Aus der Klinik für Radiologie
der Medizinischen Fakultät Charité – Universitätsmedizin Berlin

DISSERTATION

Biomechanical investigation of neurogenesis and neuroinflammation in the mouse brain by elastography

Biomechanische Untersuchung der Neurogenese und Neuroinflammation im Mäusegehirn mittels Elastographie

zur Erlangung des akademischen Grades
Doctor of Philosophy (PhD)

vorgelegt der Medizinischen Fakultät
Charité – Universitätsmedizin Berlin

von

Anna Sophie Morr

aus Berlin

Datum der Promotion: 23.03.2024

Table of contents

List of tables

List of figures

List of abbreviations

aCSF	Artificial cerebral spinal fluid
AFM	Atomic force microscopy
BBB	Blood-brain barrier
DG	Dentate gyrus
EAE	Experimental autoimmune encephalomyelitis
ECM	Extracellular matrix
Eu-VSOP	Europium-doped very small iron oxide nanoparticles
Fe	Iron
FOV	Field of view
GBCA	Gadolinium-based contrast agent
Gd	Gadolinium
GFP	Green fluorescence protein
IMC	Imaging mass cytometry
kg	Kilogram
mg	Milligram
min	Minute
mm	Millimeter
mM	Millimolar
MRE	Magnetic resonance elastography
MRI	Magnetic resonance imaging
MS	Multiple sclerosis
p.i.	Postimmunization
Pa	Pascal
PBS	Phosphate-buffered saline

PLP	Proteolipid protein
RT-PCR	Real time polymerase chain reaction
SGZ	Subgranular zone
SD	Standard deviation
TA	Acquisition time
TE	Echo time
TR	Repetition time

Abstract

Investigation of the brain´s biomechanical properties provides information on its function in physiological conditions and during disease. Adult neurogenesis in the rodent hippocampus ensures homeostasis and repair. This unique function is tightly controlled by chemical cues and has been related to mechanical properties *ex vivo*, while little is known about *in vivo* tissue mechanics of the subgranular zone (SGZ), the hippocampal neurogenic niche. Next to the importance of biomechanics in physiological processes, tissue mechanics are altered in neuroinflammatory diseases, such as multiple sclerosis (MS). Inflammatory changes in brain mechanics are influenced by different factors including immune cell infiltration, the extracellular matrix (ECM) and sex. However, the specific neuroinflammation-mediated tissue alterations underlying changes in mechanical integrity remain elusive. Tissue mechanics, measured as stiffness and fluidity, can be assessed *in vivo* by magnetic resonance elastography (MRE) and *ex vivo* using microindentation methods such as atomic force microscopy (AFM).

This thesis comprises three studies investigating (i) the *in vivo* biomechanical properties of the SGZ, a zone of neurogenesis in the rodent brain and exploring (ii) biomechanical changes during different neuroinflammatory processes, (iii) taking sex into account. More specifically, it was investigated if *in vivo* MRE, despite its much lower spatial resolution, shows similar spatial mechanical properties in the SGZ as *ex vivo* AFM measurements. Further, the experimental autoimmune encephalomyelitis model, a MS animal model, was used to investigate changes in biomechanics in areas of widespread inflammation and a leaky blood-brain barrier identified with a gadolinium-based contrast agent as well as in areas of focal inflammation visualized by accumulation of europium-doped particles. Finally, biomechanical sex differences in neuroinflammation were investigated by MRE and correlated with sex-specific properties of the ECM.

Collectively, these studies yielded the following results (i) the SGZ has softer mechanical properties *in vivo* compared to surrounding tissue, which is confirmed by *ex vivo* findings, (ii) during neuroinflammation, alterations in brain tissue mechanics are most pronounced in areas with severe focal inflammation, and (iii) in health and neuroinflammation, sex differences in cortical stiffness are associated with sex dimorphism in ECM protein expression.

These findings suggest that brain tissue mechanics are important for physiological processes such as neurogenesis, influenced by sex and are markedly affected in focal

inflammation. Macroscopic mechanical properties, resolved by MRE, are sensitive to these micromechanical structures and their pathological alterations. Hence, MRE is a promising imaging tool for investigation of physiological processes such as neurogenesis and for non-invasive clinical assessment of different pathological aspects of neuroinflammation.

Zusammenfassung

Die Untersuchung der biomechanischen Eigenschaften des Gehirns gibt Aufschluss über physiologische Funktionen und Krankheitsentstehung. Die physiologische adulte Neurogenese gewährleistet Homöostase und Regeneration im Maushippocampus. *Ex vivo* wurde die Neurogenese mit spezifischen biomechanischen Eigenschaften assoziiert, *in vivo* ist jedoch wenig über die Gewebemechanik der subgranulären Zone (SGZ), der hippocampalen neurogenen Nische, bekannt. Neben physiologischen Prozessen beeinflussen neuroinflammatorische Erkrankungen wie die Multiples Sklerose (MS) die Gewebemechanik. Entzündungsbedingte Veränderungen der Hirnmechanik werden von verschiedenen Faktoren beeinflusst, darunter Immunzellinfiltration, die extrazelluläre Matrix (EZM) und das Geschlecht. Unklar ist jedoch, welche spezifischen Gewebeveränderungen zur veränderten mechanischen Integrität führen. Die Gewebemechanik, genauer Steifigkeit und Fluidität, kann *in vivo* mittels Magnetresonanz-Elastographie (MRE) und *ex vivo* mit Mikroindentationsmethoden wie der Rasterkraftmikroskopie (AFM) gemessen werden.

Diese Arbeit umfasst drei Studien, in denen die *in vivo* biomechanischen Eigenschaften des Maushirns (i) in der SGZ, und (ii) die Veränderungen der Gewebemechanik während spezifischen neuroinflammatorischen Prozessen unter (iii) Einbezug des Geschlechts, untersucht wurden. Es wurde verglichen, ob die *in vivo* MRE, mit einer gröberen Auflösung, ähnliche räumliche mechanische Eigenschaften in der SGZ zeigt, wie *ex vivo* AFM-Messungen. Anhand des experimentellen autoimmun-Enzephalomyelitis (EAE)-Modells, einem MS-Mausmodell, wurden gewebsmechanische Veränderungen in Bereichen mit disseminierter Entzündung (visualisiert durch Gadolinium-basiertes Kontrastmittel) sowie in Bereichen mit fokalen Entzündungen (markiert durch Anreicherung von Europium-dotierten Partikeln) untersucht. Außerdem wurden Geschlechtsunterschiede in der Hirnmechanik im EAE Model mit geschlechtsspezifischen Eigenschaften der EZM korreliert.

Die vorliegenden Studien zeigen: (i) weiche mechanische *in vivo* und *ex vivo* Eigenschaften der SGZ im Vergleich zum umliegenden Gewebe; (ii) gewebsmechanische Veränderungen sind in Bereichen mit fokaler Neuroinflammation am stärksten ausgeprägt und (iii) im gesunden und inflammatorischen Zustand sind Geschlechtsunterschiede in der kortikalen Steifigkeit mit Geschlechtsunterschieden in der EZM-Proteinen Expression assoziiert.

Die Ergebnisse legen nahe, dass die Hirnmechanik für physiologische Prozesse, wie die Neurogenese, wichtig ist, vom Geschlecht beeinflusst und bei fokalen Entzündungen stark verändert wird. Makroskopische mechanische Eigenschaften, aufgelöst durch die MRE, sind empfindlich für mikromechanischen Strukturen und ihre pathologischen Veränderungen. Daher ist die MRE ein vielversprechendes bildgebendes Instrument für die Untersuchung physiologischer Prozesse und für die nicht-invasive klinische Bewertung verschiedener pathologischer Aspekte der Neuroinflammation.

1. Introduction

The study of the biomechanical properties of the brain provides important information for understanding physiological brain function and the development of neurological diseases (1, 2). In tissue mechanics, there are physical properties that characterize the deformation behavior of materials when exposed to force. Biological soft tissue is characterized by viscoelastic behavior when deformed, meaning that it simultaneously exhibits the mechanical properties of an elastic solid and a viscous fluid (1). Elastography techniques such as *in vivo* magnetic resonance elastography (MRE) or *ex vivo* microindentation methods, including atomic force microscopy (AFM), are used to measure the mechanical properties of soft tissues. MRE uses externally generated harmonic vibrations to transmit shear waves into the tissue of interest (3). Phase-contrast imaging detects wave displacement, from which viscoelastic properties such as stiffness, deduced from the shear wave speed (c), and fluidity derived from the phase angle of the complex shear modulus (ϕ), can be determined (1). Recent developments in multifrequency MRE with tomoelastography postprocessing (4) for preclinical applications allow higher resolution and imaging of multiple slices. This development makes it possible to study individual brain regions with more anatomical detail (5). However, whereas *in vivo* MRE relies on coarser scales ranging from millimeters in humans (6) to submillimeters in the preclinical setting (4), *ex vivo* AFM can measure mechanical properties of biological soft tissues with a spatial resolution on the order of a few micrometers (7). AFM determines the local elastic properties of soft matter biological samples by moving a tip over the surface of the sample and simultaneously measuring the interaction force between the surface and the tip (8).

Both physiological processes in the brain such as aging (5) and abnormal alterations like disease-related changes in neurogenesis, investigated in a model of murine Parkinson´s disease (9, 10), lead to changes in brain mechanical properties detectable by *in vivo* MRE. Adult neurogenesis is the formation of new neurons from progenitor cells, which in rodents, takes places in different brain regions such as the subgranluar zone (SGZ) of the dentate gyrus (DG), a hippocampal subregion (11, 12). The formation of new neurons is strictly regulated by chemical and physical cues (13), whereas the former, e.g., fibroblast or epidermal growth factors (14, 15), have been extensively studied, the later remain poorly understood (16). *Ex vivo* AFM studies provide already regional stiffness maps of the rodent hippocampus (7, 17, 18); however, neither *in vivo* MRE nor *ex vivo*

AFM has so far been used to investigate the SGZ, the neurogenic nice of the of the murine hippocampus.

Besides physiological processes, pathologies alter the viscoelastic properties of the brain. Neuroinflammatory diseases such as multiple sclerosis (MS) and its mouse model - the experimental autoimmune encephalomyelitis (EAE) - modify brain mechanics by reducing stiffness throughout large brain areas (19-24). MS is a chronic autoimmune demyelinating disease affecting 2.8 million people worldwide, with women being twice as likely as men to develop MS (25). Central in the pathology is the entry of myelin-reactive immune cells into the central nervous system (CNS), via the blood-brain barrier (BBB) and the blood-cerebrospinal fluid barrier (26), resulting in neuroinflammation, demyelination and neurodegeneration (27). These inflammatory processes lead to gliosis, which along with the subsequent formation of multifocal demyelination, contributes to brain softening as neuroinflammation (21), demyelination (28), microglia/macrophage activation (22) and extra cellular matrix (ECM) remodeling (24) have been shown to correlate with the observed softening. Another influencing factor appears to be sex, as brains of female MS patients exhibit a stronger reduction in viscoelasticity in response to inflammation compared to age-matched male patients (19, 20, 23). Additionally, estrogen influences the production of matrix metalloproteinases (29, 30), suggesting that the decomposition of ECM components might also be affected by sex. However, it remains to be determined how and to which degree neuroinflammatory processes such as focal inflammation and BBB leakage contribute to changes in mechanical properties and how viscoelasticity and ECM composition differs between sexes in health and during neuroinflammation.

In this thesis *in vivo* MRE was used to investigate the viscoelastic properties of the murine brain in correlation with physiological neurogenesis, sex-specific differences, and inflammation. To this end, three studies were conducted: (i) The aim of study I was to use *in vivo* MRE and *ex vivo* AFM to correlate the viscoelastic properties of the SGZ, the neurogenic niche in the mouse hippocampus, with the degree of neurogenesis in order to develop an *in vivo* biomechanical marker for neurogenic activity. Both *in vivo* MRE measurements and *ex vivo* AFM measurements were performed in the SGZ to test whether the lower spatial resolution of MRE reveals a similar mechanical signature of the SGZ as AFM measurements. (ii) The objective of study II was to determine the sensitivity of MRE to different neuroinflammatory processes such as focal inflammation and BBB leakage. In this context, the adoptive transfer EAE model, was used, and MRE measure-

ments were performed in conjunction with magnetic resonance imaging (MRI) with administration of a gadolinium-based contrast agent (GBCA) and very small superparamagnetic iron oxide particles (VSOPs); the former contrast agent visualizes BBB leakage and disseminated inflammation, the latter local inflammatory processes with marked immune cell infiltration. (iii) Study III focused on the quantification of sex differences in viscoelasticity in healthy and inflamed brain tissue and possible association with ECM alterations. In this study, MRE and ECM gene expression analysis were performed in EAE mice and age-matched female and male control mice. Overall, the studies presented here advance our understanding of the biophysical properties of brain tissue under healthy conditions and during inflammation and contribute to the development of cerebral MRE as a useful noninvasive imaging marker for preclinical and clinical research.

2. Methods

2.1 Animals and experimental set-up

All animal experiments were carried out in accordance with directive 2010/63/EU of the European Parliament and of the Council of 22th September 2010 and national and institutional guidelines for the care and use of laboratory animals and were approved by the local Animal Ethics Committee (31-33). Mice were housed under standard conditions with a 12:12 hours light-dark-cycle and ad libitum access to food and water.

2.1.1 Study I: Investigation of *in vivo* and *ex vivo* mechanical properties of the murine SGZ

As described in (33), for *in vivo* MRE measurements a total of 10 C57BL/6J mice (male, 9 to 10 weeks old, Charles River Laboratories, Germany, registration number 0301/15) were investigated. One MRE scan in the Bregma areas -2.84 mm to 0.23 mm was performed. For *ex vivo* AFM experiments 6 Tg(Nes-EGFP)33Enik/J mice (male, 7 to 9 weeks old, Leipzig University, Germany, registration number T12/20), expressing the green fluorescence protein (GFP) under the nestin promoter were sacrificed (more detail description in section 2.7). The GFP signal was used for anatomical reference to identify the SGZ.

2.1.2 Study II: Examination of the contribution of neuroinflammatory processes such as BBB leakage and focal inflammation to changes in mechanical properties

For *in vivo* MRE and MRI experiments adoptive transfer EAE was induced in 21 SJL mice (female, 9-12 weeks, Janvier, SAS, France, registration number G106/19) by the transfer of myelin proteolipid protein (PLP)-reactive lymphocytes. SJL mice were used as the animal strain of choice to induce EAE (active and adoptive transfer), as they display a high disease susceptibility after induction. PLP-reactive lymphocytes were obtained from 22 donor mice, which were actively immunized as previously described (31, 34) using 200 mg of the myelin peptide PLP139-151 emulsified with 200 ml complete Freund´s adjuvant (Thermo Fischer Scientific, United States) and 800 mg Mycobacterium tuberculosis H37Ra (Difico, United States). As described in (31), on days 0 and 2 postimmunization (p.i.), 250 ng pertussis toxin (List Biological Laboratories, United States) was injected intraperitoneally. Donor animals were sacrificed on day 10 p.i., axillary and inguinal lymph

nodes were collected and cells cultured as described (35). Cells were harvested after 4 days in culture with RPMI 1640 medium (supplemented with 2 mM L-glutamine, 100 units/ml penicillin, 100 mg/ml streptomycin and 10 % fetal bovine serum) (Gibco, Thermo Fischer Scientific) containing 12.5 mg/ml PLP. Into each of the 21 recipient mice 30 million cells were intraperitoneally injected. After immunization, recipient mice were monitored daily for signs of disease, which were scored as follows: “0-no sign, 0.5-tail paresis, 1-tail paresis and/or plegia and righting reflex weakness; 2-hind limb paresis; 3-paraplegia; 4-paraplegia with forelimb weakness or paralysis; 5-moribund or dead animal” (31). To comply with animal welfare guidelines, all mice with a score greater than 3 or with atypical signs of EAE were euthanized and removed from the study (31).

MRE was performed prior to EAE induction (baseline) and after EAE signs were established (animals showed at least partial hind limb paresis, score 1.75, for details on MRE investigations see section 2.2). When EAE signs were present, MRE was followed by pre-contrast MRI with a T1-weighted imaging, a T2-weighted sequence to acquire an anatomical image, and a pre-contrast T2-weighted sequence (for details on imaging parameters see section 2.4.2). Next, GBCA (0.2 mmol/kg, Magnevist, Bayer-Schering AG, Germany) was injected via the tail vein, and post-contrast T1-weighted images were acquired. After the scans, 0.2 mmol/kg europium-doped VSOPs (Eu-VSOPs) (batch RH030812 Eu-R; c(Fe) = 0.134 mol/L, produced and provided by the Experimental Radiology working group of the Department of Radiology, Charité - Universitätsmedizin Berlin (36)) were intravenously administered into the tail vein, and 24 hours later, a T2-weighted sequence was acquired to visualize particle accumulation. No contrast agents were injected at baseline scans. For each animal, the EAE MRE scan was compared to the corresponding baseline scan, while post-contrast imaging was compared to the pre-contrast image to determine contrast agent accumulation. A detailed visualization of the experimental timeline can be found in (31). After *in vivo* scans animals were sacrificed and tissue was processed for *ex vivo* analysis, for detailed description see section 2.8.1.

2.1.3 Study III: Exploration of regional mechanical sex differences in health and neuroinflammation and the association with sexual dimorphism in ECM protein expression

In total 33 male and 37 female SJL mice (10 to 15 weeks old, Janvier, SAS, France, registration number G106/19) were divided into four experimental groups, consisting of male healthy (n = 14), male EAE (n = 19), female healthy (n = 14) and female EAE (n = 23). The SJL strain was also selected for this study because it exhibits sex differences in

disease incidence and severity and, with the higher likelihood of disease in female mice, reflects well the sex ratio of MS in humans (37). Active EAE was induced as described in 2.1.2. Disease signs of mice were monitored and scored as aforementioned and animals with a score higher than 3 were euthanized and removed from the study (32).

EAE mice (female/male) underwent MRE based on their individual score (at least a score 1.75) and aged-matched healthy control mice (female/male) were scanned on the same experimental day. Immediately after MRE scans, animals were sacrificed and tissue was processed for *ex vivo* gene expression analysis (for detailed description see section 2.8.2). The experimental set-up is also described in (32).

2.2 MRE investigations

All *in vivo* MRE measurements (and MRI measurements, section 2.4, for experiments of (31-33)), were performed at a 7 Tesla MRI scanner (BioSpec, Bruker, Ettlingen, Germany) running with ParaVision 6.1 software. A 20-mm diameter 1H-RF quadrature volume coil (RAPID Biomedical, Würzburg, Germany) was used for image acquisition. During acquisition mice were placed on a custom-build animal holder (Figure 1A). Through an anesthesia mask a constant flow of 1.5 – 2 % isoflurane in 70 % N_2O and 30 % O_2 was administered. A pressure sensitive pad (Small Animal Instruments Inc., Stony Brook, NY, United States) was placed on the thorax for respiration monitoring. Body temperature was measured continuously with a rectal probe and kept constant by circulating water through heating pads embedded into the animal holder.

Shear waves were induced in the mouse brain using a custom-made driver system with a nonmagnetic piezoceramic actuator that generated vibrations (4). Via a transducer rod connected to a head cradle, these vibrations were transmitted into the skull of the animal. Multifrequency MRE was performed using 5 frequencies (1000, 1100, 1200, 1300, and 1400 Hz) and resulting tissue deflection were obtained by MRI motion encoding gradients yielding images of the deflection caused due to vibration (Figure 1B). In all three studies 7 coronal slices with a 0.18 mm × 0.18 mm in-plane resolution with a slice thickness of 0.8 mm were acquired. Further imaging parameters were echo time (TE) = 53 ms, repetition time (TR) = 4 ms, field of view (FOV) = 16.2 mm × 10.8 mm, matrix size = 90 × 60 and acquisition time (TA) = 9 min (31-33). Image acquisition and analysis were performed only in Bregma areas -2.84 mm to 0.23 mm to reduce scan time and to be consistent with previous studies using tomoelastography (4, 5, 38).

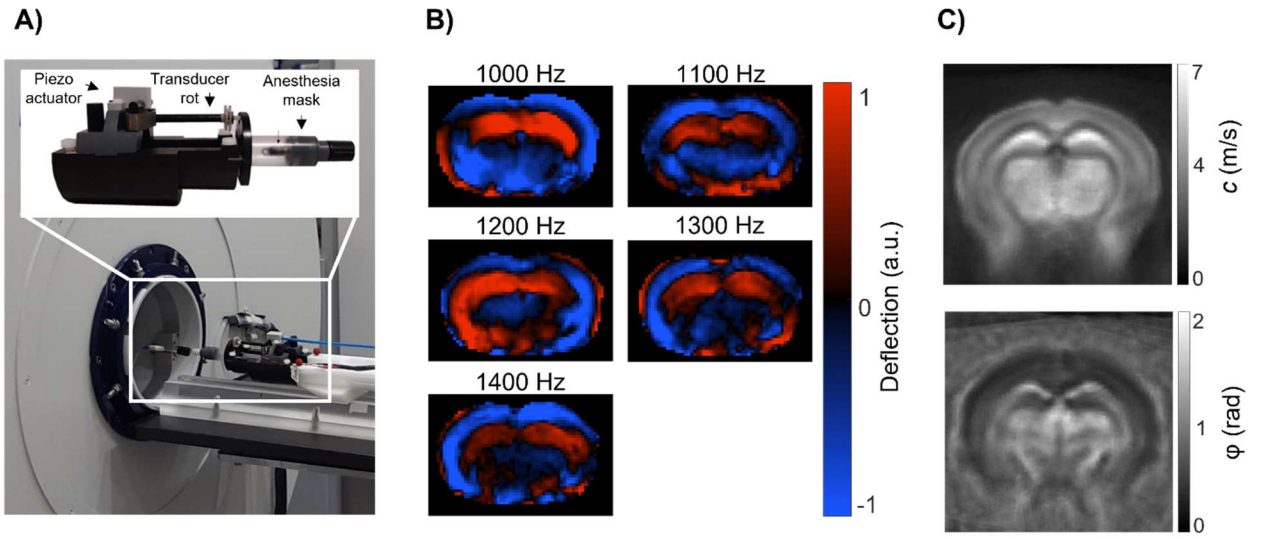

Figure 1 In vivo MRE set up, wave images and parameter maps. **A)** 7-Tesla small animal scanner, alongside with customized animal holder. Integrated into the animal holder are an anesthesia mask, a transducer rot that transmits the waves into the animal`s skull, and a nonmagnetic piezoceramic actuator for wave generation. **B)** Representative wave images, showing propagation of shear waves through the mouse brain after k-MDEV inversion (1 slice, 1 component, 5 frequencies, and no directional filters applied) **C)** Representative images of the MRE parameter maps *c* and *φ*, averaged over individual mice after registration to standard mouse brain atlas, Magnetic resonance elastography (MRE). Figure and figure caption adapted from (33)

2.3 MRE post-processing

Post-processing of the wave images, yield from MRE measurements, was performed with MATLAB R2019b (MathWorks, USA). To recover the shear wave speed, (*c* in m/s) as a representative marker of stiffness, tomoelastography post-processing was used (39) (Figure 1C). In short, the real and imaginary part of the complex-valued MRI signal was smoothed, 2D-unwarping of MRI phase signal was performed followed by selection of harmonic frequencies via Fourier transformation and high-pass directional filtering in space. Next, wave numbers for all plane waves and frequencies are reconstructed and averaged by amplitude-weighting (39). In addition, the direct Laplace-based inversion technique, the multifrequency dual elasto-visco (MDEV) inversion (1), was used to obtain the phase angle of the complex shear modulus (*φ* in rad, Figure 1C), which is a measure for the solid-fluid behavior of soft tissue. To compare the Young´s modulus (*E* in Pa) obtained from *ex vivo* AFM measurements to the *in vivo* MRE results (performed in (33)), the parameters *c* and *φ* were first converted into the magnitude of the complex shear modulus (|G*| in Pa).

$$|G^*| = \frac{c^2 \rho (1 + \cos \phi)}{2},$$

assuming material density ρ = 1000 kg/m³. Second, the *in vivo* Young´s modulus is calculated as $E_{MRE} = 3 \cdot |G^*|$.

2.4 MRI measurements

2.4.1 Anatomical reference imaging for studying the SGZ

For anatomical orientation, 13 coronal slices were acquired using a standard T2-weighted 2D rapid acquisition with relaxation enhancement (RARE) MRI sequence. Imaging parameters were: 0.078 mm × 0.078 mm in-plane resolution, 0.8 mm slice thickness, TE = 33 ms, TR = 2500 ms, 20 mm × 20 mm FOV, 265 × 265 matrix size, RARE factor = 2, number of averages = 2, bandwidth = 34722 Hz, and TA = 2:45 min (33).

2.4.2 Eu-VSOP particle visualization, GBCA imaging and anatomical reference imaging

A T2-weighted 2D-RARE sequence with 32 contiguous coronal slices with a TR = 3.500 ms, TE = 33 ms, echo spacing = 11 ms, RARE factor = 8, 4 averages, slice thickness of 0.5 mm, FOV = 18 mm × 18 mm, matrix size = 180 x 180, in-plane resolution 0.1 mm x 0.1 mm, bandwidth = 34722 Hz, and TA = 5:08 min was acquired for anatomical location (31).

For GBCA visualization a T1-weighted RARE sequence with the same geometry as the T2-weighted scan, with following parameters was performed; TR = 800 ms, TE = 6.5 ms, echo spacing = 6.5 ms, RARE factor = 2, 6 averages, bandwidth = 75000 Hz and TA = 7:12 min (31).

Eu-VSOP accumulation was visualized using a T2-weighted FLASH sequence with the same geometry as the T2-weighted scan for anatomical location and TR = 400 ms, TE = 2.5 ms, flip angle = 30 degrees, 3 averages, bandwidth = 29762 Hz and TA = 2:24 min (31).

2.5 Atlas registration of MRI images and MRE parameter maps

To combine and compare data from individual mouse brains, MRE and MRI images of study I and II were registered to the standard Allen Mouse Brain Atlas using the ANTx, a customized MATLAB toolbox (latest version available under https://github.com/ChariteExpMri/antx2) as described in (31, 33).

For the investigation of brain mechanics in the presence of contrast agents, before MRE image registration, the T2-weighted RARE, T2-weigthed FLASH pre- and post-Eu-

VSOP administration and pre- and postcontrast T1-weighted RARE were transferred into Allen mouse brain atlas space (standard space), using ELASTIX (https://elastix.lumc.nl/, (40)). Thereafter, affine non-linear b-spline transformation was used to re-slice and co-register the pre- and postcontrast T2-weighted FLASH and pre- and postcontrast T1-weighted RARE images to the T2-weighted 2D-RARE images (31).

MRE image registration to the brain atlas was performed equally for the investigation of DG subzones, including the SGZ, and the investigation of the viscoelastic properties in the presence of contrast agents. In short, the individual MRE parameter maps, c and φ, and the corresponding MR-magnitude images were 3D-co-registred and 2D-slice-wise registered to the T2-weighted 2D-RARE images. Next, MRE images were transformed into Allen mouse brain atlas space as described for the MRI images. The 7 MRE slices were interpolated to 215 slices of the reference atlas, generating approximately 58 corresponding MRE slices. More details can be found in (31, 33).

2.6 Mask generation for MRE parameter maps

2.6.1 DG and DG subzones masks

Using ANTx, the standard space mask of the DG was obtained. Using MATLAB R2019b (MathWorks Inc., Natick, MA, USA), the DG mask was 2D-eroded by one, two and three pixels (pixel size 70 µm × 70 µm) from the outer boarder towards the subgranular zone (SGZ) to evaluate DG subzones. The standardized DG mask and the eroded masks were superimposed on MRE parameter maps and mean values in the Bregma areas -2.49 mm to -2.07 mm, matching *ex vivo* AFM measurements (see section 2.7), were obtained (33).

2.6.2 Eu-VSOP particle accumulation and GBCA-enhanced area masks

As described in (31), masks depicting Eu-VSOP accumulation and Gd-enhancement were manually drawn on registered post-contrast T2-weighted and T1-weighted images using the ANALYZE 10 program (Biomedical Imaging Resources Mayo Clinic, USA). Next, all masks were registered to the Allen mouse brain atlas using ELASTIX. After registration, Eu-VSOP masks were dilated by two pixels using MATLAB to reduce effects of single-pixel artifacts, as the MRE resolution is 0.18 mm × 0.18 mm and the areas particle accumulation show as focal hypointense regions. Further, areas with Gd-enhancement were excluded from Eu-VSOP masks and vice versa to generate masks corresponding solely to either one of the two contrast agents. Additionally, for each mouse a ventricle

mask was manually drawn on the registered MRE magnitude image to exclude the ventricles from the analysis as mechanical wave propagation is not ensured in liquid-filled spaces. Masks were overlaid on MRE parameter maps in the Bregma areas -2.84 to 0.23 mm and mean values were obtained (31).

2.6.3 Manually drawn regional brain masks

Individual masks of the whole coronal midbrain, the cerebral cortex, hippocampus, and thalamic area were manually drawn on one comparable slice based on anatomical structure on the unregistered MRE images using MATLAB, to compare sexual dimorphism in healthy and EAE mice. Mean values were obtained by overlaying the mask on the MRE parameter maps. Examples of the masks and unregistered MRE images can be found in (32).

2.7 AFM measurements

The AFM is used to measure local elastic properties of biological soft matter samples (41), by moving a tip across the surface of the sample and simultaneously measuring the interaction force between the surface and the tip. The tip is attached to a soft cantilever, which´s deflection is recoded by a laser beam (8). Analysis of these force-distance-curves are used to determine the local elastic modulus applying a modified Hertz model (42).

As described in (33), for *ex vivo* AFM measurements, mice were sacrificed with an overdose of isoflurane (CP-Pharma, Burgdorf, Germany) and directly bled transcardially and then perfused with PBS. After dissection, brains were placed into artificial cerebral spinal fluid (aCSF) and cut into 350 µm thick coronal slices in the Bregma areas -2.49 mm to -2.07 mm using a vibratome (Leica VT 1200, Leica Biosystems, Wetzlar, Germany). Next, slices were placed into 24-well plates containing aCSF and indentation measurements in the DG were performed using the AFM (Nanowizard4 with 300 µm hybrid stage, JPK, Germany. The tissue samples were fixed to a glass slide with surgical glue (Histoacryl, B. Braun, Germany) and placed into aCSF supplemented with synthetic air containing 5 % CO_2 during measurements. Onto the tip of commercially available cantilevers (0.2 N/m, CONT, Nanoworld, Swiss) a small polystyrene bead (~ 6 µm diameter) was glued. A profile of 10 - 15 side-by-side 100 × 100 µm maps with a pixel resolution of 5 – 10 µm (100 - 225 pixels) for each slice was placed over the DG encompassing the

SGZ. The SGZ was visualized by the fluorescence of nestin-expressing cells. This fluorescent signal was used as anatomical marker to place the measurement profiles.

For each measurement point, local fluorescent intensity and Young´s modulus were recorded. Force curves were recorded at a z-velocity of 20 µm/s, with a nominal value of 2 nN corresponding to a penetration depth of about 2 µm. To determine the zone of GFP-expressing cells, a relative fluorescence intensity threshold was applied to automatically select all pixels within the AFM map that matched the full width at half maximum peak intensity in the GFP images. In areas with high fluorescence signal, the elasticity values were compared with the elasticity values of areas with low fluorescence signal intensity. For positional analysis, the map with the highest fluorescence intensity was selected as the central map, and the average values were calculated for each map in the profile. A total of 15 measurements were performed and data was analyzed using Data Processing Software (JPK BioAFM - Bruker Nano GmbH, Germany) (33).

2.8 *Ex vivo* tissue analysis

2.8.1 Imaging mass cytometry (IMC)

IMC was used to visualize Eu-VSOPs accumulation in inflamed brain areas and the surrounding tissue. IMC generally involves the use of antibodies labeled with metal isotopes bound to the targets of interest in the tissue. The tissue is ablated, and the presence of the metal isotopes is detected by time-of-flight based identification, which results in a detailed spatial representation of the targets in the tissue of interest (43). For IMC measurements in (31), EAE mice were sacrificed with an overdose of ketamine (Ketamin 100 mg/ml CP-Pharma, Burgdorf, Germany) /xylazine (Xylavet 20 mg/ml, CP-Pharma, Germany) immediately after the last MRI scan, followed by transcardial perfusion with 4 % paraformaldehyde (Carl RothR, Germany). As control, one healthy mouse (SJL, female, 10 weeks) without Eu-VSOP injection was sacrificed. After perfusion, prior to paraffin embedding (ROTI®Plast, Germany) brains were placed in 4% paraformaldehyde for 24 hours at 4 °C. Samples were cut in sequential 4 mm thick slices using a microtome (pfm Rotary 3000 Compact, Germany) comprising areas of Eu-VSOP accumulation, identified by MRI. Next, slices were heated at 60 °C for 1 hour and deparaffinized using m-xylene (Sigma-Aldrich, Germany). Thereafter, sections were re-hydrated in descending ethanol series (Carl RothR, Germany), and processed according to IMC staining protocol for formalin-fixed paraffin-embedded tissue sections (PN 400322 A3, Fluidigm, United States). All

antibodies used, shown in table 1 (upper panel), were tagged with a metal isotope using the Maxpar labeling kit according to the manufacturer´s instructions (Fluidigm, United States). IMC was conducted with a CyTOF2/upgraded to Helios specifications coupled to a Hyperion Tissue Imager (Fluidigm), using CyTOF software version 7.0. Dry slices were placed into the imaging module and regions of interest were selected for each sample, which were previously identified on a preview. For each specimen optimal laser power was set to ensure complete ablation of the sample and laser ablation was performed at 200 Hz and a resolution of 1 mm. For visualization, threshold correction was performed followed by the use of despeckle and sharpen tools and a Gaussian blur filter (kernel with, 0.50 pixels) using ImageJ software (ImageJ 1.48v, United States) (31).

2.8.2 Gene expression analysis

Quantitative real time polymerase chain reaction (RT-PCR) was performed to assess the expression of ECM protein genes, in the cortex and hippocampus, to study sexual dimorphism in healthy and EAE mice, as described in (32). For this reason, a subgroup of mice (female EAE = 6, male EAE = 7, female naive = 6, male naive = 6), were sacrificed after MRE measurements as described in section 2.8.1 and brains were extracted. Next, the two hemispheres of the brains were separated and from one hemisphere the hippocampus and cortex were dissected, freeze-dried in liquid nitrogen and stored at -80 °C. For quantitative RT-PCR, using the Quick-RNA-MiniPrep Kit (Zymo Research, USA), RNA was extracted from the cortex and hippocampus and cDNA synthesis was performed with the High-Capacity cDNA Reverse Transcription Kit (Thermo Fisher Scientific, USA). Measurements using TaqMan® probes (Thermo Fisher Scientific, USA, detailed information in table 1, lower panel) for the genes Lama4, Lama5, Col4a1, Col1a1, and Fn1 were performed with the QuantStudio 6 Flex Real-Time PCR system (Thermo Fisher Scientific, USA) (32). Hprt1 served as the endogenous reference (44, 45).

Table 1: Antibodies used for IMC, gene symbols and corresponding primers for TaqMan® assays used for quantitative RT-PCR

Antibody	Clone	Manufacture	Istope tag	Dilution
Anti-NeuN	1B7	Biologend	165Ho	1:400
Anti-GFAP	EPR1034	Abcam	169Tm	1:800
Anti-Iba-1	EPR16589	Abcam	144Nd	1:800
Anti-CD31	D8V9E	Cell Signaling Technology	164Dy	1:800
Anti-CD45	D3F8Q	Abcam	166Er	1:400
Anti-histone H3	D1H2	Fluidigm	176Yb	1:4000
Gene symbol	Gene name	Amplicon length	TaqMan® Assay ID	
Lama 4	Laminin, alpha 4	81	Mm01193660_m1	
Lama 5	Laminin, alpha 5	64	Mm01222029_m1	
Col1a1	Collagen, type 1, alpha 1	89	Mm00801666_g1	
Col4a1	Collagen, type IV, alpha 1	74	Mm01210125_m1	
Fn1	Fibronectin 1	58	Mm01256744_m1	
Hprt1	hypoxanthine guanine phosphoribosyl transferase	131	Mm03024075_m1	

Imaging mass cytometry (IMC), real time polymerase chain reaction (RT-PCR), adapted from (31, 32)

2.9 Statistical analyses

All statistical analyses were performed using GraphPad Prism 9.0 (GraphPad software, USA) and statistical significance was defined as $p \leq 0.05$. Normality of the data was tested using the D´Agostino & Pearson test. An unpaired t-test was used to evaluate the sexual dimorphism in viscoelastic properties of healthy mouse brains. An unpaired t-test with Welch correction was performed to assess sex differences in gene expression of ECM components in healthy mice. A paired t-test was used to compare the *ex vivo* elastic difference of low and high fluorescence signal in the DG and the percentage change on stiffness in regions with Eu-VSOP accumulation to stiffness changes in regions with no particle accumulation. The Wilcoxon matched-pairs signed rank test was used to assess the percentage change in GBCA-enhanced regions vs. non-enhanced regions. One-way repeated measures ANOVA with multiple comparisons (Tukey´s multiple comparisons test) was used for analyzing the *in vivo* MRE data in the DG and the eroded masks towards the SGZ. To study the differences in viscoelasticity *ex vivo* from peak of the fluo-

rescence signal a mixed model was used. Additionally, the gene expression of ECM proteins was evaluated with a one-way repeated measures ANOVA with multiple comparisons. A two-way ANOVA with Fisher´s LSD post-hoc comparison was performed to study brain regional sex-specific viscoelastic properties in healthy conditions and EAE. Values are reported as mean ± standard deviation (SD). Data is visualized as means ± SD.

3. Results

3.1 Study I: Investigation of *in vivo* and *ex vivo* mechanical properties of the murine subgranular zone

To assess the microscopic mechanical properties of the hippocampal subregions the MRE DG mask was eroded by 1, 2 and 3 pixels; towards the SGZ. Figure 2 on the top displays representative high-resolution maps of c and φ and the derived Young´s modulus $E_{MRE,}$ each obtained by averaging individual maps after image registration to the standard mouse brain atlas. Overlaid are representations of the original DG and the eroded masks. All parameters, c, φ, and derived Young´s modulus E_{MRE}, are significantly reduced towards the SGZ as shown in the relative changes in Figure 2A (relative change of c 1 pixel eroded (- 0.81 ± 0.86 %) vs. 2 pixels eroded (- 2.34 ± 1.69 %) ***p = 0.0010, 1 pixel eroded vs. 3 pixels eroded (- 3.41 ± 1.90 %) ***p = 0.0001, 2 pixels eroded vs. 3 pixels eroded ***p = 0.0005; relative change of φ 1 pixel eroded (- 2.06 ± 1.82 %) vs. 2 pixels eroded (- 5.00 ± 4.19 %) *p = 0.0108 , 1 pixel eroded vs. 3 pixels eroded (- 7.00 ± 6.62 %) *p = 0.0270, 2 pixels eroded vs. 3 pixels eroded not significant p = 0.0784; relative change of E_{MRE} 1 pixel eroded (- 1.06 ± 1.66 %) vs. 2 pixels (- 3.33 ± 3.10 %) eroded **p = 0.0029, 1 pixel eroded vs. 3 pixels eroded (- 5.00 ± 3.39 %) ***p = 0.0004, 2 pixels eroded vs. 3 pixels eroded **p = 0.0046). Absolute means with SD and corresponding p-values for all three parameters can be found in table 2. For *ex vivo* AFM measurements, GFP fluorescence signal was used as anatomical guidance to position measurement profiles on the SGZ (shown in Figure 2B left) and used to quantify neurogenic activity. Measurements revealed that areas with high fluorescence signal, covering the SGZ, are significantly softer compared to areas of low GFP signal intensity (Young´s modulus E area with low fluorescent signal 128 ± 72 Pa vs. area with high fluorescent signal78 ± 39 Pa, p = 0.0004, Figure 2B right).

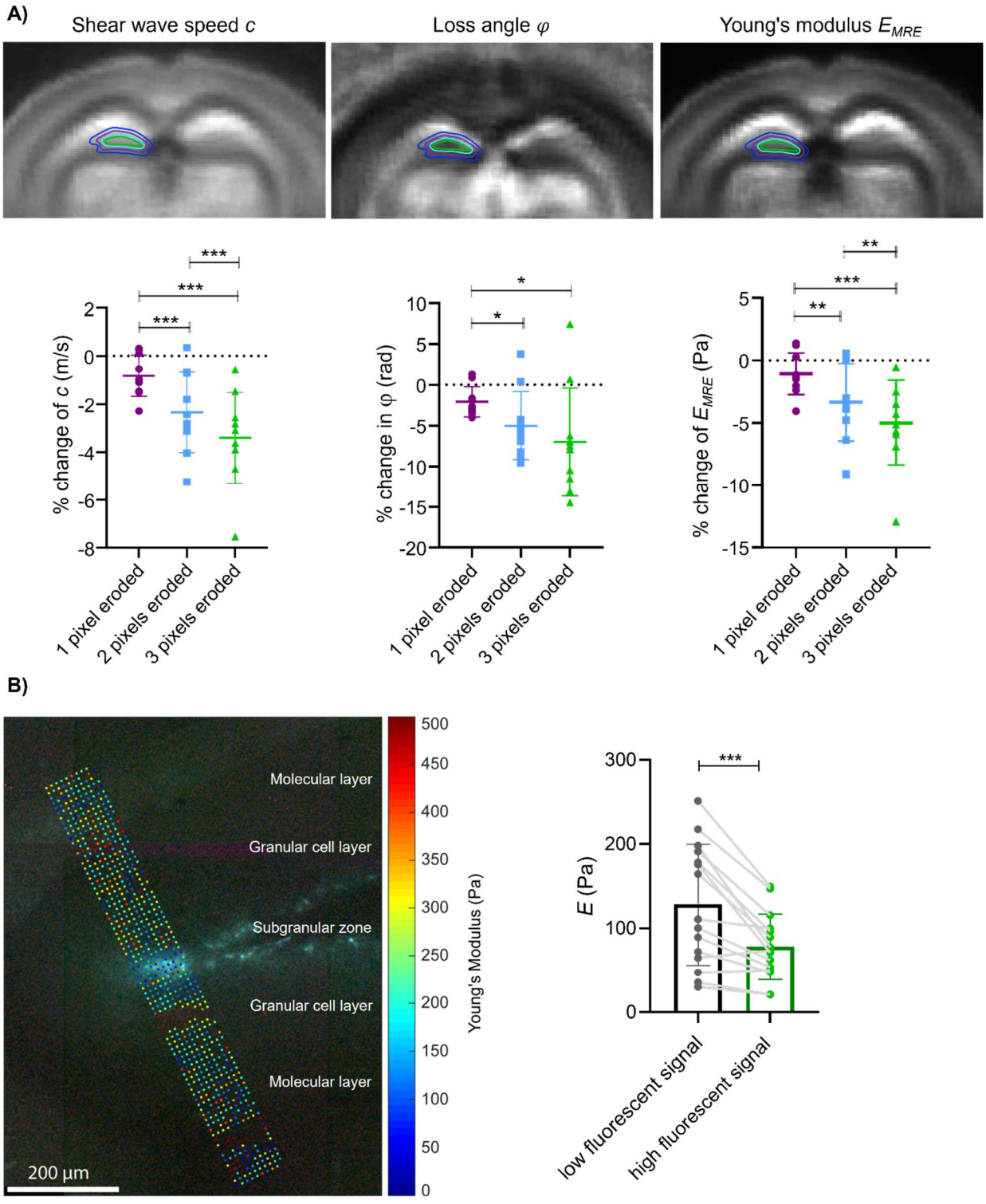

Figure 2 In vivo MRE measurements and ex vivo AFM measurements in the DG encompassing the SGZ. **A)** On the top from right to left, representative MRE parameter maps, *c, φ*, and derived Young´s modulus E_{MRE}, with schematic masks of the original DG and erosion. On the bottom all three parameters *c, φ*, and derived Young´s modulus E_{MRE}, show a significant relative decrease when the DG mask is eroded by 1 (purple), 2 (blue) and 3 (green) pixels towards the SGZ. Left, the relative change of c (1 pixel eroded vs. 2 pixels eroded **p = 0.0001, 1 pixel eroded vs. 3 pixels eroded ***p = 0.0001, 2 pixels eroded vs. 3 pixels eroded ***p = 0.0005). In the middle, the relative change of *φ* (1 pixel eroded vs. 2 pixels eroded *p = 0.0108, 1 pixel eroded vs. 3 pixels eroded *p= 0.0270, 2 pixels eroded vs. 3 pixels eroded p = 0.0784). On the right, the relative

change of Young´s modulus E_{MRE} (1 pixel eroded vs. 2 pixels eroded **p = 0.0029, 1 pixel eroded vs. 3 pixels eroded ***p = 0.0004, 2 pixels eroded vs. 3 pixels eroded **p = 0.0046). n = 10, repeated-measures ANOVA. **B)** On the left, representative measurement profile of *ex vivo* AFM measurement overlaid on the high fluorescence region with anatomical labels. On the right, areas with high fluorescence signal intensity, indicating the SGZ, exhibit softer mechanical properties than areas with low fluorescent signal, ***p = 0.0004. n = 15, paired t-test, magnetic resonance elastography (MRE), atomic force microscopy (AFM), dentate gyrus (DG), subgranular zone (SGZ). Figure and figure legend adapted from (33)

Additionally, with increasing distance from peak fluorescence, marking the SGZ, Young´s modulus *E* significantly increases, as shown in Figure 3A (means ± SD in table 2; significances are given in Figure 3A). *In vivo* MRE measurements as well indicate a significant increase in the Young´s modulus E_{MRE} away from the SGZ (0 µm (original mask) 27.7 ± 3.1 Pa, 70 µm (1 pixel erosion) 27.4 ± 3.2 Pa, 140 µm (2 pixels erosion) 26.8 ± 3.3 Pa, 210 µm (3 pixels erosion) 26.3 ± 3.3 Pa, significances are given in Figure 3B). All results can be also found in (33).

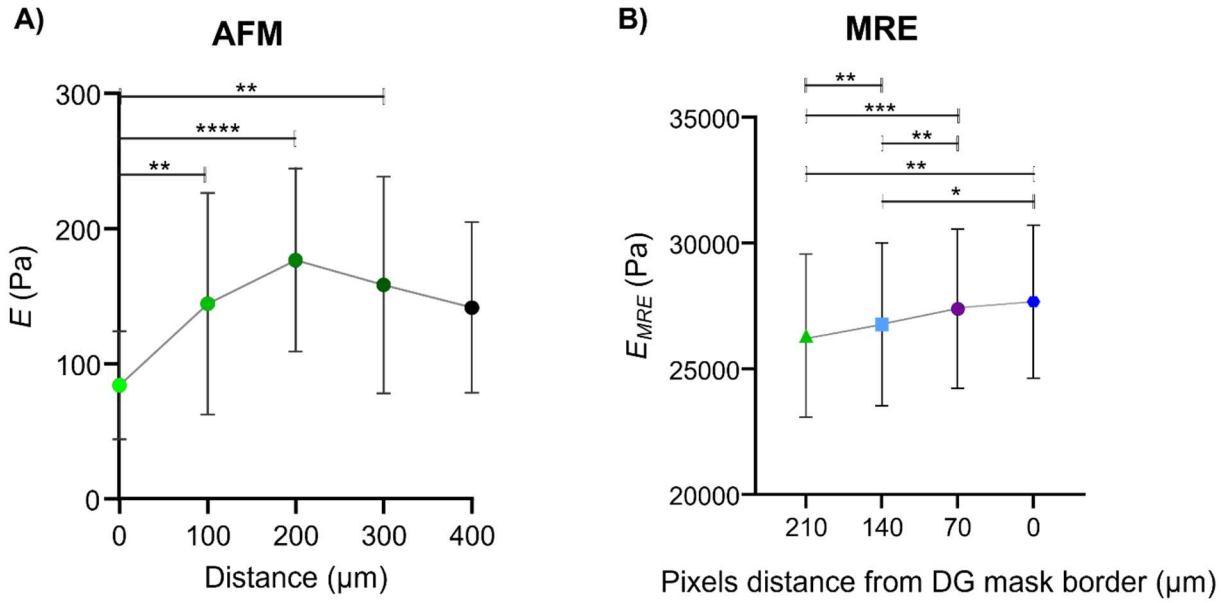

Figure 3 Comparison of ex vivo AFM and in vivo MRE in the DG. **A)** *E* increases with greater distance from peak of the fluorescence signal (marked as 0), 0 µm vs. 100 µm **p = 0.0025; 0 µm vs. 200 µm ****p<0.0001; 0 µm vs. 300 µm **p = 0.0069, 0 - 200 µm n=15, 300 µm n = 10, 400 µm n = 5, mixed model. **B)** *In vivo* MRE reveals similar results when the DG mask is eroded: original mask (0 µm) vs. 2 pixel eroded mask (140 µm), *p = 0.0309, eroded original mask (0 µm) vs. 3 pixels eroded mask (210 µm), **p =0.0043; 1 pixel eroded (70 µm) vs. 2 pixel eroded mask (140 µm), **p = 0.0051; 1 pixel eroded (70 µm) vs. 3 pixel eroded mask (210 µm), ***p = 0.0005; 2 pixel eroded (140 µm) vs. 3 pixel eroded mask (210 µm), **p = 0.0069), n = 10, repeated-measures ANOVA, atomic force microscopy (AFM), magnetic resonance elastography (MRE), dentate gyrus (DG). Figure legend adapted and figure taken from (33)

Table 2: *In vivo* MRE and *ex vivo* AFM data

MRE					
c (in m/s)		p-value			
Brain region	Mean ± SD	DG 2 pixels eroded		DG 3 pixels eroded	
DG 1 pixel eroded	3.21 ± 0.14	**0.0010**		**0.0001**	
DG 2 pixels eroded	3.16 ± 0.16			**0.0003**	
DG 3 pixels eroded	3.12 ± 0.17				
φ (in rad)		p-value			
Brain region	Mean ± SD	DG 2 pixels eroded		DG 3 pixels eroded	
DG 1 pixel eroded	0.69 ± 0.13	**0.0071**		**0.0164**	
DG 2 pixels eroded	0.66 ± 0.12			**0.0487**	
DG 3 pixels eroded	0.65 ± 0.12				
E_{MRE} (in kPa)				p-value	
Brain region	Mean ± SD	DG 2 pixels eroded		DG 3 pixels eroded	
DG 1 pixel eroded	27.39 ± 3.16	**0.0029**		**0.0003**	
DG 2 pixels eroded	26.76 ± 3.25			**0.0039**	
DG pixels eroded	26.31 ± 3.25				
AFM					
E (in Pa)		p-value			
Distance (in µm)	Mean ± SD	100	200	300	400
0	84 ± 40	**0.0025**	**<0.0001**	**0.0069**	**0.0699**
100	145 ± 82		0.1449	0.9208	>0.9999
200	177 ± 68			0.4565	0.3417
300	158 ± 80				0.2400
400	142 ± 63				

MRE values for the parameters *c, φ* and E_{MRE} and AFM values. Significant p-values are in bold. MRE – magnetic resonance elastography, AFM – atomic force microscopy, DG – dentate gyrus, adapted from (33)

3.2 Study II: Examination of the contribution of neuroinflammatory processes such as BBB leakage and focal inflammation to changes in mechanical properties

To assess viscoelastic parameters in regions of BBB leakage, exclusively detected by gadolinium enhancement, and areas of local inflammation with strong immune cell infiltrate, visualized by Eu-VSOP accumulation, mask comprising solely Gd-enhancement or Eu-VSOP accumulation were overlaid on MRE parameter maps, respectively. After EAE establishment *c* significantly decreases in regions with GBCA-enhancement (baseline

3.28 ± 0.38 m/s vs. EAE 2.99 ± 0.51 m/s, *p = 0.0183, n = 19) and in areas with Eu-VSOP accumulation (baseline 3.03 ± 0.39 m/s vs. EAE 2.55 ± 0.47 m/s, *p = 0.0235, n = 8) compared to baseline measurements. φ is unaffected in either region of contrast agent accumulation (GBCA-enhanced regions: baseline 0.85 ± 0.08 rad vs. EAE 0.86 ± 0.09 rad, p = 0.3683, n = 19; areas of Eu-VSOP accumulation: baseline 0.91 ± 0.17 rad vs. EAE 0.87 ± 0.20 rad, p = 0.1168; n = 8).

Furthermore, the percentage change in *c* and φ was analyzed in areas of GBCA-enhancement and Eu-VSOP accumulation and compared to the percentage change of the rest of the brain from baseline to EAE establishment (percentage change in *c* shown in Figure 4). No significant difference in the percentage change between non-enhancing and GBCA enhanced regions in c (Gd-enhanced areas -9.76 ± 13.32% vs. non-enhanced areas -7.18 ± 6.21%, p = 0.3321) or φ was observed (Gd-enhanced areas 4.47 ± 7.96% vs. non-enhanced areas 1.07 ± 10.56%, p = 0.1246). In areas of Eu-VSOP accumulation a significant difference in percentage change in *c* was observed compared to areas without Eu-VSOP accumulation (areas with Eu-VSOP accumulation -16.81 ± 16.49 % vs. areas without accumulation -5.85 ± 3.81%, *p = 0.0483), whereas φ was unaffected (areas with Eu-VSOP accumulation -5.29 ± 8.33% vs. areas without accumulation -2.16 ± 6.63 %, p = 0.2889).

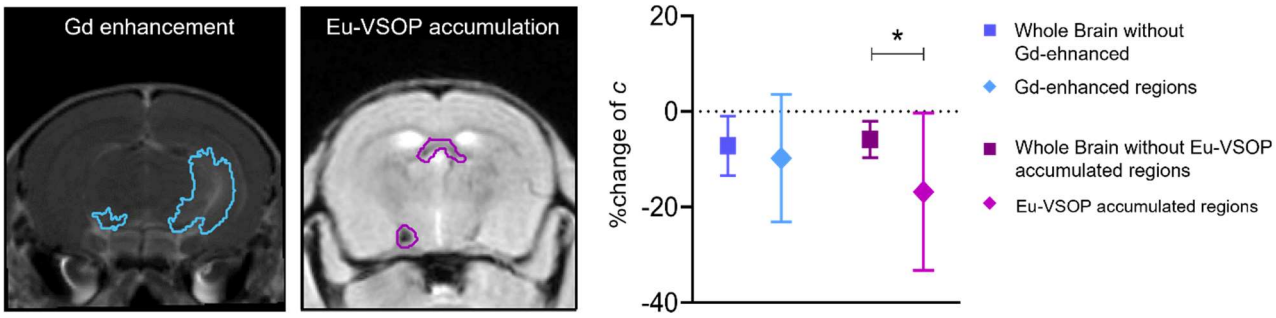

Figure 4 Percentage change of c in areas of Gd-enhancement and Eu-VSOP accumulation from baseline to EAE disease establishment. On the left, representative GBCA enhancement (T1 post GBCA injection) and Eu-VSOP accumulation (T2*-post Eu-VSOP administration) in the mouse brain during peak EAE. On the right, no significant difference in the percentage change for *c* in areas with GBCA-enhancement compared to non-enhanced areas (p = 0.3321, n = 19). A significant change in the percentage change in *c* is seen in areas with Eu-VSOP accumulation compared to areas without particle accumulation (*p = 0.0483, n = 8), paired t-tests, Gadolinium (Gd), europium-doped very small iron oxide nanoparticles (Eu-VSOP), experimental autoimmune encephalomyelitis (EAE). Figure and figure legend adapted from (31).

Subsequently, IMC was used to visualize the tissue distribution of Eu-VSOP and colocalization with barrier and inflammatory cells to confirm that the histopathological changes were indeed related to inflammation induced Eu-VSOP accumulation. EAE mice showed, compared with healthy control, clear inflammation with gliosis represented by an infiltration of immune cells (CD45, cyan) and an increase of Iba-1 (white) cells and GFAP (green). Eu-VSOPs were detected at sites of inflammation in similar regions in which particle accumulation was visible in the MRI. Areas of Eu-VSOP accumulation were associated with CD45+ leucocyte infiltration which were mostly concentrated in the periventricular space (Figure 5A, red, white arrowheads) and in the choroid plexus (Figure 5B, red, white arrows) and frequently localized adjacent to Iba-1 cells (macrophages and microglia). Accumulation of Eu-VSOP in the perivascular space was confined to these sites of injury and colocalized with CD45+ and Iba-1 positive cells. In particular, Eu-VSOPs were associated with CD31+ cells (activated endothelial cells) at the vessel walls. In the ventricles, the Eu-VSOPs were restricted to the choroid plexus, indicating a clear association with the presence of immune infiltrates. No particles co-localized with NeuN+ neurons. All presented results are from (31).

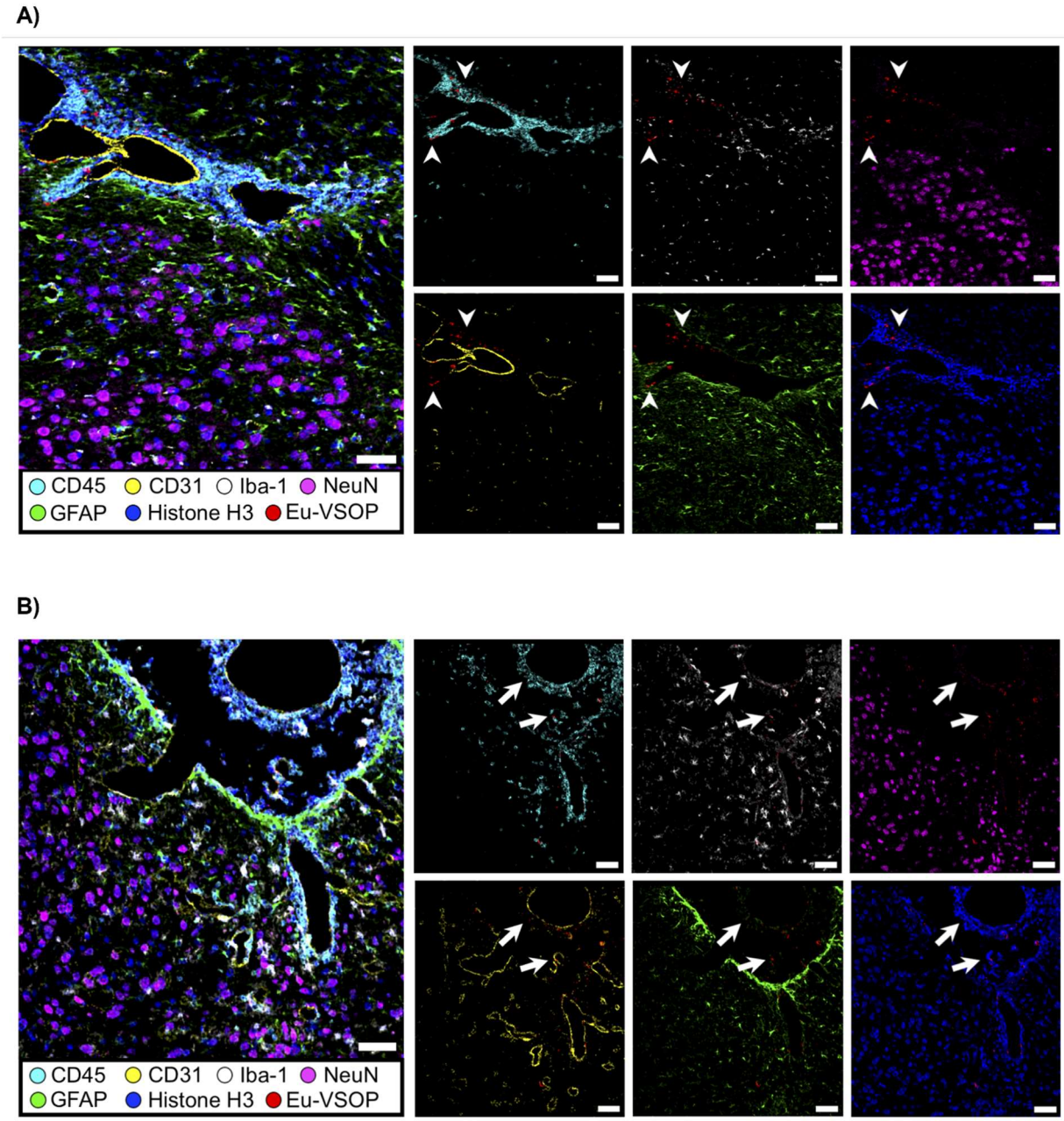

Figure 5 IMC images showing Eu-VSOP distribution and brain inflammation in EAE. **A)** Perivascular space situated between hippocampal formation and brain stem with Eu-VSOP accumulation (red, white arrowheads) and strong leucocyte infiltrate **B)** Eu-VSOPs (red, white arrows) in the choroid plexus of the third ventricle associated with perivascular inflammation; neurons (NeuN - magenta), astrocytes (GFAP - green), endothelial cells (CD31 - yellow), nuclei (histone H3 - blue), microglia (Iba-1 - white), leucocytes (CD45 - cyan), Eu-VSOPs (red dots). Scale bar: 50 µm, europium-doped very small iron oxide nanoparticles (Eu-VSOP), experimental autoimmune encephalomyelitis (EAE), imaging mass cytometry (IMC). Figure taken from (31).

3.3 Study III: Exploration of regional mechanical sex differences in health and neuroinflammation and the association with sexual dimorphism in ECM protein expression

As shown in (32), examination of the sexual dimorphism of brain tissue viscoelastic parameters in healthy mice revealed no differences in *c* comparing the midbrain (p = 0.9257), thalamus (p = 0.4105) or hippocampus (p = 0.7448). In the cortex, *c* was significantly lower in male healthy mice compared to female (*p = 0.044).

Next, the effect of sexual dimorphism on neuroinflammation was investigated by comparing a cohort of EAE male and female, after EAE signs were established, to healthy controls. In male mice a significant reduction in *c* was found when comparing the midbrain of healthy mice to EAE (*p = 0.024, Figure 6A). In the female midbrain no change in *c* was observed (p = 0.2123). In the hippocampus (Figure 6B left, female p = 0.5819, male p = 0.0831) and the thalamic area (Figure 6B right, female p = 0.7399, male p = 0.5930), no inflammation-related changes were observed in either sexes in *c*. The cortex was the most affected region during EAE, when compared to aged-matched healthy mice, with a significant reduction in *c* for female (*p = 0.013) and a trend for male mice (p = 0.067, Figure 6A). However, no sex-related difference in *c* was observed during neuroinflammation and the sex-dependent difference observed in healthy mice was maintained (**p = 0.006, Figure 6A). No significant differences between sexes and between health and EAE mice were observed in *φ*. Means and SD are presented in table 3.

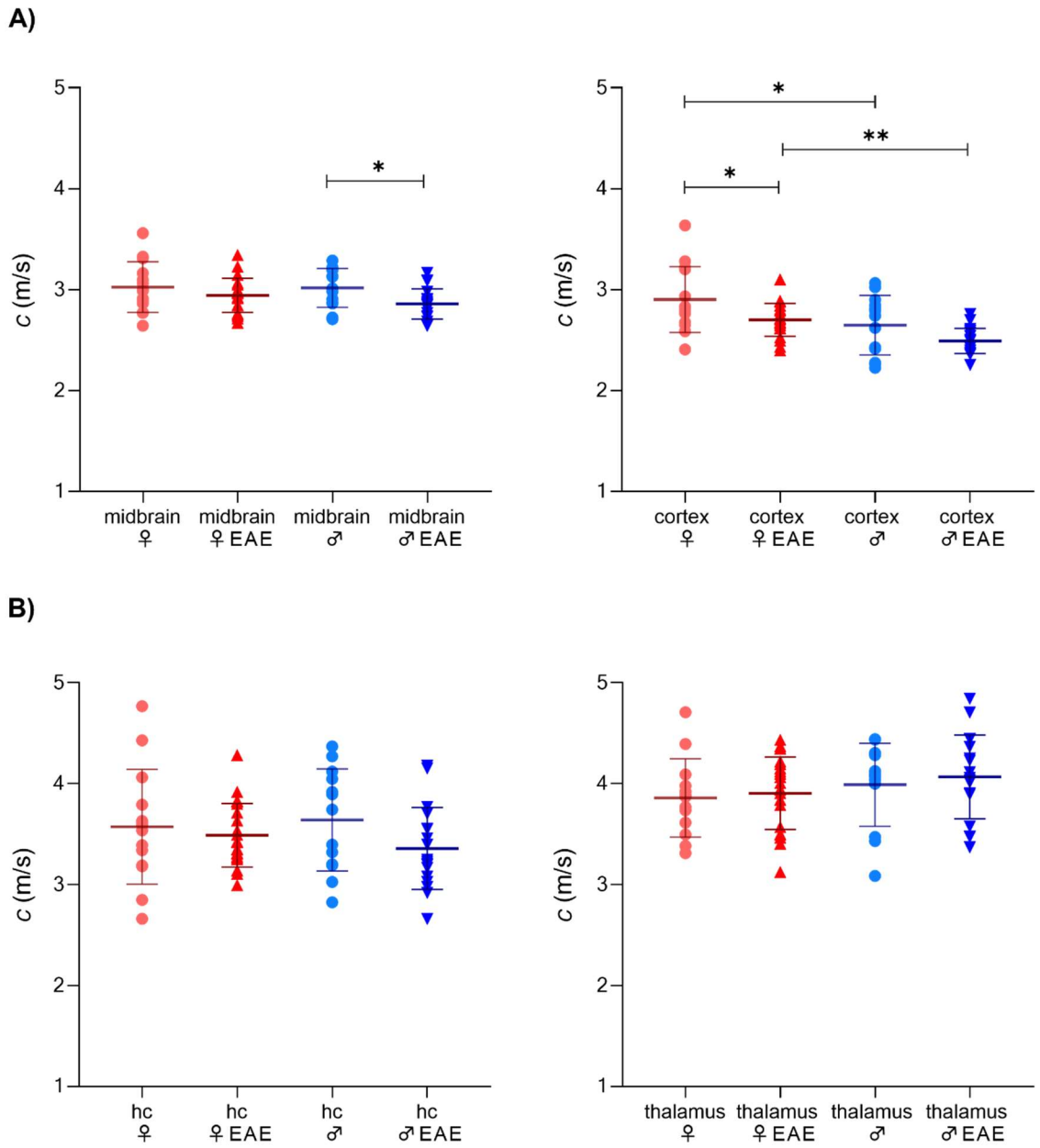

Figure 6 Regional viscoelastic parameters in both sexes in healthy and EAE mice. **A)** *c* of the midbrain (male naive vs. male EAE *p = 0.024) and the cortex (female naive vs. female EAE *p = 0.013, female EAE vs. male EAE **p = 0.006) of healthy and EAE male and female mice. B) *c* of healthy and EAE male and female mice in the hippocampus and thalamus. $n_{female\ naive}$ = 14, $n_{female\ EAE}$ = 21, $n_{male\ naive}$ = 13 $n_{male\ EAE}$ = 18. hc = hippocampus, two-way ANOVA, experimental autoimmune encephalomyelitis (EAE). Figure and figure legend adapted from (32).

In addition, sexual dimorphism in the gene expression levels of collagens (Col4a1 and Col1a1), laminins (Lama5 and Lama4) and fibronectin (Fn1) were investigated in the cerebral cortex and hippocampus ($n_{female\ naive}$ = 6, $n_{female\ EAE}$ = 6, $n_{male\ naive}$ = 6, $n_{male\ EAE}$ = 7). No differences in expression of the proteins in relation to sex in healthy mice was observed in the hippocampus. In the cortex, collagen type IV and laminin expression were significantly lower in males than in females (Col4a1 *p = 0.029, Lama4 **p = 0.006, Lama5 *p

= 0.019), whereas collagen type I did not show a significant difference. Fibronectin expression was significantly higher in the healthy male cortex compared to healthy females **p = 0.002). At peak EAE, laminin expression increased significantly in both sexes (Lama4 and Lama5 *p < 0.05), given the baseline differences between the sexes in healthy animals, the expression however remained significantly higher in female EAE (Lama4 and Lama5 ***p < 0.001). The differences of Col4a1 expression in healthy male and female mice was increased during inflammation as cortical expression in females increased by 3.0-fold (**p < 0.01) and in male by 2.0-fold (**p < 0.01) when compared to the healthy control group. Additionally, in the male cortex a decrease in the expression of Col1a1 (***p < 0.001) and Fn1 (*p = 0.018) was observed, whereas in females no significant change was seen (Figure 7A). In the hippocampus, Lama5 expression increased in females 1.83-fold (p = 0.064), whereas in males expression levels remained unaltered, leading to a significant 2.41-fold (*p = 0.025) difference during EAE between the sexes. No other significant changes regarding sex or disease status were observed in the expression levels of the target genes in the hippocampus. Means and SD for sex specific fold changes of the target genes are presented in table 3. Results are taken from (32).

Table 3: MRE and RT-PCR data (fold changes) for healthy and EAE female and male mice presented as mean ± standard deviation

	Female naive		Female EAE		Male naive		Male EAE	
MRE	*c* (m/s)	*φ* (rad)	*c* (m/s)	*φ* (rad)	*c* (m/s)	*φ* (rad)	*c* (m/s)	*φ* (rad)
Midbrain	3.03 ± 0.26	0.78 ± 0.05	2.94 ± 0.17	0.77 ± 0.05	3.02 ± 0.20	0.75 ± 0.05	2.86 ± 0.16	0.75 ± 0.04
Cortex	2.90 ± 0.33	0.65 ± 0.09	2.79 ± 0.17	0.61 ± 0.09	2.65 ± 0.30	0.65 ± 0.09	2.50 ± 0.13	0.62 ± 0.07
Hippocampus	3.58 ± 0.57	0.83 ± 0.12	4.49 ± 0.32	0.81± 0.05	3.64 ± 0.51	0.81 ± 0.08	3.36 ± 0.41	0.77 ± 0.06
Thalamus	3.86 ± 0.39	1.02 ± 0.07	3.91 ± 0.36	1.04 ± 0.07	3.99 ± 0.42	0.97 ± 0.09	4.07 ± 0.42	0.06 ± 0.10

	Female naive	Female EAE	Male naive	Male EAE
RT-PCR	Fold change	Fold change	Fold change	Fold change
Lama 4	-2.19 ± 0.17	-1.69 ± 0.16	-2.69 ± 0.03	-2.26 ± 0.08
Lama 5	-1.91 ± 0.25	-1.47 ± 0.28	-2.47 ± 0.11	-1.99 ± 0.08
Col4a1	-1.82 ± 0.15	-1.36 ± 0.18	-2.02 ± 0.11	-1.71 ± 0.07
Col1a1	-1.85 ± 0.12	-1.97 ± 0.15	-1.76 ± 0.13	-2.09 ± 0.12
Fn	-1.84 ± 0.10	-1.78 ± 0.06	-1.56 ± 0.10	-1.71 ± 0.09

Magnetic resonance elastography (MRE), real time polymerase chain reaction (RT-PCR), experimental autoimmune encephalomyelitis (EAE), Laminin, alpha 4 (Lama 4) Laminin, alpha 5 (Lama 5), Collagen, type IV, alpha 1 (Col4a1), Collagen, type 1 alpha 1 (Col4a1), Fibronectin 1 (Fn), adapted from (32)

4. Discussion

This thesis for the first time combined *in vivo* high-resolution multifrequency MRE with microscopic *ex vivo* AFM, contrast-enhanced MRI and histological methods to investigate the viscoelastic properties of the mouse brain in a region of neurogenesis and during neuroinflammation. The three animal studies yielded insights into the micromechanical structures that influence macroscopic mechanical properties measured by MRE in health and disease. In study I, *in vivo* MRE measurements were performed in the SGZ, one of the neurogenic niches in the murine brain. MRE data were compared with *ex vivo* AFM results obtained in the SGZ, using GFP-labelled nestin as an anatomical marker, to investigate whether *in vivo* measurements reflect similar patterns of mechanical properties as observed *ex vivo*. In study II, adoptive transfer EAE was induced in mice and MRE measurements were performed in conjunction with GBCA- and VSOPs-enhanced MRI at peak of the disease to study the contribution of BBB leakage/disseminated inflammation and local inflammatory processes with a strong immune cell infiltrate to the alterations of brain mechanics in neuroinflammation. In study III, the focus was on the effect of sex on viscoelasticity in healthy and EAE mice and possible correlation with sex differences in the expression levels of ECM proteins.

4.1 MRE shows soft mechanical properties of the SGZ compared to surrounding tissue, which is confirmed by *ex vivo* findings

Previous studies have shown that MRE can detect microscopic mechanical parameters such as tumor stiffness in the micrometer range (46) or collagen crosslinking on the nanoscale (47). Study I provides additional evidence that MRE is sensitive to the mechanical signature of the microscopic region involved in adult neurogenesis, the SGZ.

The heterogeneity of the mechanical properties of the DG´s demonstrated by *in vivo* MRE and *ex vivo* AFM measurement in study I is in agreement with previous *ex vivo* AFM studies. These studies show that the molecular layer and the hilus, surrounding the granular cell layer, are stiffer compared to the granular cell layer (7, 48). In these studies, the SGZ was not specifically targeted and probably included in the measurements of the surrounding granular cell layer (7, 48), hence, the findings are consistent with the results presented here of a gradual softening towards the SGZ. *Ex vivo* indentation measurements performed to investigate the SGZ separately and comparing the neurogenic niche

directly with its surrounding structures, show that the SGZ also exhibits softer mechanical properties (17), further corroborating the results of study I.

The role of tissue softness for neurogenic function is still being explored. Results of an *ex vivo* AFM study, investigating the major neuronal stem cell niche in the murine brain, the subependymal zone (49), suggests that a relative stiffness gradient exists that controls the differentiation and migratory behavior of newborn neurons. Kjell et al. showed that the neuronal stem cell niche is stiffer than adjacent non-neurogenic brain tissue and more distant regions such as the cortex. However, the subependymal zone and the rostral migratory stream were softer compared to the granule and glomerular cell layers of the olfactory bulb. In the mouse brain, neuroblasts that are born in the subependymal zone migrate into the olfactory bulb via the rostral migratory stream (49). The results of Kjell et al., therefore, suggest that durotaxis is crucial for the migration of neurons and hence, are consistent with the results of study I, showing a soft mechanical signature of the SGZ compared to the surrounding tissue of the DG (33). In the murine DG, newly generated neurons migrate (50) from the softer SGZ into the stiffer granular cell layer, emphasizing the role of durotaxis in cell migration (33).

Several studies using *ex vivo* microindentation methods or *in vivo* elastography have shown that the mechanical properties of neurogenic regions are important for brain pathophysiology (9, 10, 51-56). However, to our knowledge, no other study has correlated noninvasively measured mechanical properties of the intact brain with spatially resolved imaging of neurogenic function, paving the way for the development of an *in vivo* biomechanical marker of neurogenic activity (33).

4.2 MRE is sensitive to processes associated with strong focal inflammation visualized by Eu-VSOP accumulation

It has been shown that MRE is sensitive to changes in global brain mechanical properties due to neuroinflammation in MS patients and in the EAE model (19-22, 24). In study II, GBCA- and Eu-VSOP-enhanced MRI was performed along with MRE in adoptive transfer EAE at peak of the disease to study regional effects of tissue softening in areas of GBCA or Eu-VSOP accumulation. As discussed in (31), analysis of enhancement patterns showed that tissue softening was more pronounced in areas of Eu-VSOP accumulation than in areas of Gd-enhancement. Additional histological visualization of Eu-VSOPs by

IMC confirmed their colocalization in areas of intense focal inflammation, where significant tissue remodelling is likely to occur. This provides evidence that MRE is particularly sensitive to inflammatory brain tissue alterations with strong immune cell infiltration.

Previous studies associated global brain softening with the severity of inflammation, as F4/80 gene expression (22), a macrophage marker, and increased expression of CD3 (21), a T-cell marker, positively correlated with the observed softening. Additionally, the decrease in stiffness was found to correlate with enhanced expression of the ECM protein fibronectin (57), suggesting that neurovascular remodelling at lesion sites also contributes to altered tissue mechanics. However, these earlier studies are limited by the fact that they investigated viscoelasticity changes only in large brain areas in a single slice and therefore provide no regionally resolved data on inflammation. In study II novel tomoelastogprahy (4) was applied, which allows generation of stiffness maps over multiple slices with a sufficient spatial resolution to resolve areas of inflammation visualized by Gd-enhancement and Eu-VSOP accumulation (31).

The results of study II showed that areas of Gd-enhancement displayed a significant reduction in brain stiffness. However, this observed softening was similar to that detected in non-enhanced areas (31). In general, GBCA-enhanced MRI shows BBB permeability as large diffuse hyperintense areas in both, EAE models and MS patients (58-64). Therefore, it can be assumed that the decrease in stiffness is not due to localized tissue changes solely related to BBB breakdown. Instead, the Gd accumulation primarily indicates widespread tissue softening attributable to the general inflammatory state of the brain, as discussed above. The extent of diffusion of GBCA through the brain after passing the BBB can be attributed to factors such as the degree of vascular leakage (65) and disruption, distribution of contrast agent in the intracellular and interstitial space (66), or the decrease of the extracellular space and perfusion at sites of inflammation (59).

Gd-enhancing lesions not often correlate with the existence of immune cell infiltrate-derived lesions, a major characteristic of MS and EAE (59, 67), whereas the results of study I revealed Eu-VSOP at lesion sites marked by immune cell infiltration, which is in line with previous research (62, 68, 69). VSOPs can enter the brain via different routes including phagocytosis through activated T-cells (63) or peripheral macrophages (62, 68), binding to epithelial or endothelial barriers (19, 35), and passive diffusion as free particles through the disrupted BBB (34). These observations suggest that Eu-VSOPs reveal other histopathological changes than the known BBB disruption, which underly Gd-enhancement (34, 62, 69). Visualization of Eu-VSOP using IMC showed co-localization of particles

at sites of inflammation with endothelial cells. The magnetic particles could have been up taken by the cells via inflammation-induced alteration of sulfated glycosaminoglycans on the endothelial glycocalyx (69). Additionally, co-localization of particles with leucocyte infiltration (CD45+) and activated microglia (Iba-1+) was observed, suggesting phagocytosis. As reported in (31), areas of Eu-VSOP accumulation were significantly softer than non-enhanced areas. One factor contributing to the pronounced softening could be the presence of glia cells, which AFM measurements have shown to be softer than their neighboring neurons (70). Furthermore, dynamic alterations of the ECM structure, due to inflammatory activity, such as the accumulation of fibronectin, have also been correlated with neural tissue softening in EAE (24) and therefore may have contribute, to the observed stiffness alterations.

4.3 MRE detects sexual dimorphism in cortical stiffness which is associated with differences in ECM protein expression levels

Previous studies show ECM alterations during neuroinflammation and a correlation with the observed overall brain softening (24). Study III builds on this work with an additional focus on sexual dimorphism, which may influence ECM composition and brain mechanical properties. Here, sexual dimorphism of cortical mechanical properties was found in both healthy mice and EAE. Furthermore, both sexes exhibited cortical softening during neuroinflammation which was associated with ECM remodeling, providing further evidence that MRE is sensitive to microscopic tissue alterations such as ECM remodeling.

Consistent with previous research in humans (20, 71), study III showed that the healthy mouse brain exhibited sex-dependent differences in elasticity, primarily affecting the cerebral cortex, as the healthy male cortex was on average 9 % softer than the female cortex. Gene expression analysis revealed a significantly higher fibronectin expression in the healthy male cortex compared to the female one, while in the healthy female cortex expression of collagen IV and laminin was significantly higher (32). The ECM proteins fibronectin, collagen type IV and laminin, are mainly located in the basement membrane of the ECM of the central nervous system and exhibit important mechanical features (72-80). Therefore, differences in basement membrane constitution between the sexes could have an influence on cortical stiffness.

Although global brain softening of female EAE mice (21, 24) and MS patients of both sexes (20) has been reported, significant softening was observed only in the male

EAE midbrain, whereas no effect was seen in female mice. Here, the analysis of a single coronal slice could explain this discrepancy in results, which might cover different anatomical locations and structures as previous studies. In the present study, both sexes, however, showed significant cortical softening during neuroinflammation to a similar extent, resulting in a similar intersex difference in stiffness as observed in healthy brains. The effect of cortical softening in both sexes was reflected in a higher expression of collagen type IV and laminins in EAE mice compared to controls (32). This is in line with findings on glial scars resulting from tissue injury, which associate tissue softening with increased expression of collagen type IV and laminin (81).

Furthermore, a significant downregulation of fibronectin and collagen type I was shown in the male EAE cortex compared to healthy male mice, while previous research found increased fibronectin expression along with perivascular leucocyte infiltrates to tissue softening (24) and reports describing fibronectin deposition in MS lesions (82, 83). However, in the present study no leucocyte infiltration in the cortex was observed (data not shown, see (32)), and therefore, it can be hypothesized that cortical collagen type I and fibronectin expressions were not elevated and hence have not contributed to the observed tissue softening (32). Most insights on ECM remodeling in neuroinflammation comes from white matter lesions (84) while changes of the ECM in normal-appearing grey matter, such as the cortex, are not well understood yet.

No significant changes in the mechanical properties or ECM gene expression levels were detected in the thalamus and in the hippocampus. In line with previous research (21, 22, 24), no changes in fluidity were found in study II or III. Fluidity, deduced from the phase angle of the complex shear modulus, denotes conversion of a solid into a liquid in a continuous range from 0 to π/2. In biological tissue, fluidity describes the ability of particles to change their position in the mechanical network (5). The fact that no changes in fluidity were observed suggests that the overall architecture of the mechanical network is not affected by neuroinflammation, nor does it differ between sexes.

4.4. Limitations

Although encouraging results were obtained in all three studies, there are several limitations. First, the direct comparison between *in vivo* MRE and *ex vivo* AFM measurements of the murine DG in study I is compromised by the lack of AFM image registration with MRE parameter maps, since *ex vivo* measurements covered only small portions of the

MRE image slices. Hence, in the MRE parameter maps the SGZ location had to be estimated. The lack of a standardized SGZ atlas mask further complicated the location of the SGZ. Second, MRE measurements in the region of the SGZ might have been degraded by partial volume effects introduced by the nearby ventricles. However, erosion of the DG mask toward the SGZ increased the distance to the ventricles and led to a decrease in viscoelasticity, while an increase should have occurred in the presence of partial volume effects. Third, absolute Young´s modulus values obtained by AFM could have been affected by the size of the beads, the cantilever, and indentation velocities; however, these parameters were still in the limits in which the linear Hertz model could safely be applied (33).

Finally, the MRE set-up, with tomoelastogprahy used in all three studies did not include cerebellum and spinal cord in the image acquisition range due to technical restrictions. This limits the investigation of brain mechanics in EAE mice performed in study II and III, as the cerebellum and spinal cord are particularly affected regions in EAE models (22, 63, 85). Future studies should include these regions to further elucidate pathological alterations in brain mechanics detected by MRE.

4.5 Implications for future research

The study of micromechanical structures resolved by MRE at the macro level in health and disease can be leveraged for non-invasive clinical assessment. More precisely, the insights into the viscoelastic properties of the SGZ presented here enhance our understanding of how the mechanical properties of a tissue form the tissue environment that sustains homeostasis, repair, and neuronal proliferation. Future studies using *in vivo* MRE could investigate other neurogenic niches in the mouse, e.g., the subependymal zone next to the lateral ventricles, to foster our understanding of the biophysical environment required for healthy neurogenesis. Moreover, the influence of the ECM composition of neurogenic niches on their biomechanical properties could be investigated, since the ECM plays a central role in the process of adult neurogenesis (86, 87). The findings could be of interest for research in the field of neuronal regenerative medicine.

Our findings regarding *in vivo* mechanical properties during neuroinflammation could be exploited for clinical practice in the future. Studies II and III provide further evidence that ECM remodeling contributes to brain softening observed during neuroinflam-

mation. The combined use of contrast-enhanced MRI, regional brain mechanical properties assessment and analysis of ECM composition during different phase of EAE, including onset, remission, and relapse phases, could shed light on the prognostic value of *in vivo* MRE. Furthermore, regional resolved MRE could be used to monitor treatment response during the different inflammatory phases. Here, emphasize could also be placed on sex-related differences in contrast agent enhancement and response to treatment.

MS is a heterogeneous disease affecting both white and gray matter. Therefore, future MRE studies could also focus on the cortex, which is primarily composed of gray matter, as this region was identified to be severely affected in study III based on stiffness changes and ECM remodeling. One potential ECM target in the cortex could be perineuronal nets. Growing evidence suggests that perineuronal nets have an important role in neuronal structure and function in neuroinflammatory diseases such as MS (88, 89). Degradation of cortical perineuronal nets has been observed during EAE (88). Therefore, it could be hypothesized that cortical perineuronal net degradation correlates with cortical softening in EAE or in genetically modulated mouse models that have a compromised perineuronal net structure (90). The findings could further contribute to the establishment of MRE as a preclinical and clinical imaging marker.

5. Conclusions

This work investigated the micromechanical structures of the mouse brain during the physiological process of neurogenesis, in terms of sexual dimorphism, and their pathological changes during neuroinflammation. The three studies conducted show that the macroscopic mechanical properties, resolved by MRE, are sensitive to these microstructures and their alterations. The following major conclusions can be drawn from the findings of these studies: (i) the SGZ, the hippocampal neurogenic niche, is softer than the surrounding tissue which is detected by *in vivo* MRE and confirmed by *ex vivo* measurements; (ii) MRE is sensitive to local neuroinflammation where strong immune cell infiltration takes place, as identified by Eu-VSOP MRI, and (iii) there are sex-specific differences in cortical stiffness measured by MRE, and these differences correlate with differences in ECM protein expression levels.

Collectively, the results presented here further our understanding of the biophysical properties of brain tissue under healthy conditions and during inflammation. On the one hand, MRE is a suitable non-invasive imaging modality with the potential to become an *in vivo* biomechanical marker for neurogenic activity. On the other hand, MRE allows *in vivo* visualization of pathological processes with similar sensitivity and detail resolution as Eu-VSOPs-enhanced MRI. MRE could therefore be used for the investigation of neuroinflammation in preclinical and clinical studies and become a non-invasive tool for clinical diagnosis and therapy monitoring. In summary, MRE is highly sensitive to physiological and pathological processes in the brain and provides a useful non-invasive imaging marker for both preclinical and clinical research.

6. Reference list

1. Hirsch S, Braun J, Sack I. Magnetic resonance elastography: physical background and medical applications: John Wiley & Sons; 2017.
2. Barnes JM, Przybyla L, Weaver VM. Tissue mechanics regulate brain development, homeostasis and disease. J Cell Sci. 2017;130(1):71-82.
3. Manduca A, Bayly PJ, Ehman RL, Kolipaka A, Royston TJ, Sack I, Sinkus R, Van Beers BE. MR elastography: Principles, guidelines, and terminology. Magn Reson Med. 2021;85(5):2377-90.
4. Bertalan G, Guo J, Tzschätzsch H, Klein C, Barnhill E, Sack I, Braun J. Fast tomoelastography of the mouse brain by multifrequency single-shot MR elastography. Magnetic Resonance in Medicine. 2019;81(4):2676-87.
5. Guo J, Bertalan G, Meierhofer D, Klein C, Schreyer S, Steiner B, Wang S, da Silva RV, Infante-Duarte C, Koch S. Brain maturation is associated with increasing tissue stiffness and decreasing tissue fluidity. Acta biomaterialia. 2019;99:433-42.
6. Delgorio PL, Hiscox LV, Daugherty AM, Sanjana F, Pohlig RT, Ellison JM, Martens CR, Schwarb H, McGarry MDJ, Johnson CL. Effect of Aging on the Viscoelastic Properties of Hippocampal Subfields Assessed with High-Resolution MR Elastography. Cereb Cortex. 2021;31(6):2799-811.
7. Antonovaite N, Beekmans SV, Hol EM, Wadman WJ, Iannuzzi D. Regional variations in stiffness in live mouse brain tissue determined by depth-controlled indentation mapping. Scientific Reports. 2018;8(1):12517.
8. Heinisch JJ, Lipke PN, Beaussart A, El Kirat Chatel S, Dupres V, Alsteens D, Dufrêne YF. Atomic force microscopy–looking at mechanosensors on the cell surface. Journal of cell science. 2012;125(18):4189-95.
9. Hain EG, Klein C, Munder T, Braun J, Riek K, Mueller S, Sack I, Steiner B. Dopaminergic neurodegeneration in the mouse is associated with decrease of viscoelasticity of substantia nigra tissue. PLoS One. 2016;11(8):e0161179.
10. Klein C, Hain EG, Braun J, Riek K, Mueller S, Steiner B, Sack I. Enhanced adult neurogenesis increases brain stiffness: in vivo magnetic resonance elastography in a mouse model of dopamine depletion. PloS one. 2014;9(3):e92582.
11. Steiner B, Wolf S, Kempermann G. Adult neurogenesis and neurodegenerative disease. Regen Med. 2006;1(1):15-28.
12. Kempermann G, Jessberger S, Steiner B, Kronenberg G. Milestones of neuronal development in the adult hippocampus. Trends Neurosci. 2004;27(8):447-52.
13. Cha KJ, Kong S-Y, Lee JS, Kim HW, Shin J-Y, La M, Han BW, Kim DS, Kim H-J. Cell density-dependent differential proliferation of neural stem cells on omnidirectional nanopore-arrayed surface. Scientific Reports. 2017;7(1):13077.
14. Palmer TD, Ray J, Gage FH. FGF-2-responsive neuronal progenitors reside in proliferative and quiescent regions of the adult rodent brain. Mol Cell Neurosci. 1995;6(5):474-86.
15. Reynolds BA, Tetzlaff W, Weiss S. A multipotent EGF-responsive striatal embryonic progenitor cell produces neurons and astrocytes. J Neurosci. 1992;12(11):4565-74.
16. Franze K, Guck J. The biophysics of neuronal growth. Reports on Progress in Physics. 2010;73(9):094601.
17. Luque T, Kang MS, Schaffer DV, Kumar S. Microelastic mapping of the rat dentate gyrus. R Soc Open Sci. 2016;3(4):150702.

18. Elkin BS, Azeloglu EU, Costa KD, Morrison Iii B. Mechanical heterogeneity of the rat hippocampus measured by atomic force microscope indentation. Journal of neurotrauma. 2007;24(5):812-22.
19. Streitberger K-J, Sack I, Krefting D, Pfüller C, Braun J, Paul F, Wuerfel J. Brain viscoelasticity alteration in chronic-progressive multiple sclerosis. PloS one. 2012;7(1):e29888.
20. Wuerfel J, Paul F, Beierbach B, Hamhaber U, Klatt D, Papazoglou S, Zipp F, Martus P, Braun J, Sack I. MR-elastography reveals degradation of tissue integrity in multiple sclerosis. Neuroimage. 2010;49(3):2520-5.
21. Riek K, Millward JM, Hamann I, Mueller S, Pfueller CF, Paul F, Braun J, Infante-Duarte C, Sack I. Magnetic resonance elastography reveals altered brain viscoelasticity in experimental autoimmune encephalomyelitis. Neuroimage Clin. 2012;1(1):81-90.
22. Millward JM, Guo J, Berndt D, Braun J, Sack I, Infante-Duarte C. Tissue structure and inflammatory processes shape viscoelastic properties of the mouse brain. NMR in Biomedicine. 2015;28(7):831-9.
23. Fehlner A, Behrens JR, Streitberger KJ, Papazoglou S, Braun J, Bellmann-Strobl J, Ruprecht K, Paul F, Würfel J, Sack I. Higher-resolution MR elastography reveals early mechanical signatures of neuroinflammation in patients with clinically isolated syndrome. Journal of Magnetic Resonance Imaging. 2016;44(1):51-8.
24. Wang S, Millward JM, Hanke-Vela L, Malla B, Pilch K, Gil-Infante A, Waiczies S, Mueller S, Boehm-Sturm P, Guo J. MR elastography-based assessment of matrix remodeling at lesion sites associated with clinical severity in a model of multiple sclerosis. Frontiers in neurology. 2020;10:1382.
25. Walton C, King R, Rechtman L, Kaye W, Leray E, Marrie RA, Robertson N, La Rocca N, Uitdehaag B, van der Mei I, Wallin M, Helme A, Angood Napier C, Rijke N, Baneke P. Rising prevalence of multiple sclerosis worldwide: Insights from the Atlas of MS, third edition. Multiple Sclerosis Journal. 2020;26(14):1816-21.
26. Alvarez JI, Cayrol R, Prat A. Disruption of central nervous system barriers in multiple sclerosis. Biochimica et Biophysica Acta (BBA)-Molecular Basis of Disease. 2011;1812(2):252-64.
27. Thompson AJ, Baranzini SE, Geurts J, Hemmer B, Ciccarelli O. Multiple sclerosis. Lancet. 2018;391(10130):1622-36.
28. Schregel K, Wuerfel E, Garteiser P, Gemeinhardt I, Prozorovski T, Aktas O, Merz H, Petersen D, Wuerfel J, Sinkus R. Demyelination reduces brain parenchymal stiffness quantified in vivo by magnetic resonance elastography. Proc Natl Acad Sci U S A. 2012;109(17):6650-5.
29. Voskuhl RR, Gold SM. Sex-related factors in multiple sclerosis: genetic, hormonal and environmental contributions. Nature reviews Neurology. 2012;8(5):255.
30. Gold SM, Sasidhar MV, Morales LB, Du S, Sicotte NL, Tiwari-Woodruff SK, Voskuhl RR. Estrogen treatment decreases matrix metalloproteinase (MMP)-9 in autoimmune demyelinating disease through estrogen receptor alpha (ERα). Laboratory investigation. 2009;89(10):1076-83.
31. Silva RV, Morr AS, Mueller S, Koch SP, Boehm-Sturm P, Rodriguez-Sillke Y, Kunkel D, Tzschätzsch H, Kühl AA, Schnorr J, Taupitz M, Sack I, Infante-Duarte C. Contribution of Tissue Inflammation and Blood-Brain Barrier Disruption to Brain Softening in a Mouse Model of Multiple Sclerosis. Frontiers in Neuroscience. 2021;15(999).

32. Batzdorf CS, Morr AS, Bertalan G, Sack I, Silva RV, Infante-Duarte C. Sexual dimorphism in extracellular matrix composition and viscoelasticity of the healthy and inflamed mouse brain. Biology. 2022;11(2):230.
33. Morr AS, Nowicki M, Bertalan G, Vieira Silva R, Infante Duarte C, Koch SP, Boehm-Sturm P, Krügel U, Braun J, Steiner B, Käs JA, Fuhs T, Sack I. Mechanical properties of murine hippocampal subregions investigated by atomic force microscopy and in vivo magnetic resonance elastography. Scientific Reports. 2022;12(1):16723.
34. Millward JM, Schnorr J, Taupitz M, Wagner S, Wuerfel JT, Infante-Duarte C. Iron oxide magnetic nanoparticles highlight early involvement of the choroid plexus in central nervous system inflammation. ASN Neuro. 2013;5(1):e00110.
35. Plewes D, Betty I, Urchuk S, Soutar I. Visualizing tissue compliance with MR imaging. Journal of Magnetic Resonance Imaging. 1995;5(6):733-8.
36. de Schellenberger AA, Hauptmann R, Millward JM, Schellenberger E, Kobayashi Y, Taupitz M, Infante-Duarte C, Schnorr J, Wagner S. Synthesis of europium-doped VSOP, customized enhancer solution and improved microscopy fluorescence methodology for unambiguous histological detection. Journal of nanobiotechnology. 2017;15(1):1-14.
37. Bebo BF, Jr., Schuster JC, Vandenbark AA, Offner H. Gender differences in experimental autoimmune encephalomyelitis develop during the induction of the immune response to encephalitogenic peptides. J Neurosci Res. 1998;52(4):420-6.
38. Bertalan G, Klein C, Schreyer S, Steiner B, Kreft B, Tzschätzsch H, de Schellenberger AA, Nieminen-Kelhä M, Braun J, Guo J, Sack I. Biomechanical properties of the hypoxic and dying brain quantified by magnetic resonance elastography. Acta Biomater. 2020;101:395-402.
39. Tzschätzsch H, Guo J, Dittmann F, Hirsch S, Barnhill E, Jöhrens K, Braun J, Sack I. Tomoelastography by multifrequency wave number recovery from time-harmonic propagating shear waves. Med Image Anal. 2016;30:1-10.
40. Klein S, Staring M, Murphy K, Viergever MA, Pluim JP. Elastix: a toolbox for intensity-based medical image registration. IEEE transactions on medical imaging. 2009;29(1):196-205.
41. Hertz H. Über die Berührung fester elastischer Körper. Journal für die reine und angewandte Mathematik. 1882;92(156-171):22.
42. Mahaffy R, Shih C, MacKintosh F, Käs J. Scanning probe-based frequency-dependent microrheology of polymer gels and biological cells. Physical review letters. 2000;85(4):880.
43. Niewold P, Ijsselsteijn ME, Verreck FAW, Ottenhoff THM, Joosten SA. An imaging mass cytometry immunophenotyping panel for non-human primate tissues. Frontiers in Immunology. 2022;13.
44. Zamani A, Powell KL, May A, Semple BD. Validation of reference genes for gene expression analysis following experimental traumatic brain injury in a pediatric mouse model. Brain Research Bulletin. 2020;156:43-9.
45. Kang Y, Wu Z, Cai D, Lu B. Evaluation of reference genes for gene expression studies in mouse and N2a cell ischemic stroke models using quantitative real-time PCR. BMC neuroscience. 2018;19(1):1-11.
46. Sauer F, Fritsch A, Grosser S, Pawlizak S, Kießling T, Reiss-Zimmermann M, Shahryari M, Müller WC, Hoffmann K-T, Käs JA. Whole tissue and single cell mechanics are correlated in human brain tumors. Soft matter. 2021;17(47):10744-52.

47. Sauer F, Oswald L, de Schellenberger AA, Tzschätzsch H, Schrank F, Fischer T, Braun J, Mierke CT, Valiullin R, Sack I. Collagen networks determine viscoelastic properties of connective tissues yet do not hinder diffusion of the aqueous solvent. Soft matter. 2019;15(14):3055-64.
48. Antonovaite N, Hulshof LA, Hol EM, Wadman WJ, Iannuzzi D. Viscoelastic mapping of mouse brain tissue: relation to structure and age. journal of the mechanical behavior of biomedical materials. 2021;113:104159.
49. Kjell J, Fischer-Sternjak J, Thompson AJ, Friess C, Sticco MJ, Salinas F, Cox J, Martinelli DC, Ninkovic J, Franze K. Defining the adult neural stem cell niche proteome identifies key regulators of adult neurogenesis. Cell stem cell. 2020;26(2):277-93. e8.
50. Ming G-l, Song H. Adult neurogenesis in the mammalian brain: significant answers and significant questions. Neuron. 2011;70(4):687-702.
51. Gerischer LM, Fehlner A, Köbe T, Prehn K, Antonenko D, Grittner U, Braun J, Sack I, Flöel A. Combining viscoelasticity, diffusivity and volume of the hippocampus for the diagnosis of Alzheimer's disease based on magnetic resonance imaging. NeuroImage: Clinical. 2018;18:485-93.
52. Sandroff BM, Johnson CL, Motl RW. Exercise training effects on memory and hippocampal viscoelasticity in multiple sclerosis: a novel application of magnetic resonance elastography. Neuroradiology. 2017;59(1):61-7.
53. Huesmann GR, Schwarb H, Smith DR, Pohlig RT, Anderson AT, McGarry MDJ, Paulsen KD, Wszalek TM, Sutton BP, Johnson CL. Hippocampal stiffness in mesial temporal lobe epilepsy measured with MR elastography: Preliminary comparison with healthy participants. Neuroimage Clin. 2020;27:102313.
54. Majumdar S, Klatt D. Longitudinal study of sub-regional cerebral viscoelastic properties of 5XFAD Alzheimer's disease mice using multifrequency MR elastography. Magn Reson Med. 2021;86(1):405-14.
55. Antonovaite N, Hulshof LA, Huffels CFM, Hol EM, Wadman WJ, Iannuzzi D. Mechanical alterations of the hippocampus in the APP/PS1 Alzheimer’s disease mouse model. Journal of the Mechanical Behavior of Biomedical Materials. 2021;122:104697.
56. Zhao W, Cui W, Xu S, Cheong LZ, Shen C. Examination of Alzheimer's disease by a combination of electrostatic force and mechanical measurement. J Microsc. 2019;275(1):66-72.
57. Wang S, Millward JM, Hanke-Vela L, Malla B, Pilch K, Gil-Infante A, Waiczies S, Mueller S, Boehm-Sturm P, Guo J, Sack I, Infante-Duarte C. MR Elastography-Based Assessment of Matrix Remodeling at Lesion Sites Associated With Clinical Severity in a Model of Multiple Sclerosis. Frontiers in Neurology. 2020;10(1382).
58. Hawkins C, Munro P, MacKenzie F, Kesselring J, Tofts P, BOULAY ED, Landon D, McDonald W. Duration and selectivity of blood-brain barrier breakdown in chronic relapsing experimental allergic encephalomyelitis studied by gadolinium-DTPA and protein markers. Brain. 1990;113(2):365-78.
59. Nessler S, Boretius S, Stadelmann C, Bittner A, Merkler D, Hartung H-P, Michaelis T, Brück W, Frahm J, Sommer N. Early MRI changes in a mouse model of multiple sclerosis are predictive of severe inflammatory tissue damage. Brain. 2007;130(8):2186-98.
60. Schellenberg AE, Buist R, Yong VW, Del Bigio MR, Peeling J. Magnetic resonance imaging of blood–spinal cord barrier disruption in mice with experimental autoimmune encephalomyelitis. Magnetic Resonance in Medicine: An Official

Journal of the International Society for Magnetic Resonance in Medicine. 2007;58(2):298-305.
61. Smorodchenko A, Wuerfel J, Pohl EE, Vogt J, Tysiak E, Glumm R, Hendrix S, Nitsch R, Zipp F, Infante-Duarte C. CNS-irrelevant T-cells enter the brain, cause blood–brain barrier disruption but no glial pathology. European Journal of Neuroscience. 2007;26(6):1387-98.
62. Tysiak E, Asbach P, Aktas O, Waiczies H, Smyth M, Schnorr J, Taupitz M, Wuerfel J. Beyond blood brain barrier breakdown–in vivo detection of occult neuroinflammatory foci by magnetic nanoparticles in high field MRI. Journal of Neuroinflammation. 2009;6(1):1-8.
63. Wuerfel J, Tysiak E, Prozorovski T, Smyth M, Mueller S, Schnorr J, Taupitz M, Zipp F. Mouse model mimics multiple sclerosis in the clinico-radiological paradox. European Journal of Neuroscience. 2007;26(1):190-8.
64. Waiczies H, Millward JM, Lepore S, Infante-Duarte C, Pohlmann A, Niendorf T, Waiczies S. Identification of cellular infiltrates during early stages of brain inflammation with magnetic resonance microscopy. PLoS One. 2012;7(3):e32796.
65. Layne KA, Dargan PI, Archer JR, Wood DM. Gadolinium deposition and the potential for toxicological sequelae–A literature review of issues surrounding gadolinium-based contrast agents. British journal of clinical pharmacology. 2018;84(11):2522-34.
66. Aime S, Caravan P. Biodistribution of gadolinium-based contrast agents, including gadolinium deposition. Journal of Magnetic Resonance Imaging: An Official Journal of the International Society for Magnetic Resonance in Medicine. 2009;30(6):1259-67.
67. Nathoo N, Yong VW, Dunn JF. Understanding disease processes in multiple sclerosis through magnetic resonance imaging studies in animal models. NeuroImage: Clinical. 2014;4:743-56.
68. Millward JM, de Schellenberger AA, Berndt D, Hanke-Vela L, Schellenberger E, Waiczies S, Taupitz M, Kobayashi Y, Wagner S, Infante-Duarte C. Application of europium-doped very small iron oxide nanoparticles to visualize neuroinflammation with MRI and fluorescence microscopy. Neuroscience. 2019;403:136-44.
69. Berndt D, Millward JM, Schnorr J, Taupitz M, Stangl V, Paul F, Wagner S, Wuerfel JT, Sack I, Ludwig A. Inflammation-induced brain endothelial activation leads to uptake of electrostatically stabilized iron oxide nanoparticles via sulfated glycosaminoglycans. Nanomedicine: Nanotechnology, Biology and Medicine. 2017;13(4):1411-21.
70. Lu Y-B, Franze K, Seifert G, Steinhäuser C, Kirchhoff F, Wolburg H, Guck J, Janmey P, Wei E-Q, Käs J. Viscoelastic properties of individual glial cells and neurons in the CNS. Proceedings of the National Academy of Sciences. 2006;103(47):17759-64.
71. Sack I, Beierbach B, Wuerfel J, Klatt D, Hamhaber U, Papazoglou S, Martus P, Braun J. The impact of aging and gender on brain viscoelasticity. Neuroimage. 2009;46(3):652-7.
72. Miller RT. Mechanical properties of basement membrane in health and disease. Matrix Biol. 2017;57-58:366-73.
73. Storm C, Pastore JJ, MacKintosh FC, Lubensky TC, Janmey PA. Nonlinear elasticity in biological gels. Nature. 2005;435(7039):191-4.

74. Li H, Zheng Y, Han YL, Cai S, Guo M. Nonlinear elasticity of biological basement membrane revealed by rapid inflation and deflation. Proceedings of the National Academy of Sciences. 2021;118(11):e2022422118.
75. Bhave G, Colon S, Ferrell N. The sulfilimine cross-link of collagen IV contributes to kidney tubular basement membrane stiffness. American Journal of Physiology-Renal Physiology. 2017;313(3):F596-F602.
76. Pastor-Pareja JC, Xu T. Shaping cells and organs in Drosophila by opposing roles of fat body-secreted Collagen IV and perlecan. Developmental cell. 2011;21(2):245-56.
77. Candiello J, Balasubramani M, Schreiber EM, Cole GJ, Mayer U, Halfter W, Lin H. Biomechanical properties of native basement membranes. The FEBS Journal. 2007;274(11):2897-908.
78. Gould DB, Phalan FC, Van Mil SE, Sundberg JP, Vahedi K, Massin P, Bousser MG, Heutink P, Miner JH, Tournier-Lasserve E. Role of COL4A1 in small-vessel disease and hemorrhagic stroke. New England Journal of Medicine. 2006;354(14):1489-96.
79. Gould DB, Phalan FC, Breedveld GJ, van Mil SE, Smith RS, Schimenti JC, Aguglia U, van der Knaap MS, Heutink P, John SW. Mutations in Col4a1 cause perinatal cerebral hemorrhage and porencephaly. Science. 2005;308(5725):1167-71.
80. Pöschl E, Schlötzer-Schrehardt U, Brachvogel B, Saito K, Ninomiya Y, Mayer U. Collagen IV is essential for basement membrane stability but dispensable for initiation of its assembly during early development. Development. 2004;131(7):1619-28.
81. Moeendarbary E, Weber IP, Sheridan GK, Koser DE, Soleman S, Haenzi B, Bradbury EJ, Fawcett J, Franze K. The soft mechanical signature of glial scars in the central nervous system. Nature communications. 2017;8(1):1-11.
82. Van Horssen J, Dijkstra CD, De Vries HE. The extracellular matrix in multiple sclerosis pathology. Journal of Neurochemistry. 2007;103(4):1293-301.
83. Ghorbani S, Yong VW. The extracellular matrix as modifier of neuroinflammation and remyelination in multiple sclerosis. Brain. 2021;144(7):1958-73.
84. Ghorbani S, Yong VW. The extracellular matrix as modifier of neuroinflammation and remyelination in multiple sclerosis. Brain. 2021.
85. Tonra JR. Cerebellar susceptibility to experimental autoimmune encephalomyelitis in SJL/J mice: potential interaction of immunology with vascular anatomy. The Cerebellum. 2002;1(1):57-68.
86. Faissner A, Reinhard J. The extracellular matrix compartment of neural stem and glial progenitor cells. Glia. 2015;63(8):1330-49.
87. Schaberg E, Götz M, Faissner A. The extracellular matrix molecule tenascin-C modulates cell cycle progression and motility of adult neural stem/progenitor cells from the subependymal zone. Cell Mol Life Sci. 2022;79(5):244.
88. Potter LE, Paylor JW, Suh JS, Tenorio G, Caliaperumal J, Colbourne F, Baker G, Winship I, Kerr BJ. Altered excitatory-inhibitory balance within somatosensory cortex is associated with enhanced plasticity and pain sensitivity in a mouse model of multiple sclerosis. Journal of neuroinflammation. 2016;13(1):1-20.
89. Fawcett JW, Oohashi T, Pizzorusso T. The roles of perineuronal nets and the perinodal extracellular matrix in neuronal function. Nature Reviews Neuroscience. 2019;20(8):451-65.
90. Rowlands D, Lensjø KK, Dinh T, Yang S, Andrews MR, Hafting T, Fyhn M, Fawcett JW, Dick G. Aggrecan Directs Extracellular Matrix-Mediated Neuronal Plasticity. J Neurosci. 2018;38(47):10102-13.

Statutory Declaration

“I, Anna Sophie Morr, by personally signing this document in lieu of an oath, hereby affirm that I prepared the submitted dissertation on the topic Biomechanical investigation of neurogenesis and neuroinflammation in the mouse brain by elastography/ Biomechanische Untersuchung der Neurogenese und Neuroinflammation im Mäusegehirn mittels Elastographie, independently and without the support of third parties, and that I used no other sources and aids than those stated.
All parts which are based on the publications or presentations of other authors, either in letter or in spirit, are specified as such in accordance with the citing guidelines. The sections on methodology (in particular regarding practical work, laboratory regulations, statistical processing) and results (in particular regarding figures, charts and tables) are exclusively my responsibility.

Furthermore, I declare that I have correctly marked all of the data, the analyses, and the conclusions generated from data obtained in collaboration with other persons, and that I have correctly marked my own contribution and the contributions of other persons (cf. declaration of contribution). I have correctly marked all texts or parts of texts that were generated in collaboration with other persons.

My contributions to any publications to this dissertation correspond to those stated in the below joint declaration made together with the supervisor. All publications created within the scope of the dissertation comply with the guidelines of the ICMJE (International Committee of Medical Journal Editors; http://www.icmje.org) on authorship. In addition, I declare that I shall comply with the regulations of Charité – Universitätsmedizin Berlin on ensuring good scientific practice.

I declare that I have not yet submitted this dissertation in identical or similar form to another Faculty.

The significance of this statutory declaration and the consequences of a false statutory declaration under criminal law (Sections 156, 161 of the German Criminal Code) are known to me.”

Date Signature

Declaration of your own contribution to the publications

Anna Sophie Morr contributed the following to the below listed publications:

Publication 1:

Anna S. Morr, Marcin Nowicki, Gergely Bertalan, Rafaela Vieira Silva, Carmen Infante Duarte, Stefan Paul Koch, Philipp Boehm-Sturm, Ute Krügel, Jürgen Braun, Barbara Steiner, Josef A. Käs, Thomas Fuhs and Ingolf Sack, Mechanical properties of hippocampal subregions: a comparative study using atomic force microscopy and magnetic resonance elastography in the murine brain, Scientific Reports, 2022

Contribution:

Together with Ingolf Sack I developed the study design. I was the main experimenter of the study and performed the *in vivo* MRE and MRI measurements (data for Figure 1, 3, 4 and 6) with technical assistance of Gergerly Bertalan. Together with Thomas Fuhs, I performed the *ex vivo* AFM measurements (data for figure 1, 5 and 6). I prepared the tissue for AFM measurements with technical assistance of Marcin Nowicki. I conducted the histological staining resulting in Figure 2. I performed the statistical analysis of the data resulting the mentioned figures. I wrote the entire manuscript and prepared all the figures. Marcin Nowicki, Gergely Bertalan, Rafaela Vieira Silva, Carmen Infante Duarte, Stefan Paul Koch, Philipp Boehm-Sturm, Ute Krügel, Jürgen Braun, Barbara Steiner, Josef A. Käs, Thomas Fuhs and Ingolf Sack critically revised the manuscript. Together with Ingolf Sack and Thomas Fuhs, I corresponded with the reviewers and the editor and adapted the manuscript and figures as requested by the reviewers.

Publication 2:

Rafaela Vieira Silva*, **Anna S. Morr***, Susanne Mueller, Stefan Paul Koch, Philipp Boehm-Sturm, Yasmina Rodriguez-Sillke, Désirée Kunkel, Heiko Tzschätzsch, Anja A. Kühl, Jörg Schnorr, Matthias Taupitz, Ingolf Sack and Carmen Infante-Duarte, Contribution of Tissue Inflammation and Blood-Brain Barrier Disruption to Brain Softening in a Mouse Model of Multiple Sclerosis, Frontiers in Neuroscience, 2021

* Rafaela Vieira Silva and Anna S. Morr contributed equally to this work and share the first authorship

Contribution:

Together with Rafaela Vieira Silva and Carmen Infante Duarte, I developed the study design (resulting in Figure 1). Rafaela Vieira Silva and I were the main experimenters. I performed the MRE and MRI measurements together with Rafaela Vieira Silva. I performed the MRE data reconstruction and MRI and MRE image registration to the standard mouse brain atlas (resulting in Figure 2). Together with Rafaela Vieira Silva, I analyzed the contrast agent distribution (resulting in Figure 3) and analyzed the MRE data (resulting in Figure 4,5,6, and 7). Rafaela Viera Silva and I performed the brain tissue preparation and antibody tagging for imaging mass cytometry analysis (resulting in Figure 8 & 9). Together with Rafaela Vieira Silva, I performed the statistical analysis, and prepared all the figures. The entire manuscript was written by Rafaela Vieira Silva and me supported by Ingolf Sack and Carmen Infante Duarte, except the Methods part on imaging mass cytometry analysis, which was written and performed by Yasmina Rodriguez-Sillke and Désirée Kunkel. Rafaela Vieira Silva and I corresponded with the editor and reviewers and revised the manuscript.

Publication 3:

Clara Sophie Batzdorf, **Anna Sophie Morr**, Gergely Bertalan, Ingolf Sack, Rafaela Vieira Silva and Carmen Infante-Duarte, Sexual Dimorphism in Extracellular Matrix Composition and Viscoelasticity of the Healthy and Inflamed Mouse Brain, Biology, 2022

Contribution:

I conducted together with Clara Batzdorf and Rafaela Vieira Silva the MRE experiments. I supervised and performed the MRE data reconstruction together with Clara Batzdorf resulting in Figure 1, 2 and 4. I assisted in the tissue collection for the *ex vivo* gene expression analysis resulting in figure 3 and 5. I critically revised the manuscript and supported the revision processes.

_____

Signature, date and stamp of first supervising university professor / lecturer

_____

Signature of doctoral candidate

Printing copies of the publications and excerpts from Journal Summary List

Publication 1

Anna S. Morr, Marcin Nowicki, Gergely Bertalan, Rafaela Vieira Silva, Carmen Infante Duarte, Stefan Paul Koch, Philipp Boehm-Sturm, Ute Krügel, Jürgen Braun, Barbara Steiner, Josef A. Käs, Thomas Fuhs and Ingolf Sack, Mechanical properties of hippocampal subregions: a comparative study using atomic force microscopy and magnetic resonance elastography in the murine brain, Scientific Reports, 2022

Journal Data Filtered By: **Selected JCR Year: 2020** Selected Editions: SCIE,SSCI
Selected Categories: **"MULTIDISCIPLINARY SCIENCES"** Selected Category Scheme: WoS
Gesamtanzahl: 73 Journale

Rank	Full Journal Title	Total Cites	Journal Impact Factor	Eigenfactor Score
1	NATURE	915,925	49.962	1.089400
2	SCIENCE	814,971	47.728	0.895760
3	National Science Review	5,889	17.275	0.011400
4	Nature Communications	453,215	14.919	1.238540
5	Science Advances	65,205	14.136	0.218640
6	Nature Human Behaviour	5,549	13.663	0.023120
7	Science Bulletin	8,832	11.780	0.016400
8	PROCEEDINGS OF THE NATIONAL ACADEMY OF SCIENCES OF THE UNITED STATES OF AMERICA	799,058	11.205	0.806620
9	Journal of Advanced Research	5,927	10.479	0.006800
10	GigaScience	5,876	6.524	0.018630
11	Scientific Data	10,617	6.444	0.034470
12	Frontiers in Bioengineering and Biotechnology	7,470	5.890	0.011340
13	ANNALS OF THE NEW YORK ACADEMY OF SCIENCES	52,619	5.691	0.021430
14	iScience	5,235	5.458	0.012300
15	Research Synthesis Methods	3,926	5.273	0.007520
16	NPJ Microgravity	594	4.415	0.001790
17	Scientific Reports	541,615	4.379	1.232500
18	PHILOSOPHICAL TRANSACTIONS OF THE ROYAL SOCIETY A-MATHEMATICAL PHYSICAL AND ENGINEERING SCIENCES	24,950	4.226	0.025400

www.nature.com/scientificreports

scientific reports

Check for updates

OPEN

Mechanical properties of murine hippocampal subregions investigated by atomic force microscopy and in vivo magnetic resonance elastography

Anna S. Morr[1], Marcin Nowicki[2], Gergely Bertalan[1], Rafaela Vieira Silva[3,4], Carmen Infante Duarte[3], Stefan Paul Koch[5,6], Philipp Boehm-Sturm[5,6], Ute Krügel[7], Jürgen Braun[8], Barbara Steiner[9], Josef A. Käs[10], Thomas Fuhs[10] & Ingolf Sack[1]✉

The hippocampus is a very heterogeneous brain structure with different mechanical properties reflecting its functional variety. In particular, adult neurogenesis in rodent hippocampus has been associated with specific viscoelastic properties in vivo and ex vivo. Here, we study the microscopic mechanical properties of hippocampal subregions using ex vivo atomic force microscopy (AFM) in correlation with the expression of GFP in presence of the nestin promoter, providing a marker of neurogenic activity. We further use magnetic resonance elastography (MRE) to investigate whether in vivo mechanical properties reveal similar spatial patterns, however, on a much coarser scale. AFM showed that tissue stiffness increases with increasing distance from the subgranular zone ($p = 0.0069$), and that stiffness is 39% lower in GFP than non-GFP regions ($p = 0.0004$). Consistently, MRE showed that dentate gyrus is, on average, softer than Ammon´s horn (shear wave speed = 3.2 ± 0.2 m/s versus 4.4 ± 0.3 m/s, $p = 0.01$) with another 3.4% decrease towards the subgranular zone ($p = 0.0001$). The marked reduction in stiffness measured by AFM in areas of high neurogenic activity is consistent with softer MRE values, indicating the sensitivity of macroscopic mechanical properties in vivo to micromechanical structures as formed by the neurogenic niche of the hippocampus.

Abbreviations

aCSF	Artificial cerebrospinal fluid
AFM	Atomic force microscopy
AH	Ammon's horn

[1]Department of Radiology, Charité-Universitätsmedizin Berlin, Corporate Member of Freie Universität Berlin and Humboldt-Universität zu Berlin, Charitéplatz 1, 10117 Berlin, Germany. [2]Institute of Anatomy, University of Leipzig, Leipzig, Germany. [3]Experimental and Clinical Research Center, Max Delbrück Center for Molecular Medicine in the Helmholtz Association (MDC) and Charité-Universitätsmedizin Berlin, Corporate Member of Freie Universität Berlin and Humboldt-Universität zu Berlin, Berlin, Germany. [4]Einstein Center for Neurosciences Berlin, Charité-Universitätsmedizin Berlin, Corporate Member of Freie Universität Berlin and Humboldt-Universität zu Berlin, Berlin, Germany. [5]Department of Experimental Neurology and Center for Stroke Research, Charité-Universitätsmedizin Berlin, Corporate Member of Freie Universität Berlin and Humboldt-Universität zu Berlin, Berlin, Germany. [6]NeuroCure Cluster of Excellence and Charité Core Facility 7T Experimental MRIs, Charité-Universitätsmedizin Berlin, Corporate Member of Freie Universität Berlin and Humboldt-Universität zu Berlin, Berlin, Germany. [7]Rudolf Boehm Institute of Pharmacology and Toxicology, University of Leipzig, Leipzig, Germany. [8]Institute of Medical Informatics, Charité-Universitätsmedizin Berlin, Corporate Member of Freie Universität Berlin and Humboldt-Universität zu Berlin, Berlin, Germany. [9]Clinic for Neurology and Experimental Neurology, Charité-Universitätsmedizin Berlin, Corporate Member of Freie Universität Berlin and Humboldt-Universität zu Berlin, Berlin, Germany. [10]Section of Soft Matter Physics, Peter Debye Institute for Soft Matter Physics, Faculty of Physics and Geosciences, University of Leipzig, Leipzig, Germany. ✉email: ingolf.sack@charite.de

DG	Dentate gyrus
ECM	Extracellular matrix
FOV	Field of view
min	Minutes
mM	Millimols
mm	Millimeters
ms	Milliseconds
MRE	Magnetic resonance elastography
MRI	Magnetic resonance imaging
Pa	Pascal
PBS	Phosphate-buffered saline
PFA	Paraformaldehyde
RARE	Rapid acquisition with relaxation enhancement
RT	Room temperature
SD	Standard deviation
SGZ	Subgranluar zone
TA	Acquisition time
TE	Echo time
TR	Repetition time

Neural homeostasis, repair, and circuit function require that new neurons be formed throughout the lifespan[1,2]. In rodents, adult neurogenesis takes place in different brain regions such as the hippocampus, specifically in the subgranular zone (SGZ) of the dentate gyrus (DG). New neurons are formed from progenitor cells, whose proliferation, morphogenesis, and differentiation are tightly controlled by chemical and physical cues[3]. While chemical cues for neural stem cell differentiation, such as epidermal or fibroblast growth factors[4,5], have been extensively studied, the importance of physical control of neural development remains understudied[6]. For instance, it is known that substrate stiffness influences proliferation and differentiation of neural progenitor cells, axonal growth, branching, and maturation[7–15]; however, little is known about the viscoelastic properties of the murine SGZ in vivo.

While ex vivo methods such as atomic force microscopy (AFM) can measure the mechanical properties of hippocampus subzones with a spatial resolution on the order of a few microns[16], in vivo methods such as magnetic resonance elastography (MRE) rely on coarser scales of submillimeters in the murine brain[17] and millimeters in humans[18]. MRE uses externally induced shear waves for noninvasively probing tissue viscoelasticity as a quantitative diagnostic marker[19,20]. Although MRE lacks microscopic spatial resolution, the shear modulus of soft biological tissues is sensitive to multiscale mechanical structures from microscopic cellular dimension to macroscopic length scale[18,21–24]. Thus, macroscopic viscoelastic parameters of brain tissues are sensitive to a concert of interactions among neural cells, extracellular matrix (ECM), and vessels[25–28]. In vivo MRE has been shown to be sensitive enough to detect subtle changes in neurogenesis in the murine hippocampus induced by a Parkinson's disease model[29,30]. However, the association between MRE parameters and physiologic, adult neurogenesis in hippocampal subregions such as the neurogenic niche, the SGZ, has never been investigated. Furthermore, AFM findings in a similar region as studied before by in vivo MRE have never been correlated with neurogenic function.

Pairing AFM with MRE, on the one hand, allows us to correlate stiffness of micro tissue with the level of expression of green florescence protein (GFP)-labelled nestin, as a marker of neural progenitor[31] cells, and, thus, to directly test the mechanical properties of the neurogenic niche ex vivo. On the other hand, the study of viscoelastic properties by in vivo MRE takes into account vital processes such as blood flow[32], neural activity[33], and metabolism[32], which are absent when tissues are studied ex vivo. Therefore, here we compare AFM with in vivo MRE for the first time to test whether the coarse resolution of MRE reveals a similar mechanical signature as detected by AFM at the microscopic level and in correlation with neurogenic activity. This study aims at contributing to our understanding of the micromechanical parameters that critically shape the biophysical environment of neuronal homeostasis and repair and could be exploited for neuronal regenerative medicine in the future.

Material and methods

In vivo MRE and MRI. All animal experiments were carried out in accordance with Directive 2010/63/EU of the European Parliament and of the Council of 22 September 2010 and national and institutional guidelines for the care and use of laboratory animals and were approved by the local Animal Ethics Committee (State Office for Health and Social Affairs Berlin, Germany and State Ministry for Social Affairs and Consumer Protection, Leipzig, Germany). Methods are provided in accordance with ARRIVE guidelines. A total of 10 C57BL/6J mice (male, 9–10 weeks old) were investigated by MRE.

MRE and magnetic resonance imaging (MRI) were performed on a 7-Tesla small animal MRI scanner (Bruker BioSpec, Ettlingen, Germany). During the scans, mice were anesthetized with 1.5–2% isoflurane in 30% O_2 and 70% N_2O. The gas was administered through an anesthesia mask, and respiration was continuously monitored using a pressure-sensitive pad placed on the thorax (Small Animal Instruments Inc., Stony Brook, NY, USA). Body temperature was kept constant through warming pads integrated into the animal holder and monitored using a rectal probe. A 20-mm (mm) diameter 1H-RF transmit/receive quadrature volume coil (RAPID Biomedical, Würzburg, Germany) was used for MRI and MRE.

MRE was performed based on five consecutively induced and encoded vibration frequencies of 1000, 1100, 1200, 1300, and 1400 Hz. Vibrations were generated by a piezoceramic actuator and transmitted into the skull

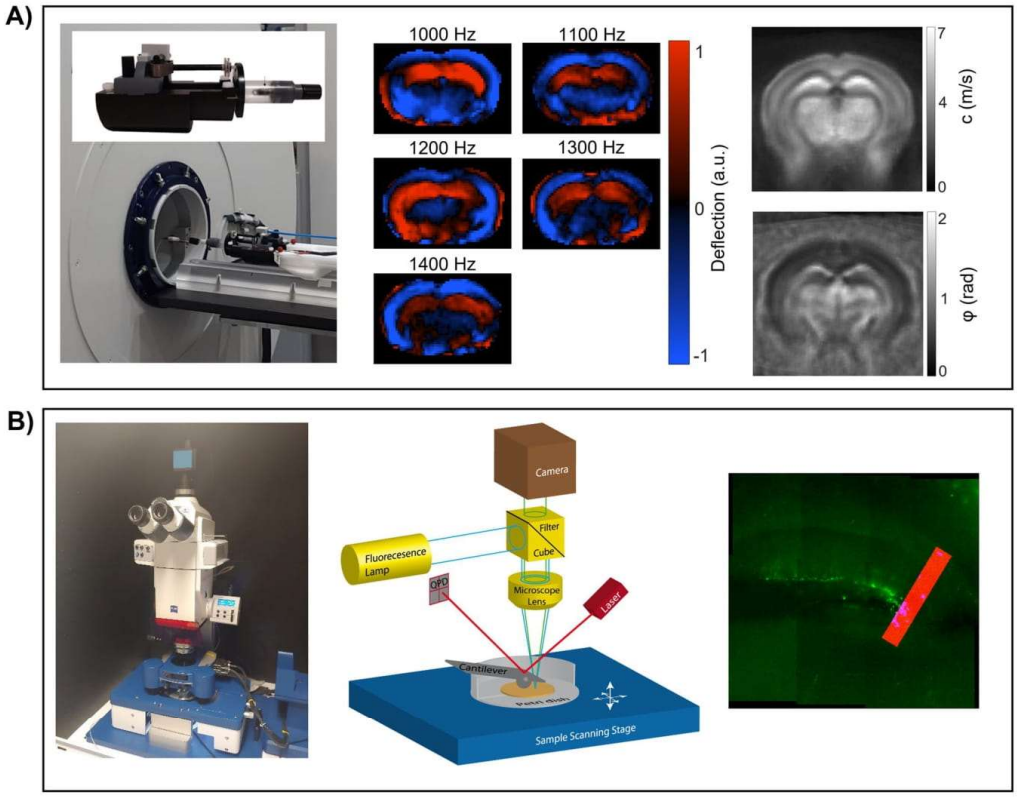

Figure 1. MRE and AFM setup. (**A**) On the left, the 7-Tesla animal scanner is shown along with customized animal holder, comprising a nonmagnetic piezoceramic actuator for wave generation, transducer rot (for wave transmission into the animal`s skull), and an anesthesia mask. In the middle, wave images showing shear wave propagation in the mouse brain at the 5 vibration frequencies (after k-MDEV inversion, 1 slice, 1 component, and no directional filters applied). On the right, a representative averaged MRE c-map and φ-map are shown. (**B**) On the left, the atomic force microscopy setup, in the middle a schematic drawing of the AFM, illustrating the main components of an AFM, and on the right, a representative image of a brain slice with a measurement profile are shown.

via a transducer rod as shown in Fig. 1A. A total of 7 coronal slices (in the Bregma areas − 2.84 mm (mm) to 0.23 mm) with 0.8 mm slice thickness were acquired using a single-shot echo-planar imaging sequence as described in detail in[17]. Further imaging parameters were: 0.18 mm × 0.18 mm in-plane resolution, echo time (TE) = 53 ms (ms), repetition time (TR) = 4000 ms, 16.2 × 10.8 mm^2 field of view (FOV), total scan time (TA) of 9 min (min). Tomoelastography postprocessing[34] was performed to derive shear wave speed (c in m/s) as a surrogate marker of stiffness, based on multifrequency wave-number analysis. To recover the phase angle of the complex shear modulus (φ in rad, also termed loss angle), Laplace-based direct multifrequency inversion was used[20]. To match AFM measurement, parameters c and φ (Fig. 1A right) were analyzed in bregma area − 2.4945 mm to − 2.0745 mm. Furthermore, c and φ were converted to shear stiffness (magnitude of the complex shear modulus |G*| in Pa) by

$$|G^*| = \frac{c^2 \rho (1 + \cos \varphi)}{2}, \tag{1}$$

assuming material density ρ = 1000 kg/m^3. For comparison with AFM-measured Young's modulus *E*, we tabulated in vivo Young's modulus $E_{MRE} = 3 \cdot |G^*|$.

For anatomical orientation, 13 coronal slices covering the Bregma areas − 2.84 to 0.23 mm were acquired with a standard T2-weighted 2D rapid acquisition with relaxation enhancement (RARE) MRI sequence. Imaging parameters were: 0.8 mm slice thickness, 0.078 mm × 0.078 mm in-plane resolution, TE = 33 ms, TR = 2500 ms,

20 mm × 20 mm FOV, 265 × 265 matrix size, RARE factor = 2, number of averages = 2, bandwidth = 34,722 Hz, and TA of 2:45 min.

Image registration and generation of masks. MRE parameter maps of c and φ and the corresponding MRE magnitude images were registered to the Allen mouse brain atlas ([35] Allen Institute for Brain Science, United States Allen Mouse Brain Atlas (2017) available from: https://mouse.brain-map.org) using ANTx2, a customized MATLAB toolbox (latest version available from https://github.com/ChariteExpMri/antx2), as described elsewhere[26]. In short, MRE parameter maps and magnitude images were 3D-coregistered and registered to each animal's T2-weighted MR image in a 2D slice-wise fashion using affine and non-linear b-spline transformations. In a next step, affine and non-linear b-spline registrations were applied to bring the animal's T2-weighted MR image to the Allen mouse brain atlas space (standard space) using ELASTIX (http://elastix.isi.uu.nl/)[36]. Finally, the MRE parameter maps and magnitude images were transformed to standard space by applying the registration parameters from the previous step.

Standard space masks of the hippocampus and DG were generated in ANTx2. To obtain a mask of Ammon´s horn, the DG mask was cut out of the hippocampus mask using MATLAB R2019b (MathWorks Inc., Natick, MA, USA). To evaluate the subzones of the DG, the masks were 2D-eroded by one, two, and three pixels from the outer DG boundaries towards the SGZ in a slice-wise fashion using the imerode function of MATLAB R2019b (MathWorks Inc., Natick, MA, USA). Standardized DG and AH masks and eroded DG masks were overlaid on MRE parameter maps in the Bregma area − 2.4945 to − 2.0745 mm.

Atomic force microscopy (AFM). Six Tg(Nes-EGFP)33Enik/J mice (male, 7–9 weeks old), expressing the green fluorescence protein (GFP) under the nestin promoter, were euthanized with an isoflurane (CP-Pharma, Burgdorf, Germany) overdose and transcardially perfused with ice cold phosphate-buffered saline (PBS). Brains were removed and placed in artificial cerebral spinal fluid (aCSF, solution I: 124 millimols (mM) sodium chloride [NaCl], 1.25 mM sodium dihydrogen phosphate [NaH_2PO_4], 10.0 mM glucose, 1.8 mM magnesium sulphate [$MgSO_4$)], 1.60 mM calcium chloride [$CaCl_2$], and 3.00 mM potassium chloride [KCl]; solution II: 26.0 mM sodium bicarbonate [$NaHCO_3$]. Solutions I and II were mixed immediately before use). Coronal brain slices of 350 µm thickness were cut, using a vibratome (Leica VT 1200, Leica Biosystems, Wetzlar, Germany) in the Bregma area − 2.4945 to − 2.0745 mm and placed on ice in a 24-well plate containing aCSF until further measurement. Next, indentation measurements were obtained by AFM (Fig. 1B) to determine the elastic properties of the hippocampus (Nanowizard4 with 300 µm hybrid stage, JPK, Berlin, Germany). Commercially available cantilevers (0.2 N/m, CONT, Nanoworld, Neuchatel, Swiss) were modified by gluing a small polystyrene bead (~ 6 µm diameter) onto the tip. During indentation measurement, the tissue was immobilized on a glass slide with surgical glue (Histoacryl, Braun, Melsungen, Germany) and placed in aCSF supplemented with synthetic air with 5% CO_2. For each slice, a profile of 10–15 adjacent maps of 100 × 100 µm with a pixel resolution of 5–10 µm (100–225 pixels) was laid over the DG, comprising the SGZ. The force curves were recorded at 20 µm/s z-speed with the setpoint of 2 nN corresponding to around 2 µm indentation. AFM force–displacement curves were transformed to the local Young's modulus using the Hertz model (F = force, E = Youngs modulus, R = tip radius, d = indentation depth):

$$F = \frac{4}{3} E \cdot R^{\frac{1}{2}} \cdot d^{\frac{3}{2}} \tag{2}$$

Supplementary Fig. 1 shows a fit of the Hertz model to experimental data and a series of experimental force-indentation curves. Total measurement time was below 2 h per slice. Fluorescence, visualizing the SGZ, was used for anatomical orientation (Fig. 1B). Young´s modulus (E in Pa) and local fluorescent intensity were acquired for each measurement point (Fig. 1B). For comparison based on local GFP expression, a threshold of relative fluorescent intensity was applied to automatically select all pixels within the AFM map which corresponded to the full width at half maximum of peak intensity within the GFP images. Elasticity values within such areas of high fluorescent signal were compared with values of the other areas which were considered of low fluorescent signal intensity. For position-based analysis, the map with the highest fluorescent intensity was selected as the central map, and averages were calculated for each map in the profile. Analysis was performed using Data Processing Software (JPK BioAFM—Bruker Nano GmbH, Berlin, Germany) and MATLAB (MathWorks Inc., Natick, MA, USA). A total of 15 measurements were performed.

Immunohistochemistry and microscopy. One Tg(Nes-EGFP)33Enik/J mouse was deeply anesthetized with ketamine/xylazine at a dose of 300 mg/kg body weight ketamine hydrochloride (Ketamine Insera, Insera Arzneimittel, Freiburg, Germany) and 30 mg/kg body weight xylazine hydrochloride (CP-Pharma, Burgdorf, Germany) administered by intraperitoneal injection. Next, the mouse was transcardially perfused with 1 M (moles per liter) PBS and 4% paraformaldehyde (PFA), and the brain was extracted. The tissue was post-fixated in PFA overnight at 4 °C and placed in 30% sucrose for 72 h. To cut the tissue in 40 µm thick slices using a cryostat (Leica CM 1850 UV, Wetzlar, Germany), brains were frozen in 2-methylbutane cooled with liquid nitrogen. The brain slices were stored in cryoprotectant solution (25% glycerol, 25% ethylene glycol, and 50% 0.1 M PBS) at 4 °C until further use.

Immunohistochemistry was performed to visualize nestin-expressing cells in the hippocampus. Free-floating brain sections were washed with PBS and placed in 10% donkey serum-enriched PBS (PBS^+) for 30 min at room temperature (RT). After blocking, sections were incubated overnight at RT with the primary antibody, anti-rabbit-GFP (1:250, Abcam, Cambridge United Kingdom) in PBS^+. On the next day, sections were washed in PBS, incubated in PBS^+ for 25 min at RT and subsequently incubated with the secondary antibody, anti-rabbit

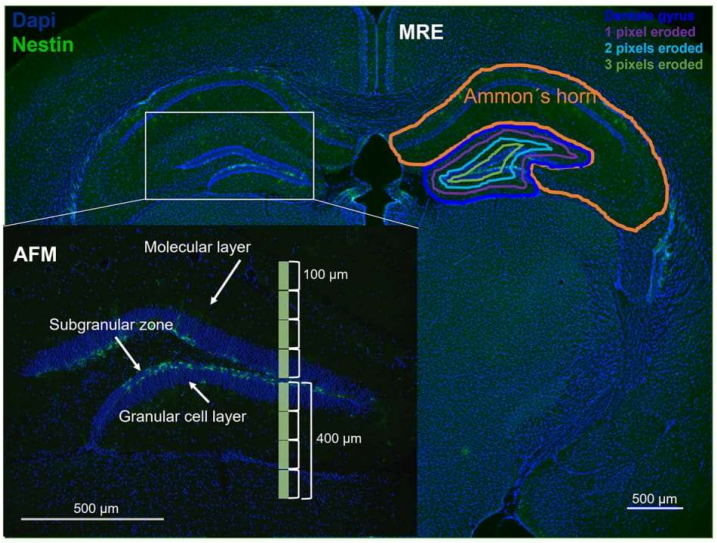

Figure 2. MRE masks and AFM measurement profiles. The MRE Ammon´s horn mask, dentate gyrus mask (DG), and DG mask eroded by 1, 2, and 3 pixels are schematically overlaid onto a histological image (magnification × 10). At the bottom, a schematic AFM measurement profile (in green) on the DG (magnification × 20). blue—DAPI (cell nuclei), green—nestin.

Alexa 488 (1:1000, Thermo Fischer Scientific, Waltham, MA, USA) for 4 h at RT. After washing, sections were incubated with PBS-diluted fluorochrome 4´6-diamidino-2-phenylindole (DAPI, 1:10,000, Thermo Fischer Scientific, Waltham, MA, USA) for 7 min to visualize cell nuclei. Tissue sections were mounted on microscope slides using ProTags PARAmount (Quartett GMBH, Berlin, Germany). Imaging was performed on a Keyence BZ-X800 microscope (Keyence, Osakaa, Japan). Images were postprocessed using BZ-X800 Analyzer software (Keyence, Osakaa, Japan).

Statistics. Statistical analysis was performed using GraphPad Prism 9.0 (GraphPad software, San Diego, CA USA). The D'Agostino & Pearson test was used to test normality. A paired t-test was used to compare in vivo AH and DG viscoelastic differences and ex vivo elastic differences of low and high fluorescence signal. Repeated measures one-way ANOVA with multiple comparisons (Tukey's multiple comparisons test) was performed to compare differences in the dentate gyrus subzone in vivo while ex vivo analysis was perfomed using a mixed model. Values are presented as mean ± standard deviation (SD). Statistical significance was defined as $p < 0.05$.

Results

Figure 2 shows examples of MRE masks along with a schematic AFM profile superimposed on a histological image of the mouse brain stained for DAPI (cell nuclei) and nestin. The SGZ in the DG is clearly identified by the expression of green fluorescence nestin in neuronal stem cells and was covered by both, in vivo MRE and ex vivo AFM measurements.

In vivo MRE is sensitive to micromechanical properties. Figure 3 shows high resolution maps of c and φ obtained by averaging individual maps after image registration to the standard atlas of the mouse brain. The DG and AH are apparent as distinct regions with lower shear wave speed c (DG = 3.2 ± 0.2 m/s *vs.* AH = 4.4 ± 0.3 m/s, $p < 0.0001$, Fig. 3A) and loss angle φ (DG 0.70 ± 0.13 rad *vs.* AH 0.77 ± 0.11 rad, $p = 0.01$, Fig. 3B) in DG than in AH.

Furthermore, Fig. 4 shows that eroding DG masks by 1, 2 and 3 pixels towards SGZ significantly reduces c, φ, and derived Young's modulus E_{MRE}. Table 1 summarizes absolute values. Relative changes are − 0.8 ± 0.9%, − 2.1 ± 1.9%, and − 1.1 ± 1.7% (one-pixel erosion), − 2.3 ± 1.7%, − 5.0 ± 4.2%, and − 3.3 ± 3.1% (two-pixel erosion), and − 3.4 ± 1.9%, − 6.9 ± 6.7% and − 5.0 ± 3.4% (three-pixel erosion) for c, φ, and derived Young's modulus E_{MRE}, respectively (significances are shown in Fig. 4).

Correlation of ex vivo AFM with GFP-expression under the nestin promoter

Neurogenic activity was quantified from the intensity of the GFP fluorescence signal, and a corresponding measurement profile was placed on the SGZ as shown Fig. 5 (left).

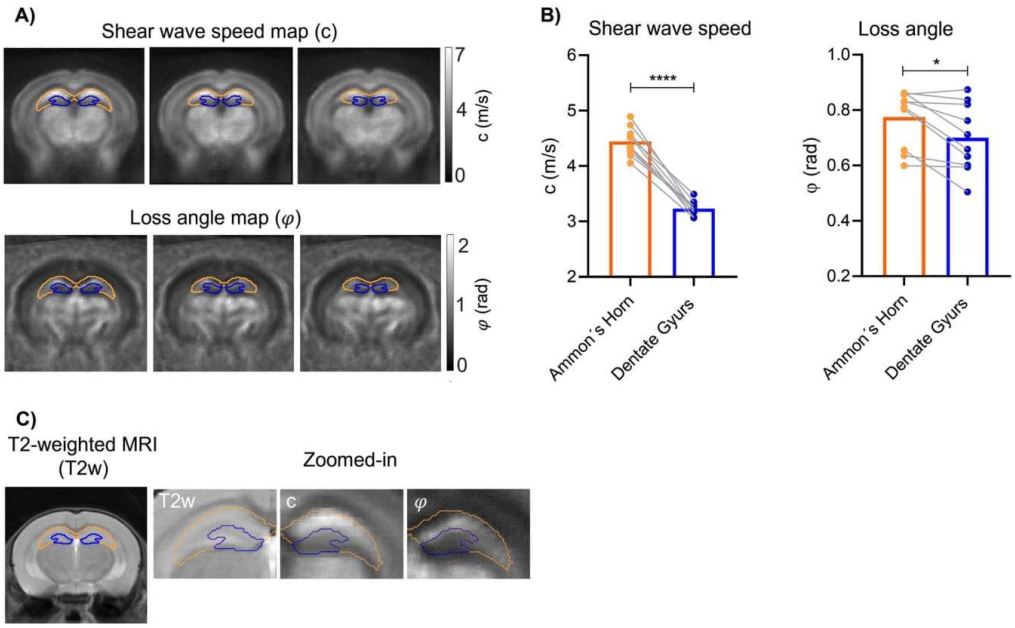

Figure 3. Regional in vivo MRE results. (**A**) Representative group averaged c- and φ-maps with Ammon´s horn (orange) and dentate gyrus (blue) masks. Image slices with distances of 210 µm correspond to the Bregma areas − 2.49, − 2.28 and − 2.07. (**B**) Group values of c and φ for Ammon´s horn and dentate gyrus (n = 10, *p = 0.0102, ****p < 0.0001). (**C**) T2-weighted MRI for anatomical orientation with magnifications of parameter maps and masks in the hippocampal region.

The 15 AFM measurements shown in Fig. 5 (right) reveal that Young's modulus E is lower in areas of high fluorescence signal (covering the SGZ) than in areas of low GFP intensity (128 ± 72 Pa *vs.* 78 ± 39 Pa, p = 0.0004, Fig. 5). Furthermore, as shown in Fig. 6, E (Pa) significantly increases with increasing distance from peak fluorescence (SGZ). As can be seen in Fig. 2, the fluorescence signals were not spatially associated with distinct changes in cell nuclear density (DAPI), suggesting that the observed softening within the SGZ was not related to the density of cell nuclei.

Absolute values are compiled in Table 1. Relative changes in E (Pa) with distance from the peak signal (SGZ) are: 71.9% at 100 µm (p = 0.0025), 110.2% at 200 µm (p < 0.0001), and 88.4% at 300 µm (p < 0.0069) while no significant change is seen at 400 µm (p = 0.0699). Figure 6 also shows MRE results for E_{MRE}, indicating consistent softening towards SGZ in vivo (significances are given in Fig. 6 and absolute values in Table 1).

Discussion

In this study, we compared AFM and MRE to investigate whether the viscoelastic properties of the murine DG in vivo reflect similar patterns of stiffness reduction as observed ex vivo in correlation with neurogenic function. In vivo MRE results show that the DG is softer than AH with markedly soft properties towards the SGZ region. Using AFM, we were able to (1) confirm the markedly soft properties of the SGZ and (2) correlate this property with GFP-labeled nestin signal, indicating the functional importance of this viscoelastic signature.

It has been shown before that MRE is sensitive to microscopic mechanical interactions such as collagen crosslinking on the nanoscale[37], tumor cell stiffness on the micrometer scale[38], and wave scattering on the sub-millimeter scale[39]. Our study now provides additional evidence about the mechanical signature of microscopic regions involved in adult neurogenesis to which in vivo MRE is potentially sensitive. The mechanical properties of these regions are highly relevant in brain pathophysiology, as demonstrated by numerous studies using in vivo elastography or ex vivo indentation methods such as AFM[29,30,40–45].

Using in vivo MRE we here show mechanical heterogeneity of the murine hippocampus between the Ammons's horn and the dentate gyrus. Consistent with our result, recent studies on human hippocampal subfields showed significant differences in stiffness[18] and damping ratio[18,24] between the dentate gyrus combined with the CA3 region and the CA1/2 subfields of the Ammon´s horn. This mechanical heterogeneity of the hippocampus, as found here by noninvasive in vivo MRE, is in agreement with previous ex vivo AFM indentation measurements showing that the DG of adult rats has softer elastic properties than the subregions of the AH[46]. Moreover, the rodent DG with its subregions has been shown to be heterogeneous in terms of stiffness as revealed by ex vivo indentation measurement[16,47]. In these studies, the granular cell layer was found to be softer than

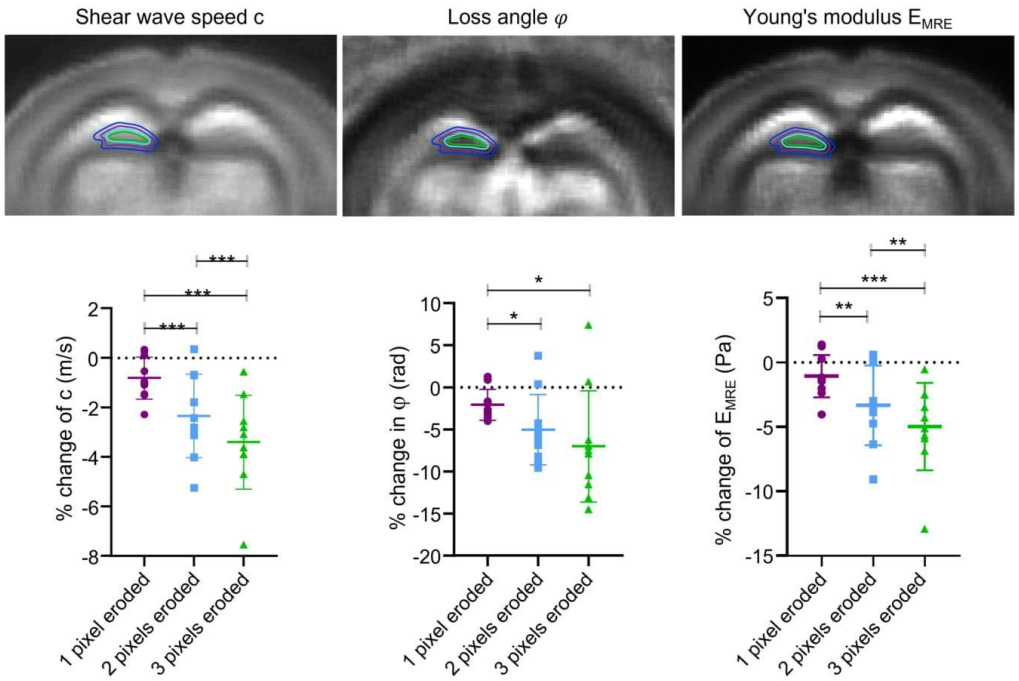

Figure 4. Eroding the dentate gyrus (DG) mask by 1, 2, and 3 pixels leads to significant decrease in viscoelastic parameters. Top, schematic mask of original DG and 1, 2, and 3 pixels eroded overlaid on averaged c-, φ- and EMRE-maps. Bottom, from left to right, percentage change in c (m/s) showing a significant decrease in c (m/s) when the DG mask is 1, 2 and 3 pixels (pixels) eroded (1 pixel eroded vs. 2 pixels eroded ***p = 0.0001, 1 pixel eroded vs. 3 pixels eroded ***p = 0.0001, 2 pixels eroded vs. 3 pixels eroded ***p = 0.0005); in the middle, percentage change in φ (rad) showing a significant decrease in φ (rad) when the DG mask is 2 and 3 pixels eroded (1 pixel eroded vs. 2 pixels eroded *p = 0.0108, 1 pixel eroded vs. 3 pixels eroded *p = 0.0270, 2 pixels eroded vs. 3 pixels eroded p = 0.0784); on the right, percentage change in EMRE (Pa) showing a significant decrease in E (Pa) when the DG mask is 1, 2 and 3 pixels eroded (1 pixel eroded vs. 2 pixels eroded **p = 0.0029, 1 pixel eroded vs. 3 pixels eroded ***p = 0.0004, 2 pixels eroded vs. 3 pixels eroded **p = 0.0046), n = 10.

MRE				AFM	
	c (m/s)	φ (rad)	E_{MRE} (kPa)		E (Pa)
Mask	Mean ± SD	Mean ± SD	Mean ± SD	Distance (µm)	Mean ± SD
Ammon's horn	4.4 ± 0.3	0.77 ± 0.11	50.8 ± 6.1	0	84 ± 40
Dentate Gyrus	3.2 ± 0.2	0.70 ± 0.13	27.7 ± 3.1	100	145 ± 82
1 pixel eroded	3.2 ± 0.2	0.68 ± 0.12	27.4 ± 3.2	200	177 ± 68
2 pixels eroded	3.2 ± 0.2	0.66 ± 0.12	26.8 ± 3.3	300	158 ± 80
3 pixels eroded	3.1 ± 0.2	0.65 ± 0.12	26.3 ± 3.3	400	142 ± 63

Table 1. Mean and standard deviation (SD) for c (m/s), φ (rad) and Young's modulus (kPa or Pa). On the left, mean and SD of c (m/s) and φ (rad) and Young's modulus ($E_{MRE} = 3 \cdot |G^*|$) of the Ammon's horn and DG masks and the DG masks reduced by 1 to 3 pixels from in vivo MRE, n = 10. On the right, mean and SD are given for distances from peak fluorescence intensity (in µm) from ex vivo AFM, 0 µm n = 15, 100 µm n = 15, 200 µm n = 15, 300 µm n = 10, 400 µm n = 5.

surrounding regions such as the hilus and the molecular layer[16,47]. Softening correlated negatively with neuronal and nuclei density[16,47] and positively with the presence of astrocytes[47]. However, these studies did not specifically examine the SGZ and most likely included the SGZ in the granular cell layer[16,47], making these results consistent with our findings of gradual softening towards the SGZ both ex vivo and in vivo. When the SGZ was examined

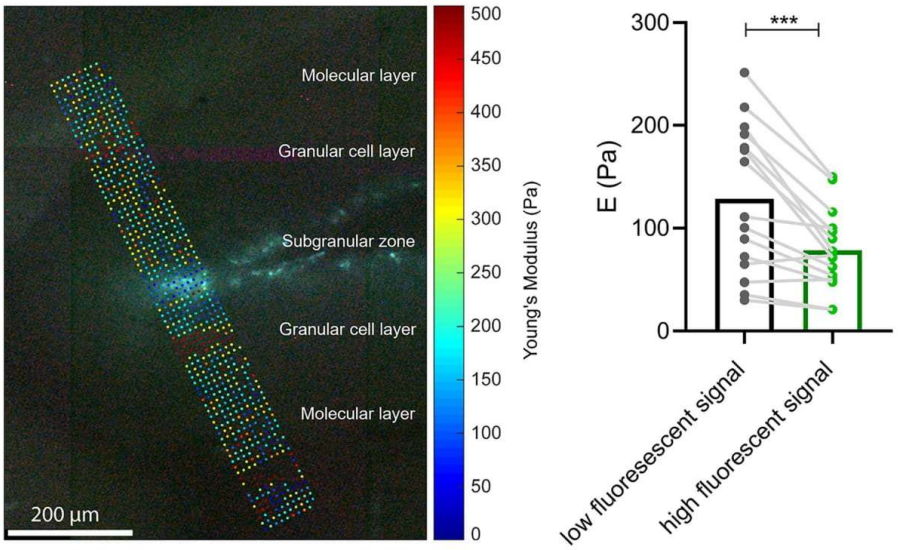

Figure 5. Ex vivo AFM results. On the left, a representative measurement profile overlaid on the high fluorescence region is shown (more data are shown in Supplementary Fig. 2). Right, the subgranular zone (area with high fluorescent signal) is significantly softer than the surrounding tissue (low fluorescent signal), n = 15, ***p = 0.0004.

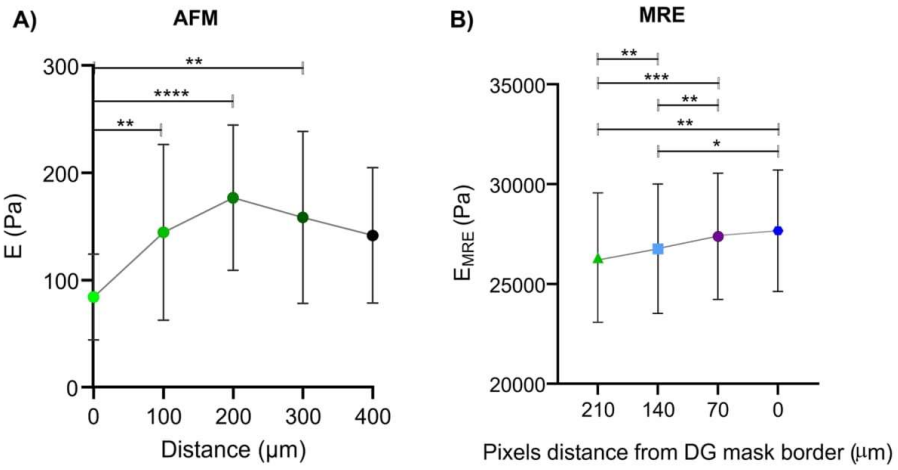

Figure 6. Comparison of ex vivo AFM and in vivo MRE results. (**A**) Stiffness increases with greater distance (in µm) from the peak of the fluorescence signal (marked as 0), 0 µm vs. 100 µm **p = 0.0025; 0 µm vs. 200 µm ****p < 0.0001; 0 µm vs. 300 µm **p = 0.0069, 0 µm n = 15, 100 µm n = 15, 200 µm n = 15, 300 µm n = 10, 400 µm n = 5. (**B**) Similar results are seen in vivo when the dentate gyrus mask is eroded: original mask (0 µm) vs. 2 pixel eroded mask (140 µm), *p = 0.0309, eroded original mask (0 µm) vs. 3 pixels eroded mask (210 µm), **p = 0.0043; 1 pixel eroded (70 µm) vs. 2 pixel eroded mask (140 µm), **p = 0.0051; 1 pixel eroded (70 µm) vs. 3 pixel eroded mask (210 µm), ***p = 0.0005; 2 pixel eroded (140 µm) vs. 3 pixel eroded mask (210 µm), **p = 0.0069), n = 10.

individually by ex vivo indentation measurement and compared directly with its surrounding structures, it also exhibited softer mechanical properties[15], which is consistent with our findings.

The relevance of tissue mechanical properties for neurogenic function is still under investigation. Other AFM studies in the subependymal zone, which is the largest neuronal stem cell niche in the rodent brain, suggest the importance of a relative stiffness gradient that directs migratory behavior and differentiation of newborn neurons[48]. Neuroblasts generated in the subependymal zone migrate via the rostral migratory stream to the olfactory bulb, where they differentiate and integrate into existing networks[49]. Migratory cells that depart from the rostral migratory stream differentiate into granule cells or periglomerular cells. These cells reside in the granule cell layer and glomerular cell layer of the olfactory bulb[49], which have been shown to be stiffer than the rostral migratory stream and the subependymal zone[48], suggesting that durotaxis is critical for neuron migration. Therefore, as a neurogenic niche, the subependymal zone can be stiffer than the non-neurogenic parenchyma as long as it has softer properties than the target region[48]. Consistent with this, our results suggest that newly formed hippocampal neurons migrate[50] from the softer SGZ into the stiffer granular cell layer of the DG.

Combined ex vivo and in vivo stiffness measurements of the murine hippocampus using invasive in vivo ultrasound-based shear-wave elasticity imaging and ex vivo AFM measurements have been performed before[51]. However, in this study, the SGZ was not analyzed separately but in conjunction with the hilus ex vivo while in vivo stiffness was measured for the whole hippocampus[51]. To our knowledge, no other study has compared the viscoelastic properties of the intact brain measured noninvasively with the spatial representation of neurogenic function. The unique combination of techniques, GFP-labeled nestin-positive cells, AFM, and MRE allowed us to match tissue stiffness in within the DG with nestin expression.

Although our results are encouraging, our study has limitations. First, direct comparison of ex vivo AFM and in vivo MRE is naturally hampered by the lacking registration of AFM images with MRE because AFM covers only small areas of the image slices obtained by MRE. Therefore, the location of the SGZ in MRE parameter maps had to be estimated, which was further impeded as standardized atlas masks of the SGZ are not yet available. In addition, we cannot fully rule out that MRE measurements were influenced by partial volume effects induced by the ventricles in the vicinity of the measured DG. However, erosion of the DG masks resulted in progressively smaller masks centered in the SGZ area and moving increasingly farther away from the boundaries. Therefore, an increase rather than a decrease in values with distance from the DG boundaries would be expected as a result of partial volume effects. Furthermore, previous MRE studies have studied regions of comparable size and border proximity to DG as analyzed here[28,29]. Possible limitations of our AFM experiments relate to sample transfer in a free-floating 24-well plate and brief contact with a clean glass surface during immobilization. In addition, absolute E-values may have been affected by the stiffness of the cantilever, the size of the beads, and indentation velocities. Nevertheless, we carefully adjusted these parameters to ensure that they were within the limits where the linear Hertz model can still be safely applied. Simulations have shown that, for spherical tips, the strain field extends about five times the penetration depth into the sample and that the penetration depth should not exceed 1/3 of the probe diameter[52]. We therefore assume that AFM measured the effective mechanical properties beneath the contact area of approximately 8 μm^2 including the first two cell layers with microenvironment. Given the consistency of our results across different samples and measurement positions, we consider our AFM data to be a robust marker of the effective stiffness beneath the cantilever tip as sensed by nestin-expressing cells. The discrepancy between the quantitative values of in vivo MRE and ex vivo AFM may be attributed to two main technical differences: First, different length scales (8 μm^2 in AFM versus 32,400 μm^2 in-plane pixel size in MRE), and, second, different dynamic ranges (quasi-static AFM versus 1–1.4 kHz MRE vibrations). While AFM values are still in the order of magnitude of those measured with MRE at low frequencies[53], MRE stiffness increases significantly from low to high frequencies due to viscoelastic dispersion[54]. Thus, the dynamic range appears to be more relevant than the scale difference, raising the prospect of using viscoelastic models in the future to match AFM and MRE over the broad dynamic range covered by both modalities.

Using ex vivo AFM, we showed here that tissue softening correlates with neurogenic signal intensity in the SGZ, and that softer properties can be found by in vivo MRE when the same region is analyzed, but at a much coarser scale. Both, in vivo MRE and ex vivo AFM, revealed consistent mechanical properties of the SGZ compared with surrounding regions. Collectively, our results contribute to the understanding of how viscoelastic tissue properties critically shape the biophysical environment that promotes neuronal proliferation, homeostasis, and repair. In the future, our results may be leveraged for neuronal regenerative medicine.

Data availability

The datasets generated during and analyzed during the current study are available from the corresponding author on reasonable request.

Received: 8 April 2022; Accepted: 22 September 2022
Published online: 06 October 2022

References

1. Steiner, B., Wolf, S. A. & Kempermann, G. Adult neurogenesis and neurodegenerative disease. *Regen. Med.* **1**(1), 15–28 (2006).
2. Kempermann, G. *et al.* Milestones of neuronal development in the adult hippocampus. *Trends Neurosci.* **27**(8), 447–452 (2004).
3. Cha, K. J. *et al.* Cell density-dependent differential proliferation of neural stem cells on omnidirectional nanopore-arrayed surface. *Sci. Rep.* **7**(1), 13077 (2017).
4. Reynolds, B. A., Tetzlaff, W. & Weiss, S. A multipotent EGF-responsive striatal embryonic progenitor cell produces neurons and astrocytes. *J. Neurosci.* **12**(11), 4565–4574 (1992).
5. Palmer, T. D., Ray, J. & Gage, F. H. FGF-2-responsive neuronal progenitors reside in proliferative and quiescent regions of the adult rodent brain. *Mol. Cell Neurosci.* **6**(5), 474–486 (1995).
6. Franze, K. & Guck, J. The biophysics of neuronal growth. *Rep. Prog. Phys.* **73**(9), 094601 (2010).

7. Jagielska, A. *et al.* Mechanical environment modulates biological properties of oligodendrocyte progenitor cells. *Stem Cells Dev.* **21**(16), 2905–2914 (2012).
8. Koser, D. E. *et al.* Mechanosensing is critical for axon growth in the developing brain. *Nat. Neurosci.* **19**(12), 1592–1598 (2016).
9. Moshayedi, P. *et al.* Mechanosensitivity of astrocytes on optimized polyacrylamide gels analyzed by quantitative morphometry. *J. Phys. Condens. Matter* **22**(19), 194114 (2010).
10. Georges, P. C. *et al.* Matrices with compliance comparable to that of brain tissue select neuronal over glial growth in mixed cortical cultures. *Biophys. J.* **90**(8), 3012–3018 (2006).
11. Chen, L. *et al.* Statistical study of biomechanics of living brain cells during growth and maturation on artificial substrates. *Biomaterials* **106**, 240–249 (2016).
12. Sur, S. *et al.* Tuning supramolecular mechanics to guide neuron development. *Biomaterials* **34**(20), 4749–4757 (2013).
13. Saha, K. *et al.* Substrate modulus directs neural stem cell behavior. *Biophys. J* . **95**(9), 4426–4438 (2008).
14. Keung, A. J. *et al.* Pan-neuronal maturation but not neuronal subtype differentiation of adult neural stem cells is mechanosensitive. *Sci. Rep.* **3**, 1817 (2013).
15. Luque, T. *et al.* Microelastic mapping of the rat dentate gyrus. *R Soc. Open Sci.* **3**(4), 150702 (2016).
16. Antonovaite, N. *et al.* Regional variations in stiffness in live mouse brain tissue determined by depth-controlled indentation mapping. *Sci. Rep.* **8**(1), 12517 (2018).
17. Bertalan, G. *et al.* Fast tomoelastography of the mouse brain by multifrequency single-shot MR elastography. *Magn. Reson. Med.* **81**(4), 2676–2687 (2019).
18. Delgorio, P. L. *et al.* Effect of aging on the viscoelastic properties of hippocampal subfields assessed with high-resolution MR elastography. *Cereb. Cortex* **31**(6), 2799–2811 (2021).
19. Venkatesh, S. K., Yin, M. & Ehman, R. L. Magnetic resonance elastography of liver: Clinical applications. *J. Comput. Assist. Tomogr.* **37**(6), 887–896 (2013).
20. Hirsch, S., Braun, J. & Sack, I. *Magnetic Resonance Elastography: Physical Background and Medical Applications* (Wiley, Hoboken, 2017).
21. Fabry, B. *et al.* Time scale and other invariants of integrative mechanical behavior in living cells. *Phys. Rev. E Stat. Nonlin Soft Matter Phys.* **68**(4 Pt 1), 041914 (2003).
22. Sack, I. *et al.* Structure-sensitive elastography: On the viscoelastic powerlaw behavior of in vivo human tissue in health and disease. *Soft Matter* **9**(24), 5672–5680 (2013).
23. Posnansky, O. *et al.* Fractal network dimension and viscoelastic powerlaw behavior: I. A modeling approach based on a coarse-graining procedure combined with shear oscillatory rheometry. *Phys. Med. Biol.* **57**(12), 4023–4040 (2012).
24. Daugherty, A. M. *et al.* Magnetic resonance elastography of human hippocampal subfields: CA3-dentate gyrus viscoelasticity predicts relational memory accuracy. *J. Cogn. Neurosci.* **32**(9), 1704–1713 (2020).
25. Schregel, K. *et al.* Demyelination reduces brain parenchymal stiffness quantified in vivo by magnetic resonance elastography. *Proc. Natl. Acad. Sci. USA* **109**(17), 6650–6655 (2012).
26. Guo, J. *et al.* Brain maturation is associated with increasing tissue stiffness and decreasing tissue fluidity. *Acta Biomater.* **99**, 433–442 (2019).
27. Wang, S. *et al.* MR elastography-based assessment of matrix remodeling at lesion sites associated with clinical severity in a model of multiple sclerosis. *Front. Neurol.* **10**, 1382 (2020).
28. Silva, R. V. *et al.* Contribution of tissue inflammation and blood-brain barrier disruption to brain softening in a mouse model of multiple sclerosis. *Front. Neurosci.* **15**, 999 (2021).
29. Hain, E. G. *et al.* Dopaminergic neurodegeneration in the mouse is associated with decrease of viscoelasticity of substantia nigra tissue. *PLoS ONE* **11**(8), e0161179 (2016).
30. Klein, C. *et al.* Enhanced adult neurogenesis increases brain stiffness: In vivo magnetic resonance elastography in a mouse model of dopamine depletion. *PLoS ONE* **9**(3), e92582 (2014).
31. Michalczyk, K. & Ziman, M. Nestin structure and predicted function in cellular cytoskeletal organisation. *Histol. Histopathol.* **20**(2), 665–671 (2005).
32. Bertalan, G. *et al.* Biomechanical properties of the hypoxic and dying brain quantified by magnetic resonance elastography. *Acta Biomater.* **101**, 395–402 (2020).
33. Patz, S. *et al.* Imaging localized neuronal activity at fast time scales through biomechanics. *Sci. Adv.* **5**(4), eaav3816 (2019).
34. Tzschätzsch, H. *et al.* Tomoelastography by multifrequency wave number recovery from time-harmonic propagating shear waves. *Med. Image Anal.* **30**, 1–10 (2016).
35. Lein, E. S. *et al.* Genome-wide atlas of gene expression in the adult mouse brain. *Nature* **445**(7124), 168–176 (2007).
36. Klein, S. *et al.* Elastix: A toolbox for intensity-based medical image registration. *IEEE Trans. Med. Imaging* **29**(1), 196–205 (2009).
37. Sauer, F. *et al.* Collagen networks determine viscoelastic properties of connective tissues yet do not hinder diffusion of the aqueous solvent. *Soft Matter* **15**(14), 3055–3064 (2019).
38. Sauer, F. *et al.* Whole tissue and single cell mechanics are correlated in human brain tumors. *Soft Matter* **17**(47), 10744–10752 (2021).
39. Lambert, S. A. *et al.* Bridging three orders of magnitude: Multiple scattered waves sense fractal microscopic structures via dispersion. *Phys. Rev. Lett.* **115**(9), 094301 (2015).
40. Gerischer, L. M. *et al.* Combining viscoelasticity, diffusivity and volume of the hippocampus for the diagnosis of Alzheimer's disease based on magnetic resonance imaging. *NeuroImage Clin.* **18**, 485–493 (2018).
41. Sandroff, B. M., Johnson, C. L. & Motl, R. W. Exercise training effects on memory and hippocampal viscoelasticity in multiple sclerosis: A novel application of magnetic resonance elastography. *Neuroradiology* **59**(1), 61–67 (2017).
42. Huesmann, G. R. *et al.* Hippocampal stiffness in mesial temporal lobe epilepsy measured with MR elastography: Preliminary comparison with healthy participants. *Neuroimage Clin.* **27**, 102313 (2020).
43. Majumdar, S. & Klatt, D. Longitudinal study of sub-regional cerebral viscoelastic properties of 5XFAD Alzheimer's disease mice using multifrequency MR elastography. *Magn. Reson. Med.* **86**(1), 405–414 (2021).
44. Antonovaite, N. *et al.* Mechanical alterations of the hippocampus in the APP/PS1 Alzheimer's disease mouse model. *J. Mech. Behav. Biomed. Mater.* **122**, 104697 (2021).
45. Zhao, W. *et al.* Examination of Alzheimer's disease by a combination of electrostatic force and mechanical measurement. *J. Microsc.* **275**(1), 66–72 (2019).
46. Elkin, B. S., Ilankovan, A. & Morrison, B. 3rd. Age-dependent regional mechanical properties of the rat hippocampus and cortex. *J. Biomech. Eng.* **132**(1), 011010 (2010).
47. Antonovaite, N. *et al.* Viscoelastic mapping of mouse brain tissue: Relation to structure and age. *J. Mech. Behav. Biomed. Mater.* **113**, 104159 (2021).
48. Kjell, J. *et al.* Defining the adult neural stem cell niche proteome identifies key regulators of adult neurogenesis. *Cell Stem Cell* **26**(2), 277–293 (2020).
49. Lim, D. A. & Alvarez-Buylla, A. The adult ventricular–subventricular zone (V-SVZ) and olfactory bulb (OB) neurogenesis. *Cold Spring Harb. Perspect. Biol.* **8**(5), a018820 (2016).
50. Ming, G.-L. & Song, H. Adult neurogenesis in the mammalian brain: Significant answers and significant questions. *Neuron* **70**(4), 687–702 (2011).

51. Ryu, Y. *et al.* A shift in tissue stiffness during hippocampal maturation correlates to the pattern of neurogenesis and composition of the extracellular matrix. *Front. Aging Neurosci.* **13**, 491 (2021).
52. Yoo, Y.-H., Lee, W. & Shin, H. Spherical nano-indentation of a hard thin film/soft substrate layered system: II. Evolution of stress and strain fields. *Model. Simul. Mater. Sci. Eng.* **12**(1), 69–78 (2003).
53. Herthum, H. *et al.* Superviscous properties of the in vivo brain at large scales. *Acta Biomater.* **121**, 393–404 (2021).
54. Bertalan, G.T.H., Franze, K., Budday, S. & Sack, I. In *Viscosity Reconciles Seemingly Disparate Stiffness Measurements Under Static and Dynamic Conditions* (CMBBE, Bonn, 2021).

Author contributions

A.S.M. experimental design, acquisition of the data, analysis and interpretation. preparation of figures and wrote the original manuscript, M.N. acquisition of the data, technical assistance and writing/editing of the manuscript, GB acquisition of the data, technical assistance and writing/editing, R.V.S. technical assistance and writing/editing of the manuscript, C.I.D. writing and editing of the manuscript and funding acquisition. S.P.K. technical assistance, data analysis and writing/editing of the manuscript, PBS technical assistance and writing/editing of the manuscript, UK resources and writing and editing of the manuscript. J.B. writing/editing of the manuscript and funding acquisition, B.S. conceptualization, resources and writing/editing of the manuscript, J.A.K. resources and writing/editing of the manuscript. T.F. experimental design, acquisition of the data and analysis, interpretation, preparation of figures and writing/editing, I.S. conceptualization, data interpretation, editing/writing of the manuscript, resources, funding acquisition, project administration, and supervision.

Funding

Open Access funding enabled and organized by Projekt DEAL. Funding from the Deutsche Forschungsgemeinschaft (DFG, German Research Foundation, SFB 1340 and BIOQIC GRK2260) and ERC (ERC Advanced 741350) is gratefully acknowledged. Funding to SPK and PBS was provided by the German Federal Ministry of Education and Research under the ERA-NET NEURON scheme (BMBF 01EW1811) and the German Research Foundation (DFG, Project BO 4484/2-1, Sa901/17-2 and EXC NeuroCure).

Competing interests

The authors declare no competing interests.

Additional information

Supplementary Information The online version contains supplementary material available at https://doi.org/10.1038/s41598-022-21105-7.

Correspondence and requests for materials should be addressed to I.S.

Reprints and permissions information is available at www.nature.com/reprints.

Publisher's note Springer Nature remains neutral with regard to jurisdictional claims in published maps and institutional affiliations.

Publication 2

Rafaela Vieira Silva*, **Anna S. Morr***, Susanne Mueller, Stefan Paul Koch, Philipp Boehm-Sturm, Yasmina Rodriguez-Sillke, Désirée Kunkel, Heiko Tzschätzsch, Anja A. Kühl, Jörg Schnorr, Matthias Taupitz, Ingolf Sack and Carmen Infante-Duarte, Contribution of Tissue Inflammation and Blood-Brain Barrier Disruption to Brain Softening in a Mouse Model of Multiple Sclerosis, Frontiers in Neuroscience, 2021

* Rafaela Vieira Silva and Anna S. Morr contributed equally to this work and share the first authorship

Journal Data Filtered By: **Selected JCR Year: 2019** Selected Editions: SCIE,SSCI
Selected Categories: **"NEUROSCIENCES"** Selected Category Scheme: WoS
Gesamtanzahl: 271 Journale

Rank	Full Journal Title	Total Cites	Journal Impact Factor	Eigenfactor Score
1	NATURE REVIEWS NEUROSCIENCE	42,809	33.654	0.055400
2	NATURE NEUROSCIENCE	62,933	20.071	0.144390
3	BEHAVIORAL AND BRAIN SCIENCES	9,395	17.333	0.008170
4	TRENDS IN COGNITIVE SCIENCES	27,705	15.218	0.036050
5	JOURNAL OF PINEAL RESEARCH	10,537	14.528	0.009430
6	NEURON	95,056	14.415	0.199640
94	EUROPEAN NEUROPSYCHOPHARMACOLOGY	7,597	3.853	0.013120
95	JOURNAL OF NEUROTRAUMA	15,388	3.793	0.021530
96	Frontiers in Neuroscience	17,395	3.707	0.049650

frontiers in Neuroscience

ORIGINAL RESEARCH
published: 23 August 2021
doi: 10.3389/fnins.2021.701308

Contribution of Tissue Inflammation and Blood-Brain Barrier Disruption to Brain Softening in a Mouse Model of Multiple Sclerosis

Rafaela Vieira Silva[1,2†], Anna S. Morr[3†], Susanne Mueller[4,5], Stefan Paul Koch[4,5], Philipp Boehm-Sturm[4,5], Yasmina Rodriguez-Sillke[6], Désirée Kunkel[6], Heiko Tzschätzsch[3], Anja A. Kühl[7], Jörg Schnorr[3], Matthias Taupitz[3], Ingolf Sack[3‡] and Carmen Infante-Duarte[1,2,8‡]*

[1] Charité - Universitätsmedizin Berlin, Corporate Member of Freie Universität Berlin and Humboldt-Universität zu Berlin, Institute of Medical Immunology, Berlin, Germany, [2] Charité - Universitätsmedizin Berlin, Einstein Center for Neurosciences Berlin, Berlin, Germany, [3] Charité - Universitätsmedizin Berlin, Corporate Member of Freie Universität Berlin and Humboldt-Universität zu Berlin, Department of Radiology, Berlin, Germany, [4] Charité - Universitätsmedizin Berlin, Corporate Member of Freie Universität Berlin and Humboldt-Universität zu Berlin, Department of Experimental Neurology and Center for Stroke Research, Berlin, Germany, [5] Charité - Universitätsmedizin Berlin, NeuroCure Cluster of Excellence and Charité Core Facility 7T Experimental MRIs, Berlin, Germany, [6] Berlin Institute of Health at Charité - Universitätsmedizin Berlin, Flow & Mass Cytometry Core Facility, Berlin, Germany, [7] Charité - Universitätsmedizin Berlin, Corporate Member of Freie Universität Berlin and Humboldt-Universität zu Berlin, Berlin, Germany, [8] Charité - Universitätsmedizin Berlin, Corporate Member of Freie Universität Berlin and Humboldt-Universität zu Berlin, ECRC Experimental and Clinical Research Center, Berlin, Germany

OPEN ACCESS

Edited by:
Nathalie Just,
INRA Centre Val de Loire, France

Reviewed by:
Emmanuelle Canet Soulas,
Université Claude Bernard Lyon 1, France
Max Masthoff,
University Hospital Münster, Germany

***Correspondence:**
Carmen Infante-Duarte
carmen.infante@charite.de

†These authors have contributed equally to this work and share first authorship

‡These authors have contributed equally to this work and share senior authorship

Specialty section:
This article was submitted to Brain Imaging Methods, a section of the journal Frontiers in Neuroscience

Received: 27 April 2021
Accepted: 19 July 2021
Published: 23 August 2021

Citation:
Silva RV, Morr AS, Mueller S, Koch SP, Boehm-Sturm P, Rodriguez-Sillke Y, Kunkel D, Tzschätzsch H, Kühl AA, Schnorr J, Taupitz M, Sack I and Infante-Duarte C (2021) Contribution of Tissue Inflammation and Blood-Brain Barrier Disruption to Brain Softening in a Mouse Model of Multiple Sclerosis. Front. Neurosci. 15:701308. doi: 10.3389/fnins.2021.701308

Neuroinflammatory processes occurring during multiple sclerosis cause disseminated softening of brain tissue, as quantified by *in vivo* magnetic resonance elastography (MRE). However, inflammation-mediated tissue alterations underlying the mechanical integrity of the brain remain unclear. We previously showed that blood-brain barrier (BBB) disruption visualized by MRI using gadolinium-based contrast agent (GBCA) does not correlate with tissue softening in active experimental autoimmune encephalomyelitis (EAE). However, it is unknown how confined BBB changes and other inflammatory processes may determine local elasticity changes. Therefore, we aim to elucidate which inflammatory hallmarks are determinant for local viscoelastic changes observed in EAE brains. Hence, novel multifrequency MRE was applied in combination with GBCA-based MRI or very small superparamagnetic iron oxide particles (VSOPs) in female SJL mice with induced adoptive transfer EAE (n = 21). VSOPs were doped with europium (Eu-VSOPs) to facilitate the *post-mortem* analysis. Accumulation of Eu-VSOPs, which was previously demonstrated to be sensitive to immune cell infiltration and ECM remodeling, was also found to be independent of GBCA enhancement. Following registration to a reference brain atlas, viscoelastic properties of the whole brain and areas visualized by either Gd or VSOP were quantified. MRE revealed marked disseminated softening across the whole brain in mice with established EAE (baseline: 3.1 ± 0.1 m/s vs. EAE: 2.9 ± 0.2 m/s, $p < 0.0001$). A similar degree of softening was observed in sites of GBCA enhancement i.e., mainly within cerebral cortex and brain stem (baseline: 3.3 ± 0.4 m/s vs. EAE: 3.0 ± 0.5 m/s, $p = 0.018$).

However, locations in which only Eu-VSOP accumulated, mainly in fiber tracts (baseline: 3.0 ± 0.4 m/s vs. EAE: 2.6 ± 0.5 m/s, $p = 0.023$), softening was more pronounced when compared to non-hypointense areas (percent change of stiffness for Eu-VSOP accumulation: −16.81 ± 16.49% vs. for non-hypointense regions: −5.85 ± 3.81%, $p = 0.048$). Our findings suggest that multifrequency MRE is sensitive to differentiate between local inflammatory processes with a strong immune cell infiltrate that lead to VSOP accumulation, from disseminated inflammation and BBB leakage visualized by GBCA. These pathological events visualized by Eu-VSOP MRI and MRE may include gliosis, macrophage infiltration, alterations of endothelial matrix components, and/or extracellular matrix remodeling. MRE may therefore represent a promising imaging tool for non-invasive clinical assessment of different pathological aspects of neuroinflammation.

Keywords: magnetic resonance elastography, Eu-VSOP, gadolinium, neuroinflammation, experimental autoimmune encephalomyelitis, BBB disruption, multiple sclerosis

INTRODUCTION

Multiple sclerosis (MS) is a chronic autoimmune disease in which myelin-autoreactive immune cells gain access to the central nervous system (CNS) *via* the blood-brain barrier (BBB) and the blood-cerebrospinal fluid barrier (Alvarez et al., 2011). This infiltration results in the formation of multiple focal lesions that involve both white and gray matter and contribute to demyelination and neurodegeneration. Demyelinating plaques are seen as hyperintense areas by T2-weighted magnetic resonance imaging (MRI), whereas inflammation-associated BBB leakage is revealed by hyperintensity in contrast agent-based T1-weighted images (Thompson et al., 2018).

Due to their intrinsic magnetic properties, gadolinium-based contrast agents (GBCAs) have long been used as contrast agents for MRI. GBCAs induce signal changes in T2, T2* and T1-weighted MRI by affecting the relaxation time of water protons in biological tissues. The appearance of hyperintense widespread Gd-enhanced areas has become the standard MRI marker of loss of BBB integrity on T1-weighted MRI. Because BBB leakage was found to predict the formation of new non-focal white matter lesions, GBCA enhancement reflecting inflammatory activity is widely used in MS diagnosis (Lassmann, 2008; Zéphir, 2018). However, studies on the potential accumulation of Gd into the tissue, including the CNS, after repeated administration of GBCAs, in particular linear GBCAs, raised concerns about their safety (Layne et al., 2018). Furthermore, a discrepancy between the presence of Gd-enhancing lesions and clinical manifestations in both, MS and its animal model, the experimental autoimmune encephalomyelitis (EAE), has been reported (Lassmann, 2008) (Wuerfel et al., 2007, 2010; Tysiak et al., 2009; Wang et al., 2019). This discrepancy, referred to as a clinical-radiological paradox, motivates the quest for reliable imaging tools in neuroinflammation.

An evolving imaging strategy for visualizing neuroinflammation is based on the application of very small iron oxide particles (VSOPs) (Tysiak et al., 2009; Millward et al., 2013). VSOPs have a hydrodynamic diameter of only 7 nm and are stabilized with a citrate coating (Taupitz et al., 2000; Wagner et al., 2002). The iron causes strong susceptibility changes, which give rise to hypointense areas in T1-, T2- and T2*-weighted MR images, but appears to be best visualized by T2*weighted MRI (Tysiak et al., 2009; Millward et al., 2013, 2019). Previous work in EAE has demonstrated that VSOPs administered *in vivo* intravenously can be phagocytosed locally or transported within cells to areas of inflammation and/or appear freely diffused in the brain parenchyma or bound to endothelial cells (Tysiak et al., 2009; Millward et al., 2013, 2019; Berndt et al., 2017). Therefore, VSOPs do not only visualize BBB breakdown in areas of Gd-enhancement but additionally detect other inflammatory mechanisms that were not detected by conventional GBCA-enhanced MRI, such as myeloid cell infiltrates, changes in the extracellular matrix (ECM) or alteration of the endothelial glycocalyx (Tysiak et al., 2009; Millward et al., 2013, 2019; Berndt et al., 2017).

At the same time, magnetic resonance elastography (MRE) (Muthupillai et al., 1995) has evolved as a non-invasive tool for detecting inflammation-associated pathologies (Muthupillai et al., 1995; Plewes et al., 1995; Schregel et al., 2012; Hiscox et al., 2016). It is already well documented that neuroinflammation modifies the viscoelastic properties of neuronal tissue, reducing stiffness throughout larger brain areas (Wuerfel et al., 2010; Streitberger et al., 2012) (Riek et al., 2012; Millward et al., 2015; Fehlner et al., 2016; Wang et al., 2020). MRE uses harmonic vibrations to transmit shear waves into the tissue of interest (Manduca et al., 2021). Wave propagation is detected using motion-sensitive MRI, from which viscoelastic parameters such as stiffness (magnitude shear modulus or shear wave speed) and fluidity (viscosity, dispersion angle or loss angle of the shear modulus) are derived (Hirsch et al., 2017). We previously demonstrated in the active EAE model that MRE does not appear to correlate with GBCA enhancement in MRI. However, in this study, we could not provide an accurate regional analysis due to the limitation of the MRE tools (Wang et al., 2020). The recent development of multifrequency MRE with tomoelastography postprocessing in small animal models fosters high-resolution

MRE of the mouse brain with multiple imaging slices that reveal deeper anatomical details (Bertalan et al., 2019), enabling a more accurate investigation of the mechanisms underlying brain softening in inflamed areas.

Therefore, in this study, we aimed at uncovering how neuroinflammatory processes such as blood-brain barrier leakage and focal inflammation are associated with changes in the mechanical properties detected by multifrequency MRE. To optimize the study, here we use a model of adoptive transfer EAE, which contrary to the active EAE used in Wang et al., 2020 (Wang et al., 2020) develops numerous and large brain lesions. We hypothesize that novel tomoelastography sensitively detects mechanical changes in sites of intense neuroinflammation that are revealed by VSOP-deposits. Those sites are known to be characterized by enhanced myeloid cell activity (Millward et al., 2013), alterations of the glycocalyx on barrier cells (Berndt et al., 2017) and ECM remodeling (Wang et al., 2020). To test our hypothesis, we combined *in vivo* viscoelasticity measured by multifrequency MRE with both, GBCA- and VSOP- MRI, in the adoptive transfer EAE model. We used VSOPs doped with europium (Eu) in order to improve histological detection of the particles in biological tissues, without the interference of endogenous iron (de Schellenberger et al., 2017).

MATERIALS AND METHODS

Animals and Adoptive Transfer EAE Induction

All animal experiments were conducted in accordance with national and institutional guidelines for the care and use of laboratory animals and with directive 2010/63/EU of the European Parliament and of the Council of 22 September 2010 and were approved by the Berlin State Office for Health and Social Affairs (LAGeSo, registration number G106/19).

Adoptive transfer EAE was induced by transfer of myelin proteolipid protein (PLP)-reactive lymphocytes into two cohorts of adult female SJL mice, 9–12 weeks old (n = 21 mice in total; Janvier, SAS, France). EAE is more effectively induced in females than in male animals (Miller and Karpus, 2007), therefore in all our previous studies and also in this study we included only female mice in the experiments. To obtain PLP-reactive lymphocytes, a donor group of mice (n = 22) was actively immunized with 200 μg of the myelin peptide PLP139-151 emulsified with 200 μl complete Freund's adjuvant (Thermo Fischer Scientific, United States) and 800 μg Mycobacterium tuberculosis H37Ra (Difico, United States) as previously described (Millward et al., 2013). Additionally, 250 ng pertussis toxin (List Biological Laboratories, United States) was injected intraperitoneally on days 0 and 2. On day 10 post-immunization, animals were sacrificed, inguinal and axillary lymph nodes were collected, and the cells were cultured as previously described (Plewes et al., 1995). After 4 days in culture with RPMI 1640 medium (supplemented with 2 mM L-glutamine, 100 units/ml penicillin, 100 μg/ml streptomycin and 10% fetal bovine serum) (Gibco, Thermo Fischer Scientific) containing 12.5 μg/ml PLP, lymph node cells were harvested, and 30 million cells were injected intraperitoneally into each recipient mouse. After immunization, mice were monitored daily for signs of disease, which were scored as follows: 0—no sign, 0.5—tail paresis, 1—tail paresis and/or plegia and righting reflex weakness; 2—hind limb paresis; 3—paraplegia; 4—paraplegia with forelimb weakness or paralysis; 5—moribund or dead animal. To comply with animal welfare guidelines, all mice with a score greater than 3 or with atypical signs of EAE were euthanized and removed from the study before the second T2*-weighted MRI (n = 8).

In vivo Scans and Experimental Set-Up

In vivo scans were performed at two timepoints, prior to EAE induction (baseline control) and after EAE signs were established, i.e., animals showed at least partial hind limb paresis (score 1.75) (**Figure 1A**). For each single animal, EAE scan was compared to the corresponding baseline scan, while imaging post-contrast was compared to the corresponding pre-contrast image. In EAE animals, MRE was first performed followed by pre-contrast MRI with a T1-weighted imaging, a T2-weighted sequence to acquire an anatomical image, and a pre-contrast T2*-weighted sequence. Thereafter, GBCA (0.2 mmol/kg, Magnevist, Bayer-Schering AG) was administered *via* the tail vein, and post-contrast T1-weighted images were acquired, At the end of the scans, 0.2 mmol/kg Eu-VSOPs [batch RH030812 Eu-R; c(Fe) = 0.134 mol/L] were intravenously injected into the tail vein, and 24 h later, a T2*-weighted sequence was acquired to visualize particle accumulation. The applied Eu-VSOP and Magnevist doses as well as the time between injections and scans were defined based on our previous studies (Wuerfel et al., 2007; Tysiak et al., 2009; Millward et al., 2013, 2019; Wang et al., 2020). No GBCA or Eu-VSOPs were administered at baseline. Eu-VSOPs were produced and provided by the Experimental Radiology working group of the Department of Radiology, Charité - Universitätsmedizin Berlin as described previously (de Schellenberger et al., 2017).

MRI and MRE examinations were performed in a preclinical 7 Tesla MRI scanner (BioSpec, Bruker, Ettlingen, Germany) running with ParaVision 6.1 software. All scans were acquired with a 20-mm diameter 1H-RF quadrature volume coil (RAPID Biomedical, Würzburg, Germany). For acquisitions, mice were placed on a custom-built animal holder (**Figure 1B**) and anesthetized with 1.5–2.0% isoflurane in 30% O_2 and 70% N_2O administered *via* an anesthesia mask during continuous respiratory monitoring using a pressure-sensitive pad placed on the thorax (Small Animal Instruments Inc., Stony Brook, NY, United States). Body temperature was kept constant by circulating water through warming pads integrated into the animal holder, and body temperature was monitored using a rectal probe.

MRI

Coronal anatomical images were acquired using a T2-weighted 2D-RARE sequence with repetition time (TR) = 3,500 ms, effective echo time (TE) = 33 ms, echo spacing (DTE) = 11 ms, RARE factor = 8, 4 averages, 32 contiguous slices with a slice thickness of 0.5 mm, field of view (FOV) = 18 mm × 18 mm, matrix size MTX = 180 × 180, in-plane resolution

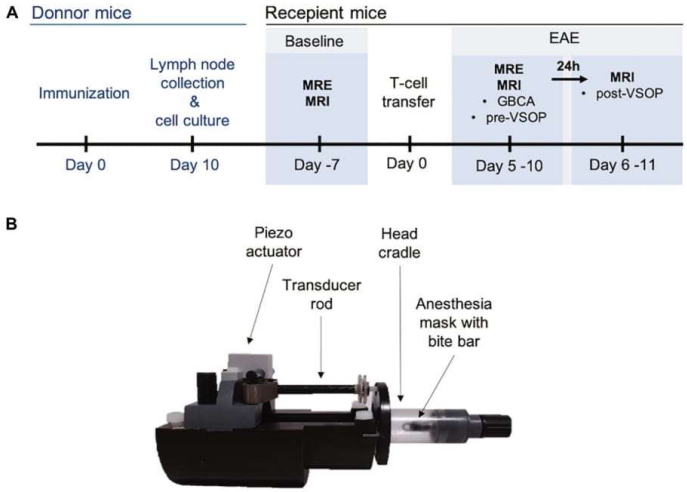

FIGURE 1 | Experimental set-up. **(A)** Timeline depicting induction of adoptive transfer EAE and *in vivo* scans at baseline, before immunization, and after establishment of EAE. **(B)** Custom-made animal holder. A piezo actuator generates the mechanical waves, which are transmitted *via* the transducer to the head cradle and into the skull of the mouse.

0.1 mm × 0.1 mm × 0.5 mm, bandwidth BW = 34,722 Hz, and total acquisition time TA = 5:08 min). GBCA-enhanced images were acquired using a T1-weighted RARE sequence with TR = 800 ms, TE = 6.5 ms, (DTE) = 6.5 ms, RARE factor = 2, 6 averages, BW = 75,000 Hz, and the same geometry as for the T2w scan resulting in a total acquisition time of TA = 7:12 min. To visualize Eu-VSOP accumulation, a T2*-weighted FLASH sequence was used with TR = 400 ms, TE = 2.5 ms, flip angle = 30 deg, 3 averages, BW = 29,762 Hz, and the same geometry as for the T2w scan with a total acquisition time of TA = 2:24 min.

MRE

To induce shear waves in the mouse brain, vibrations were generated with a custom-made driver system using a non-magnetic piezoceramic actuator. Vibrations were transmitted *via* a transducer rod to the head cradle and into the skull of the anesthetized and fixated mouse (**Figure 1B**). The MRE technique used in this study has been described in more detail elsewhere (Bertalan et al., 2019). In short, multifrequency MRE was performed, and wave images (**Figure 2**) were acquired using 5 frequencies (1,000, 1,100, 1,200, 1,300, and 1,400 Hz). In the bregma areas −2.84 mm to 0.23 mm, 7 coronal slices with a slice thickness of 0.8 mm and a 0.18 mm × 0.18 mm in-plane resolution were acquired. We limited our analysis to this area for consistency with previous studies using tomoelastography (Bertalan et al., 2019, 2020; Guo et al., 2019), as well as to reduce scan time while focusing on multifrequency studies. Further imaging parameters were: TA = 9 min, TE = 53 ms, TR = 4,000 ms, FOV = 16.2 mm × 10.8 mm, and matrix size = 90 × 60.

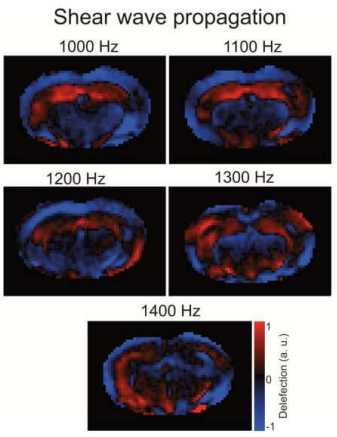

FIGURE 2 | Representative wave images. Propagation of shear waves through the mouse brain after *k*-MDEV inversion (1 slice, 1 component, 5 frequencies, and no directional filters applied). The image was taken from a mouse after immunization.

For analysis, tomoelastography postprocessing (Tzschätzsch et al., 2016) based on multifrequency wave-number analysis was used to derive shear wave speed (c in m/s) as a surrogate marker of stiffness. In addition, Laplacian-based direct multifrequency inversion (Hirsch et al., 2017) was used to recover the phase angle of the complex shear modulus (ϕ in rad, also known as

loss angle) as a measure of the solid-fluid behavior of biological tissues. Averaged c- and ϕ-maps showing the brain area covered by MRE (from bregma −2.84 to 0.23 mm) are provided in **Supplementary Figure 1**.

Data Analysis

Registration to the Allen Brain Atlas

ANTx, a customized MATLAB toolbox (latest version available under [1]), was used for MRI and MRE image registration, as described elsewhere (Koch et al., 2019). In short, for MRI, T2-weighted RARE images, pre- and postcontrast T1-weighted RARE, and T2*-weighted FLASH images were transferred into the Allen mouse brain atlas space (Allen Institute for Brain Science, United States) using ELASTIX [2](Klein et al., 2009). Next, the pre- and postcontrast T1-weighted RARE and the pre- and postcontrast T2*-weighted FLASH images were co-registered and resliced to the T2-weighted RARE image using affine transformation.

For image registration of the MRE parameter maps to the brain atlas, the individual magnitude images and the parameter maps, c and ϕ, were first 3D-coregistered and 2D-slice wise registered to the to the T2-weighted TurboRare images using affine non-linear b-spline transformation. Finally, the image transformation found for MRI was used to transform MRE images into the Allen mouse brain atlas space (Guo et al., 2019). All acquired 7 MRE slices were interpolated to 215 slices of the reference atlas, generating approx. 58 corresponding MRE slices. Consequently, all acquired scans were aligned to the Allen mouse brain atlas, making it possible to locate and compare identified areas of Gd-enhancement and Eu-VSOP accumulation between the different imaging modalities.

Generation of Masks

Masks corresponding to areas of Gd-enhancement and Eu-VSOP accumulation were manually drawn on registered postcontrast T1-weighted and T2*-weighted images by two experienced researchers using the ANALYZE 10.0 program (Biomedical Imaging Resources Mayo Clinic). For masks depicting Gd-enhancement, maps showing percentage changes in signal intensity (SI) were calculated by subtracting the postcontrast from the precontrast T1-weighted image using Image J 1.52e ([3]National Institutes of Health, United States). Eu-VSOP masks were drawn on the postcontrast T2*-weighted images. Then, all masks were registered to the Allen mouse brain atlas using ELASTIX.

As the sites of particle accumulation appear as focal hypointense areas, and the current MRE resolution is 0.18 mm × 0.18 mm, it was necessary to dilate the Eu-VSOP masks by two pixels using Matlab to reduce effects of single-pixel artifacts [Version 9.7 (R2019b); Natick, Massachusetts: The MathWorks Inc.]. Eu-VSOP areas were excluded from GBCA masks and vice versa in order to obtain masks corresponding solely to areas with either Gd-enhancement or Eu-VSOP accumulation. Individual ventricle masks, manually drawn on registered MRE magnitude images, were excluded from the GBCA and Eu-VSOP masks to eliminate the ventricles from the maps, as mechanical wave propagation is not ensured in liquid-filled spaces. In order to establish MRE parameter maps of areas with alterations detected exclusively by one of the MRI modalities (either by GBCA or Eu-VSOP), areas marked in both, GBCA-based and Eu-VSOP-based MRI, were disregarded. Mean values for stiffness and fluidity were obtained by overlaying the masks on the MRE parameter maps (c-map and ϕ-map).

Gadolinium-based contrast agent masks generated from percentage change T1-weighted images and Eu-VSOP masks drawn on (unregistered) T2*-weighted images were used to create incidence maps using the ANTx toolbox in order to illustrate the prevalence of inflammation detected by either GBCA or Eu-VSOPs.

Statistical Analysis

Paired *t*-tests were applied to shear wave speed (c) and phase angle (ϕ) mean values of mask obtained from the MRE parameter maps using GraphPad Prism 9.0 (GraphPad software, La Jolla, CA, United States). Normality was tested using the D'Agostino-Pearson test. If one of the two compared groups did not pass the normality test, the Wilcoxon matched-pairs signed rank test was used. Differences were considered to be statistically significant for p-values < 0.05.

Histology and Imaging Mass Cytometry

Imaging Mass Cytometry™ (IMC) was used to identify the surroundings of the particles within the inflamed tissue by using lanthanide-tagged antibodies and the Eu incorporated into the nanoparticle cores to label VSOPs. Therefore, after the last MRI scan, animals were sacrificed with an overdose of ketamine/xylazine and immediately transcardially perfused with 4% paraformaldehyde (PFA) (Carl Roth®, Germany). In addition, a healthy mouse without Eu-VSOP administration was used as control. The brains were removed and immersed in 4% PFA for 24 h at 4°C prior to paraffin embedding (ROTI® Plast, Germany). Sequential 4-μm sections of samples, corresponding to areas with Eu-VSOP accumulation identified by MRI, were cut, heated at 60°C for at least 1 h, and deparaffinized in m-xylene overnight (Sigma-Aldrich, Germany) for IMC. Following deparaffinization, the sections were re-hydrated in descending ethanol series (Carl Roth®, Germany). Then, samples were processed according to the IMC staining protocol for FFPE sections [PN 400322 A3, Fluidigm San Francisco, CA, United States(RSY1)]. The antigen retrieval was performed with a citrate buffer (10 mM sodium citrate, 0.05% Tween 20, pH 6) for 20 min at 96°C. After incubation with isotope-tagged antibodies overnight at 4°C, the sections were stained with the CELL-ID Intercalator-Ir (Fluidigm, United States) for 30 min at room temperature, then washed, air-dried and kept at RT until imaging with the Hyperion Imaging System (Fluidigm, United States).

[1]https://github.com/ChariteExpMri/antx2
[2]http://elastix.isi.uu.nl/
[3]https://imagej.nih.gov/ij/

All antibodies were tagged with a metal isotope using the Maxpar labeling kit according to the manufacturer's instructions (Fluidigm, United States). A complete list of the panel with a description of the antibodies, isotope tags, and dilutions is available in **Supplementary Table 1**. Imaging mass cytometry was performed on a CyTOF2/upgraded to Helios specifications coupled to a Hyperion Tissue Imager (Fluidigm), using CyTOF software version 7.0. Prior to ablation, the instrument was tuned according to the manufacturer's instructions, using the 3-Element Full Coverage Tuning Slide (Fluidigm). The dried slide was loaded into the imaging module and regions of interest were selected for each sample on a preview (panorama). Optimal laser power was determined for each sample to ensure complete ablation of the tissue. Laser ablation was performed at a resolution of 1 μm and a frequency of 200 Hz. Data was stored as MCD files as well as txt files. Original files were opened with MCD viewer (v1.0.560.6), and images were extracted as TIFF files. For visualization, threshold correction was applied to reduce noise followed by post-acquisition processing with ImageJ software (ImageJ 1.48v, United States) using the despeckle and sharpen tools and Gaussian blur filter (kernel width, 0.50 pixels).

RESULTS

GBCA and Eu-VSOP Incidence Maps in Adoptive Transfer EAE

Following transfer of myelin-reactive lymphocytes, all animals showed signs of disease reflecting ascending paralysis. On the first day of imaging after EAE establishment, the mean score was 1.97 (±0.76 SD) versus 2.83 (±0.39 SD) on the second day, 24 h after Eu-VSOP injection. According to the animal protocols, 8 animals with atypical signs of EAE or with a score greater than 3 were removed from the study before the second T2*-weighted acquisition.

Incidence maps, as percentage of mice affected, were created to visualize the extent and frequency of inflammatory lesions visualized by each of the two contrast agents. The color scale represents the percentage of animals with a mask in these areas (**Figure 3**). After establishment of the disease, all mice showed Gd- (n = 19) and Eu-VSOPs-enhancement (n = 11) (bregma coordinates −2.8 to 0.23 mm). Both GBCA and Eu-VSOPs were found throughout the brain. The GBCA-intensity maps, showing large diffuse Gd-enhanced lesions across the brain, indicate that BBB leakage was localized in the same areas among mice, namely near the ventricles. The most affected regions were close to large arteries, such as the left hippocampal artery (bregma coordinate −3.26 mm), present in 80% of the mice (**Figure 3A**). While the cerebellum and brainstem were particularly affected, enhancement was also found in the hippocampus, thalamus, hypothalamus and midbrain. Specifically within the brain area covered by the MRE scan (bregma coordinates −2.84 to 0.23 mm), GBCA-enhancement was detected within the cerebral cortex, cerebral nuclei, brain stem, midbrain and fiber tracts), as shown in details in the **Supplementary Figure 2**. Conversely, Eu-VSOP accumulation was more diffuse with a less predictable pattern, with the highest incidence in the vicinity of the basilar artery (bregma coordinate −3.26 mm) and the anterior cerebral artery (bregma coordinate −6.76 mm) of about 40% (**Figure 3B**). An overview of the Eu-VSOP distribution across the brain can be found in **Supplementary Figure 3**. Within the brain section covered by MRE, the signal distribution was found spread inside the hippocampus, cerebral nuclei, brain stem, midbrain and fiber tracts. **Table 1** additionally shows the incidence of Gd and Eu-VSOP across the whole brain.

Next, we assessed the global effect of neuroinflammation on viscoelasticity. Therefore, viscoelastic properties of the whole brain, disregarding the ventricles, were measured at baseline and after establishment of EAE symptoms. A significant softening (reduction in stiffness, i.e., decrease in c in m/s) was observed ($p < 0.0001$, baseline 3.15 ± 0.11 m/s vs. EAE 2.89 ± 0.20 m/s, n = 19), whereas the fluidity depicted by the loss angle (ϕ in rad) (p = 0.6070, baseline 0.69 ± 0.03 m/s vs. EAE 0.70 ± 0.06 m/s, n = 19) was unaffected (**Figure 4**).

MRE Detects Tissue Softening in Areas of Gd-Enhancement

To assess the sensitivity of MRE to measure mechanical alterations in areas of BBB leakage detected exclusively by Gd-enhancement, GBCA masks generated from percentage change images calculated from T1-weighted MR images were overlaid on MRE parameter maps (ϕ and c) as illustrated in **Figures 5A,B**.

A significant reduction in shear wave speed (c) after EAE establishment was observed compared to baseline (p = 0.0183; baseline 3.28 ± 0.38 m/s vs. EAE 2.99 ± 0.51 m/s, n = 19), indicating softening of brain tissue, whereas fluidity (phase angle, ϕ) remained unaltered (p = 0.3683; baseline 0.85 ± 0.08 rad vs. EAE 0.86 ± 0.09 rad, n = 19) (**Figure 5C**).

MRE Detects Marked Tissue Softening in Sites of Eu-VSOP Accumulation

Eight of the 11 mice with Eu-VSOP accumulation showed accumulation in regions covered by the MRE scans (bregma −2.84 to 0.23 mm). The masks solely comprising Eu-VSOP accumulation were overlaid on the MRE parameter maps, c and ϕ, as shown in **Figures 6A,B**. Tomoelastography at baseline and after EAE induction revealed a significant reduction in stiffness (c in m/s) in sites with Eu-VSOP accumulation (within hippocampus, cerebral nuclei, brain stem, midbrain and fiber tracts) (p = 0.0235, baseline 3.03 ± 0.39 m/s vs. EAE 2.55 ± 0.47 m/s, n = 8); whereas fluidity, depicted by ϕ in rad, was unaffected (p = 0.1168, baseline 0.91 ± 0.17 rad vs. EAE 0.87 ± 0.20 rad, n = 8) (**Figure 6C**).

Sites of Eu-VSOP Accumulation Display Pronounced Softening Compared to the Overall Brain Alterations

We further investigated whether MRE is sensitive to mechanical changes at sites of inflammation detected by MRI with either GBCA or Eu-VSOPs. For that, the percentage change in stiffness and fluidity in areas with Gd-enhancement or Eu- VSOP accumulation was compared to the rest of the brain (**Figure 7A**). Our analysis revealed no significant difference in the percentage

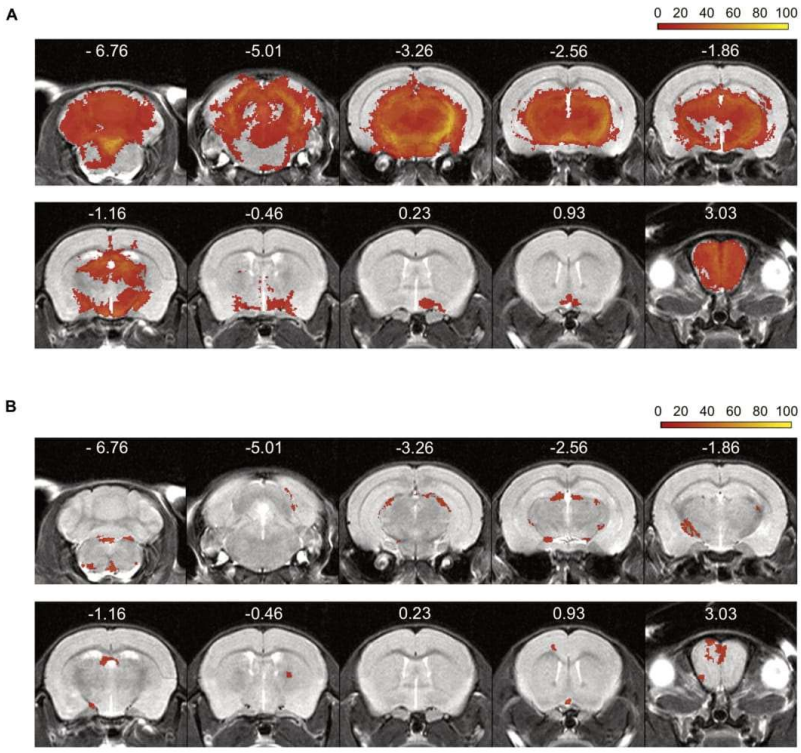

FIGURE 3 | Percentage incidence maps for Gd-enhancement and Eu-VSOP accumulation during EAE. **(A)** Incidence (% of mice affected) of gadolinium distribution across the brain, displaying large diffuse lesions along the cerebral cortex, cerebral nuclei, brain stem, midbrain and fiber tracts (n = 19). **(B)** Conversely, Eu-VSOP distribution appears to be characterized by smaller and focal areas of accumulation in the cerebral cortex, cerebral nuclei, brain stem, midbrain and fiber tracts (n = 11).

change between sites with Gd-enhancement (within cerebral cortex, cerebral nuclei, brain stem, midbrain and fiber tracts) compared to non-enhancing areas for either stiffness (p = 0.3321, Gd-enhanced areas −9.76 ± 13.32% vs. non-enhanced areas −7.18 ± 6.21%, n = 19) or fluidity (p = 0.1246, Gd-enhanced areas 4.47 ± 7.96% vs. rest of the brain 1.07 ± 10.56%, n = 19) (**Figure 7B**). However, when we compared the percentage change in stiffness between areas with Eu-VSOP accumulation and those without Eu-VSOP accumulation, we observed a significant difference (p = 0.0483, areas with Eu-VSOP accumulation −16.81 ± 16.49% vs. areas without accumulation −5.85 ± 3.81%, n = 8) (**Figure 7B**). This effect was also seen for global stiffness after establishment of EAE signs vs. stiffness at sites of Eu-VSOP accumulation (p = 0.0229, whole brain 2.93 ± 0.16 m/s vs. Eu-VSOP accumulation 2.55 ± 0.47 m/s, n = 8) (**Supplementary Figure 4**). This result indicates that, besides being sensitive to global brain changes, MRE can effectively identify areas affected by inflammatory processes that are detectable by Eu-VSOP accumulation only. Fluidity in these above mentioned locations, however, was unaffected (p = 0.2889, areas with Eu-VSOP accumulation −5.29 ± 8.33% vs. non-hypointense areas −2.16 ± 6.63%, n = 8) (**Figure 7B**).

TABLE 1 | Incidence of Gd-enhancement and Eu-VSOP accumulation.

	Incidence (%)	
Anatomical label	**Gd mask**	**Eu-VSOP mask**
Cerebral cortex	100	72.7
Cerebral nuclei	100	54.5
Brain stem	78.9	90.9
Midbrain	100	63.6
Hindbrain	100	63.6
Cerebellum	100	54.5
Fiber tracts	100	90.9

Incidence in percent of Gd-enhancement and Eu-VSOP accumulation, per brain region, across the whole brain.

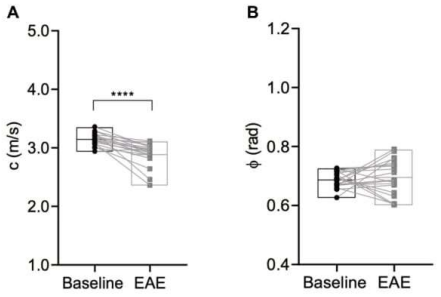

FIGURE 4 | Global brain softening due to inflammation. **(A)** Whole brain stiffness is reduced during inflammation ($p < 0.0001$, Wilcoxon matched-pairs signed rank test), whereas **(B)** fluidity is unaffected ($p = 0.6070$, paired *t*-test). $n = 19$; mean, min/max. ****$p \leq 0.0001$.

Visualization of Eu-VSOPs by IMC Reveals Association of Eu-VSOP Accumulation With Inflammatory Damage

To confirm that the histopathological changes are indeed associated with inflammation-induced Eu-VSOP accumulation, we investigated inflammation in EAE and healthy control brain sections as well as the tissue distribution of Eu-VSOP and co-localization with different inflammatory and barrier cells using IMC (**Figures 8**, **9**).

When compared with healthy control, EAE mice showed evident inflammation, with gliosis, represented by increase in Iba^{+}(white) cells and GFAP (green), as well as infiltration of immune cells (CD45, cyan) (**Figure 8**, white arrows). In sites where Eu-VSOPs were visualized by MRI, the particles were found to be associated with sites of inflammatory damage. In particular, areas of Eu-VSOP accumulation presented CD45 + leukocyte infiltration, mostly concentrated in perivascular cuffs, in the periventricular space (**Figure 9A**, arrowheads) as well as in the choroid plexus (**Figure 9B**, white arrows). Iba-1 + cells (microglia, macrophages) were frequently localized alongside immune infiltrates. Perivascularly, Eu-VSOP accumulation was confined to these sites of injury and colocalized with Iba-1 + and CD45 + positive cells. Furthermore, Eu-VSOPs (red dots) were found to be especially associated to the vessel walls, where they were co-localized with activated endothelial cells (CD31+). In the ventricles, Eu-VSOPs (red dots) were confined to the choroid plexus, showing a clear association with the presence of immune infiltrates (**Figure 9B**). No particles were found to be co-localized with NeuN + neurons. Due to the IMC resolution of 1 μm and the particle dynamic diameter of 7 nm, quantification of the particle count could not be determined.

DISCUSSION

MRE has been previously shown to identify global changes in brain stiffness both in MS and in its animal model, EAE (Wuerfel et al., 2010; Streitberger et al., 2012; Riek et al., 2012; Millward et al., 2015; Wang et al., 2020). To further understand the

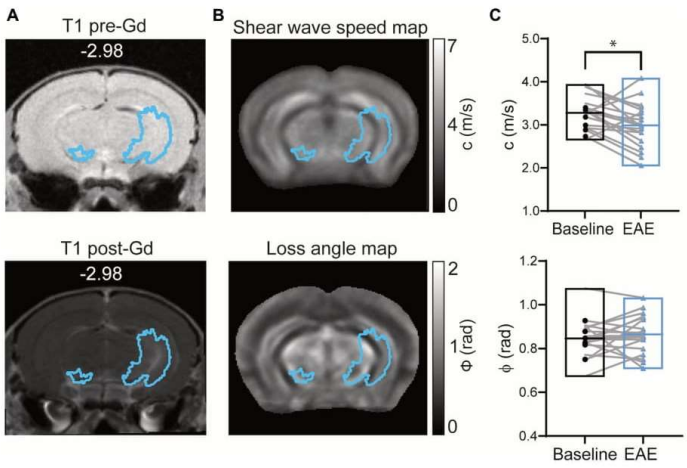

FIGURE 5 | Brain mechanical properties in Gd-enhanced lesions during EAE. **(A)** Representative T1-weighted image acquired before (left) and after GBCA (right) injection (corresponding GBCA mask overlaid) shows Gd-enhancing lesions near the left hippocampal artery. **(B)** GBCA mask overlaid on averaged MRE maps of stiffness (shear wave speed) and fluidity (loss angle). **(C)** Stiffness represented by shear wave speed (c) was reduced during EAE ($p = 0.0183$; paired *t*-test) whereas tissue fluidity (ϕ) was unchanged ($p = 0.3683$; paired *t* test). $n = 19$; mean, min/max; ∗<0.05. Of note, ventricles are excluded from our analysis since MRE cannot be performed in fluid compartments.

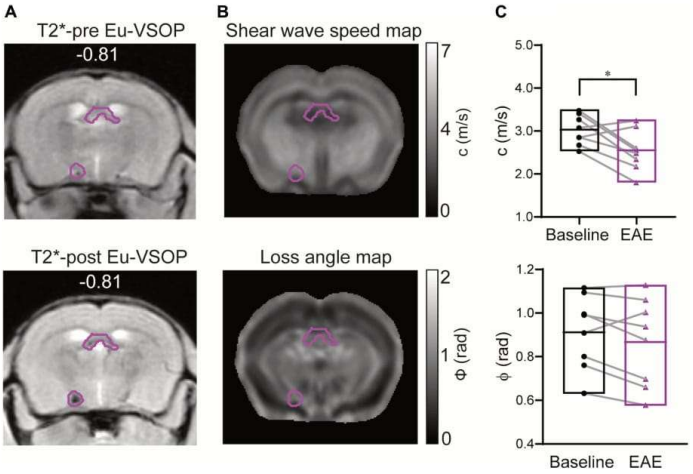

FIGURE 6 | Brain mechanical properties of areas accumulating Eu-VSOPs during EAE. **(A)** Exemplary image of a mask comprising Eu-VSOP accumulation overlaid on T2*-weighted image prior (left) and post Eu-VSOP (right) injection. **(B)** Shear wave speed map (c in m/s) and loss angle map (ϕ in rad). **(C)** There is a significant reduction in stiffness in sites with Eu-VSOP accumulation compared to non-hypointense areas ($p = 0.0235$, paired t-test). Fluidity of brain tissue in these areas, marked by ϕ, is not affected ($p = 0.1168$, paired t-test). $n = 8$, mean, min/max; *<0.05. Of note, ventricles are excluded from our analysis since MRE cannot be performed in fluid compartments.

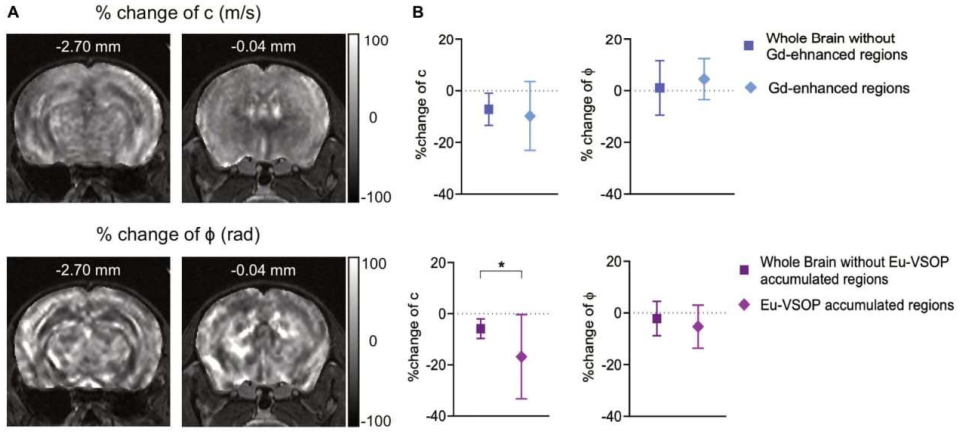

FIGURE 7 | MRE is sensitive to stiffness changes in sites of Eu-VSOP accumulation. **(A)** Representative percentage change maps of c- and ϕ-map. **(B)** Percentage change in areas with Gd enhancement (within cerebral cortex, cerebral nuclei, brain stem, midbrain and fiber tracts) compared to non-enhancing areas revealed no significant difference (top), for c in m/s $p = 0.3321$ (Wilcoxon matched-pairs rank sum test), for ϕ in rad $p = 0.1246$ (paired t-test), $n = 19$; percentage change of region with Eu-VSOP accumulation (within cerebral cortex, cerebral nuclei, brain stem, midbrain and fiber tracts) (bottom) compared to non-hypointense areas showed a significant difference for c ($p = 0.0483$, paired t-test, mean ± SD, $n = 8$, *<0.05) whereas ϕ was not affected ($p = 0.2889$, paired t-test, mean ± SD $n = 8$, *<0.05). Percentage change maps are based on the percentage difference from peak to baseline.

neuropathological alterations detected by MRE, we combined MRE with GBCA- and Eu-VSOP-enhanced MRI. Tissue viscoelasticity was then evaluated in areas of BBB leakage (GBCA-enhancing areas) and in sites with Eu-VSOP accumulation, i.e., areas where we have previously identified activated myeloid cells and/or altered endothelium or epithelia. To the best of our knowledge, this study for the first time combines analysis of these biochemical imaging markers with MRE findings

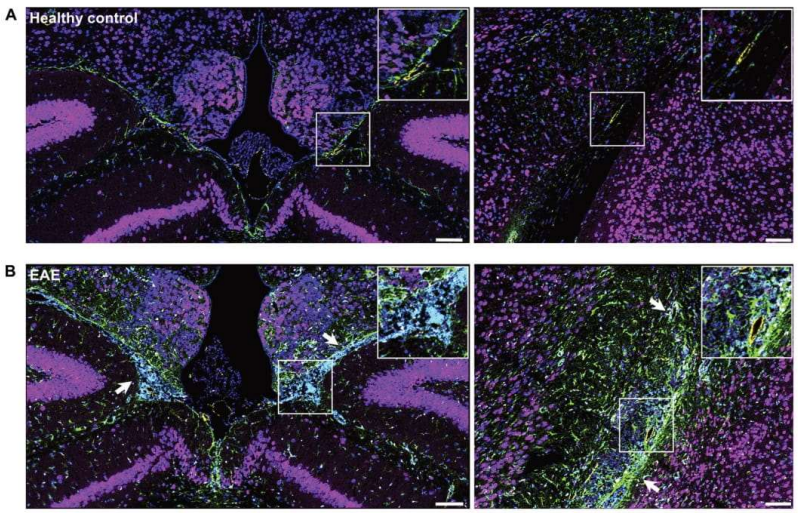

FIGURE 8 | Visualization of brain inflammation induced by EAE using IMC. **(A)** Brain section of a healthy control (naïve) mouse at the third ventricles (left) and brain stem and hippocampal formation (right). **(B)** Extensive inflammation during EAE can be visualized by infiltration of $CD45^+$ cells (cyan), astrogliosis (GFAP, green) and activated microglia (Iba-1, white) (white arrows). Neurons (NeuN—magenta), astrocytes (GFAP—green), endothelial cells (CD31—yellow), nuclei (histone H3—blue), microglia (Iba-1—white), leucocytes (CD45—cyan). Scale bar: 100 μm.

across multiple slices in a mouse model of neuroinflammation, revealing that areas of exclusive GBCA or Eu-VSOP signal displayed significant tissue softening. When these areas were compared with non-enhancing brain areas, stiffness changes at sites of Eu-VSOP accumulation showed more pronounced softening than areas of Gd-enhancement, suggesting that MRE is especially sensitive to detect inflammation-associated changes in tissue viscoelasticity. Subsequent histological visualization of Eu-VSOPs by IMC confirmed their distribution in areas of intense focal inflammation, likely undergoing significant tissue remodeling.

Here, brain viscoelastic properties were investigated in the adoptive transfer EAE model using SJL mice. The induction of this model, introduced by injection of a pre-activated population of myelin epitope-specific CD4 + T cells, results in a more severe disease with large cerebral infiltrations compared to active immunization, as used in previous studies (Riek et al., 2012; Wang et al., 2020). While in C57BL/6 mice, immunized with myelin oligodendrocyte glycoprotein (MOG) (Miller and Karpus, 2007), principally spinal cord lesions are detected, making this model less suitable for cranial MRE studies (Millward et al., 2015). Thus, the relapse-remitting adoptive transfer model in SJL mice is an appropriate tool for brain imaging studies.

In this study we confirm previous work reporting a significant global decrease in stiffness during neuroinflammation in both patients and mouse models of neuropathologies such as Alzheimer (Murphy et al., 2011; Munder et al., 2018), Parkinson disease (Lipp et al., 2013; Klein et al., 2014; Hain et al., 2016), and MS (Wuerfel et al., 2010; Streitberger et al., 2012) (Riek et al., 2012; Millward et al., 2015; Fehlner et al., 2016; Wang et al., 2020). Based on gene expression and histopathological investigations, this reduction in stiffness correlated with the severity of inflammation. In the EAE model, an increased expression of CD3, a T-cell lineage marker (Riek et al., 2012), and F4/80 gene expression, a marker for macrophages (Millward et al., 2015), positively correlated with brain softening. Furthermore, enhanced expression of the extracellular matrix glycoprotein fibronectin was correlated with decreased stiffness, hinting at a role of neurovascular remodeling at lesion sites that contributes to changes in mechanical tissue properties (Wang et al., 2020). However, previously MRE changes were only investigated in large brain areas within one slice and thus could not account for regionally resolved inflammation. By combining contrast-enhanced MRI and multifrequency MRE with tomoelastography post processing, we were able to directly measure changes in viscoelastic properties at sites of neuroinflammation. Although, MRE was limited to the same brain segment included in previous studies using tomoelastography (Bertalan et al., 2019; Bertalan et al., 2020; Guo et al., 2019), known for acquiring multifrequency wavefield for high-resolution MRE, we were able to acquire multiple slices ranging from bregma −2.84 to 0.23 and with a resolution sufficient to resolve areas of focal inflammation. This allowed us to register MRE maps to a reference atlas, thus making the comparison within areas of contrast agent enhancement possible.

GBCA-enhanced MRI visualizes BBB permeability not only in MS patients but also in EAE models (Hawkins et al., 1990; Nessler et al., 2007; Schellenberg et al., 2007; Smorodchenko et al., 2007;

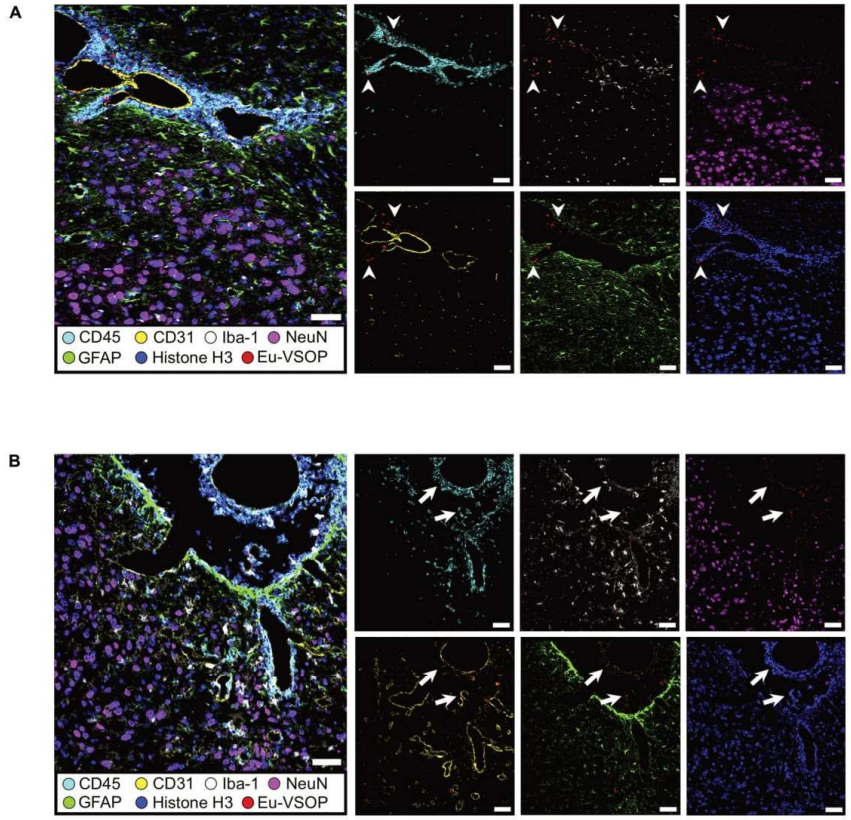

FIGURE 9 | Histological visualization of Eu-VSOP distribution by IMC. **(A)** Magnetic particle accumulation in the perivascular space with strong leukocyte infiltrate (arrowheads) located between brain stem and hippocampal formation. **(B)** In the third ventricle, particles can be found in the choroid plexus and are associated with perivascular inflammation (arrows). Eu-VSOPs (red dots), neurons (NeuN—magenta), astrocytes (GFAP—green), endothelial cells (CD31—yellow), nuclei (histone H3—blue), microglia (Iba-1—white), leucocytes (CD45—cyan). Scale bar: 50 mm.

Tysiak et al., 2009; Wuerfel et al., 2007; Waiczies et al., 2012). To investigate the potential of MRE in identifying BBB-related pathological events, we directly compared mechanical properties of the brain and Gd distribution. Here, the quantification of viscoelastic parameters revealed a significant decrease in tissue stiffness in adoptive transfer EAE.

As apparent from the incidence maps, all mice had GBCA enhancement, as also shown by Smorodchenko et al., 2007. Confirming previous results (Smorodchenko et al., 2007; Wuerfel et al., 2007), our findings showed marked involvement of the brain, with extensive cerebellar enhancement (bregma −7.32 and −5.50 mm), notably at the 4th ventricle; similarly, but to a lesser extent, the brain stem was also affected. Cerebellar susceptibility to BBB breakdown is an expected outcome of this model and is attributable to the high degree of vascularization in this area (Tonra, 2002). Other regions showing Gd-enhancement included the periventricular areas, hippocampus, thalamus, hypothalamus and midbrain (bregma −3.26 to −1.86), with particularly pronounced enhancement close to major vessels such as the hippocampal artery and in their adjacency. This pattern of enhancement has been described in other EAE models before (Kuharik et al., 1988; Smorodchenko et al., 2007; Wuerfel et al., 2007).

However, Gd-enhancing areas showed a reduction in stiffness similar to that observed in non-enhancing areas of the inflamed brain. Given that Gd-enhancement is often visualized as areas of diffuse hyperintensity and much more extensive compared with the pattern of Eu-VSOP accumulation, we hypothesize that the viscoelastic effect observed in areas of Gd-enhancement does not reflect strictly localized histopathological alterations purely associated with BBB breakdown, but rather indicates predominantly a disseminated softening due to the inflammatory

state of the brain. Although GBCA diffusion within the tissue primarily represents increased BBB permeability and has been correlated with glial cell activation (Nessler et al., 2007; Morrissey et al., 1996), its spatial distribution is not only limited to these events. After crossing the BBB, GBCA diffusion and dispersion throughout the tissue could also be attributed to factors such as the contrast agent's distribution in the interstitial and intracellular spaces, an inherent property of a molecule's biodistribution (Aime and Caravan, 2009), the degree of vascular disruption and leakiness (Layne et al., 2018), or the reduction of perfusion or extracellular space in areas of inflammatory lesions (Nessler et al., 2007).

Previous studies have shown that Gd-enhancing lesions are present before disease signs become apparent (Wuerfel et al., 2007) but rarely correlate with the presence of characteristic immune infiltrate-derived lesions, a hallmark of EAE and MS (Nessler et al., 2007; Nathoo et al., 2014). In contrast, we show that Eu-VSOPs also accumulate in areas that are not enhanced by GBCA and are present at sites of immune cell infiltration, which is in alignment with the literature (Tysiak et al., 2009; Millward et al., 2019; Berndt et al., 2017). More precisely, we found Eu-VSOPs to be dispersed and mostly located in the vicinity of vessels and ventricles, as indicated in the incidence maps. In the cerebellum, comprising approximately the bregma coordinates −7.32 to −5.50 mm, Eu-VSOP accumulations were found next to the 4th ventricle, the dorsomedial cerebellar arteries, lateral superior cerebral artery, and close to the basilar artery. In the bregma −3.26 mm to 0.23 mm, including structures such as the hippocampus, and the lateral and 3rd ventricles, Eu-VSOPs appear to be located close to the anterior choroidal artery (for anatomical references refer to Dorr et al. (2007) and Xiong et al. (2017). Different routes have been proposed to explain how VSOPs can enter the brain: phagocytosis by peripheral macrophages (Tysiak et al., 2009; Millward et al., 2019) and activated T cells (Wuerfel et al., 2007), which then infiltrate the CNS; passive diffusion through the leaky BBB as freely diffusing particles as observed in the parenchyma of EAE mice (Millward et al., 2013); and binding to endothelial or epithelial barriers (Plewes et al., 1995; Streitberger et al., 2012). Eu-VSOPs were imaged 24 h after injection when they have been shown to be cleared from the blood (Wuerfel et al., 2007). Therefore, we propose that hypointense signals seen in T2* images originate primarily from VSOP bound to altered ECM components (Berndt et al., 2017) or from particles phagocytosed by peripheral macrophages or/and activated microglia present at sites of inflammation (Tysiak et al., 2009; Millward et al., 2013, 2019). However, it cannot be excluded that these hypointense signals originate from particles phagocytosed by intravascular immune cells patrolling the endothelium and ready to cross upon inflammatory signals as reported in Masthoff et al., 2018 (Masthoff et al., 2018). Taken together, these evidence indicate that magnetic particles reveal histopathological alterations other than the well-known BBB disruption underlying GBCA enhancement (Tysiak et al., 2009; Millward et al., 2013; Berndt et al., 2017).

Importantly, our results show that, during inflammation, stiffness is particularly reduced in regions of Eu-VSOP accumulation compared to global brain softening. To elucidate underlying alterations in sites with Eu-VSOP accumulation that might contribute to the marked reduction in stiffness, we performed histological assessment of the particles. Differently from the unspecific method to detect iron particles, the Prussian blue stain, here we show that Eu-VSOPs can be visualized by IMC. The IMC allows a distinguishable detection of the Eu present in the core of the particles, and additionally, provides important information on the cellular environment in sites of particle accumulation. We found that Eu-VSOPs accumulated at sites of inflammation, as co-localization with leukocyte infiltrate was evident, in line with our previous reports (Millward et al., 2013). In areas without hypointense signal, particles may be found scattered in the tissue, possibly after diffusing through the disrupted BBB and accumulating in the brain parenchyma. Consequently, passively diffused particles would not contribute to the MRI signal 24 h after injection as much as the phagocytosed particles accumulated in sites of strong inflammation.

In contrast to tissue from EAE mice, histological analysis of healthy control further confirmed no Eu-VSOP accumulation in the non-inflamed brain tissue, indicating that Eu-VSOP accumulation is caused by processes of inflammation. Accumulations within the investigated inflamed tissue sections were mostly concentrated in the perivascular cuffs and in the periventricular space as well as in the choroid plexus. In areas of inflammatory alterations, we found particles co-localized with endothelial cells, which could have been uptaken *via* inflammation-induced alterations of sulfated glycosaminoglycans on the endothelial glycocalyx (Berndt et al., 2017) and with CD45 + and Iba-1 + cells, suggesting that they were phagocytosed. During EAE, astrogliosis and pronounced microglial activation were observed, presenting a typically hypertrophic and ramified morphology. Eu-VSOPs were also specifically co-localized with activated microglia, consistent with previous reports (Wuerfel et al., 2007; Tysiak et al., 2009; Millward et al., 2013, 2019). Atomic force microscopy has shown that glial cells are relatively softer than their neighboring neurons (Lu et al., 2006), as GFAP-expressing cells were associated with lower stiffness values (Moeendarbary et al., 2017). Therefore, in inflamed regions, the presence of softer glial cells could be one contributing factor to the marked decrease in stiffness observed in sites of Eu-VSOP accumulation. Additionally, the inflammatory activity of infiltrating peripheral immune cells and activated glial cells in these areas could result in extensive remodeling of the ECM. In addition, secretion of metalloproteinases during neuroinflammation leads to the degradation of ECM components, which facilitates further disruption of the BBB [for a review refer to Rosenberg (2002)]. A dynamic alteration of the ECM structure with accumulation of other matrix components, such as fibronectin, has also been demonstrated for EAE and correlates with neural tissue softening (Wang et al., 2020).

Moreover, although there are no studies directly associating vasogenic edema with viscoelastic changes in EAE, reports on mice with stroke lesions have linked edema with brain softening in the ipsilateral side (Xu et al., 2013, 2014). Thus, it is possible

that vasogenic edema associated with the cellular inflammation depicted may also influence tissue elasticity in areas with VSOPs.

The pronounced softening observed at sites of Eu-VSOP accumulation suggests that an intense focal inflammatory process has a strong effect on viscoelastic parameters. This could be attributable to a combined influence of activated glial cells, accumulation of immune cells, local edema, and/or remodeling of the extracellular matrix, especially in the microenvironment of the neurovascular unit. On the other hand, GBCA-enhanced MRI reflects a transient event of enhanced vessel permeability and may only account for one aspect of the inflammatory state in a multifactorial disease model. Hence, the contribution of the dynamic disturbance of the BBB possibly results in a different distribution of Eu-VSOP accumulation compared to Gd-enhancement.

To be able to distinguish neuroinflammatory processes visualized either by GBCA or by VSOPs, masks comprising solely each contrast agent were generated. Areas, in which Eu-VSOP accumulation overlaps with Gd-enhancement might contain particles that just passively diffuse into the brain parenchyma through a damaged BBB. Thus, particles co-localizing with GBCA-enhancement would not reveal distinct aspects of inflammation different from BBB leakage and were not considered for this investigation.

One limitation of our study is that the brain area covered by tomoelastography is limited to the bregma areas −2.84 mm to 0.23 mm. It is well documented, for instance, that the cerebellum is a particularly affected region in EAE models (Tonra, 2002; Wuerfel et al., 2007; Millward et al., 2015) though it could not be included in our analysis. Therefore, it would be important to include these regions in future studies to incorporate crucial pathological information into the imaging findings. Moreover, based on previous studies, we consider that 24 h after injection, Magnevist is completely depleted from the blood and the brain (Tysiak et al., 2009; Wang et al., 2020). Thus, an effect on the T2*-weighted image used for quantification of Eu-VSOP is highly unlikely. However, since we did not perform a T1 scan before the second T2*-weighted scan, it is not possible to completely exclude a residual effect of the GBCA.

A noteworthy point to mention is that studies involving *in vivo* VSOP imaging requires intravenous administration of particles with the obvious associated safety concerns if a clinical application in the future is intended. As changes in viscoelastic properties in areas of VSOP accumulation was shown to be detectable by MRE, we propose that MRE may represent a suitable non-invasive imaging method that allows *in vivo* visualization of broad pathological processes. MRE could therefore be applied to both, pre-clinical and clinical settings in the context of neuroinflammation, serving as a tool for research, diagnostic, and therapy monitoring.

CONCLUSION

Combining for the first time Gd-enhancement and Eu-VSOP with *in vivo* multifrequency MRE, we obtained results suggesting that MRE is able to detect non-invasively pathological processes associated with inflammation beyond BBB disruption and vascular leakage. Such processes visualized by Eu-VSOP-enhanced MRI may involve gliosis and macrophages infiltration as well as alterations of endothelial matrix components and ECM remodeling. MRE may serve to visualize *in vivo* a broad spectrum of pathological processes and represents, therefore, a useful non-invasive imaging tool for neuroinflammation in preclinical and clinical settings.

DATA AVAILABILITY STATEMENT

The raw data supporting the conclusions of this article will be made available by the authors, without undue reservation.

ETHICS STATEMENT

The animal study was reviewed and approved by Berlin State Office for Health and Social Affairs (LAGeSo), Berlin, Germany.

AUTHOR CONTRIBUTIONS

AM and RS: experimental design, data acquisition, data analysis and interpretation, and manuscript writing. YR-S and DK: IMC design, image acquisition, image processing, and manuscript revision. HT: supervision of MRE data analysis and manuscript revision. AK: IMC resources and manuscript revision. JS and MT: Eu-VSOP resources and manuscript revision. SK: technical assistance, supervision of MRI data registration, and manuscript revision. SM and PB-S: technical assistance, supervision of MRI design and data analysis, and manuscript revision. CI-D and IS: conceptualization, data interpretation, funding acquisition, resources, methodology, project administration, supervision, and editing and critical revision of manuscript. All authors fully qualify for authorship and have approved the final version of the manuscript.

FUNDING

This work was funded by the Deutsche Forschungsgemeinschaft (DFG, German Research Foundation)—project number 372486779—SFB 1340_ Projects A01, B05, B06, C01, and C03, the Einstein Center for Neurosciences Berlin (ECN) and the Research Training Group GRK2260 BIOQIC.

ACKNOWLEDGMENTS

We would like to thank Natascha Asselborn for technical assistance.

SUPPLEMENTARY MATERIAL

The Supplementary Material for this article can be found online at: https://www.frontiersin.org/articles/10.3389/fnins.2021.701308/full#supplementary-material

REFERENCES

Aime, S., and Caravan, P. (2009). Biodistribution of gadolinium-based contrast agents, including gadolinium deposition. *J. Magn. Reson. Imaging* 30, 1259–1267. doi: 10.1002/jmri.21969

Alvarez, J. I., Cayrol, R., and Prat, A. (2011). Disruption of central nervous system barriers in multiple sclerosis. *Biochim. Biophys. Acta* 1812, 252–264.

Berndt, D., Millward, J. M., Schnorr, J., Taupitz, M., Stangl, V., Paul, F., et al. (2017). Inflammation-induced brain endothelial activation leads to uptake of electrostatically stabilized iron oxide nanoparticles via sulfated glycosaminoglycans. *Nanomedicine* 13, 1411–1421. doi: 10.1016/j.nano.2017.01.010

Bertalan, G., Guo, J., Tzschätzsch, H., Klein, C., Barnhill, E., Sack, I., et al. (2019). Fast tomoelastography of the mouse brain by multifrequency single-shot MR elastography. *Magn. Reson. Med.* 81, 2676–2687. doi: 10.1002/mrm.27586

Bertalan, G., Klein, C., Schreyer, S., Steiner, B., Kreft, B., Tzschätzsch, H., et al. (2020). Biomechanical properties of the hypoxic and dying brain quantified by magnetic resonance elastography. *Acta Biomater.* 101, 395–402. doi: 10.1016/j.actbio.2019.11.011

de Schellenberger, A. A., Hauptmann, R., Millward, J. M., Schellenberger, E., Kobayashi, Y., Taupitz, M., et al. (2017). Synthesis of europium-doped VSOP, customized enhancer solution and improved microscopy fluorescence methodology for unambiguous histological detection. *J. Nanobiotechnol.* 15, 1–14.

Dorr, A., Sled, J. G., and Kabani, N. (2007). Three-dimensional cerebral vasculature of the CBA mouse brain: a magnetic resonance imaging and micro computed tomography study. *Neuroimage* 35, 1409–1423. doi: 10.1016/j.neuroimage.2006.12.040

Fehlner, A., Behrens, J. R., Streitberger, K. J., Papazoglou, S., Braun, J., Bellmann-Strobl, J., et al. (2016). Higher-resolution MR elastography reveals early mechanical signatures of neuroinflammation in patients with clinically isolated syndrome. *J. Magn. Reson. Imaging* 44, 51–58. doi: 10.1002/jmri.25129

Guo, J., Bertalan, G., Meierhofer, D., Klein, C., Schreyer, S., Steiner, B., et al. (2019). Brain maturation is associated with increasing tissue stiffness and decreasing tissue fluidity. *Acta Biomateri.* 99, 433–442. doi: 10.1016/j.actbio.2019.08.036

Hain, E. G., Klein, C., Munder, T., Braun, J., Riek, K., Mueller, S., et al. (2016). Dopaminergic neurodegeneration in the mouse is associated with decrease of viscoelasticity of substantia nigra tissue. *PLoS One* 11:e0161179. doi: 10.1371/journal.pone.0161179

Hawkins, C., Munro, P., MacKenzie, F., Kesselring, J., Tofts, P., Boulay, E. D., et al. (1990). Duration and selectivity of blood-brain barrier breakdown in chronic relapsing experimental allergic encephalomyelitis studied by gadolinium-DTPA and protein markers. *Brain* 113, 365–378. doi: 10.1093/brain/113.2.365

Hirsch, S., Braun, J., and Sack, I. (2017). *Magnetic resonance elastography: physical background and medical applications*. Hoboken, NJ: John Wiley & Sons.

Hiscox, L. V., Johnson, C. L., Barnhill, E., McGarry, M. D., Huston, J., van Beek, E. J., et al. (2016). Magnetic resonance elastography (MRE) of the human brain: technique, findings and clinical applications. *Phys. Med. Biol.* 61, R401–R437.

Klein, C., Hain, E. G., Braun, J., Riek, K., Mueller, S., Steiner, B., et al. (2014). Enhanced adult neurogenesis increases brain stiffness: *in vivo* magnetic resonance elastography in a mouse model of dopamine depletion. *PloS One* 9:e92582. doi: 10.1371/journal.pone.0092582

Klein, S., Staring, M., Murphy, K., Viergever, M. A., and Pluim, J. P. (2009). Elastix: a toolbox for intensity-based medical image registration. *IEEE Trans. Med. Imaging* 29, 196–205. doi: 10.1109/tmi.2009.2035616

Koch, S., Mueller, S., Foddis, M., Bienert, T., von Elverfeldt, D., Knab, F., et al. (2019). Atlas registration for edema-corrected MRI lesion volume in mouse stroke models. *J. Cerebral. Blood Flow Metabol.* 39, 313–323. doi: 10.1177/0271678x17726635

Kuharik, M., Edwards, M., Farlow, M., Becker, G., Azzarelli, B., Klatte, E., et al. (1988). Gd-enhanced MR imaging of acute and chronic experimental demyelinating lesions. *Am. J. Neuroradiol.* 9, 643–648.

Lassmann, H. (2008). The pathologic substrate of magnetic resonance alterations in multiple sclerosis. *Neuroimaging Clin. North Am.* 18, 563–576. doi: 10.1016/j.nic.2008.06.005

Layne, K. A., Dargan, P. I., Archer, J. R., and Wood, D. M. (2018). Gadolinium deposition and the potential for toxicological sequelae–A literature review of issues surrounding gadolinium-based contrast agents. *Br. J. Clin. Pharmacol.* 84, 2522–2534. doi: 10.1111/bcp.13718

Lipp, A., Trbojevic, R., Paul, F., Fehlner, A., Hirsch, S., Scheel, M., et al. (2013). Cerebral magnetic resonance elastography in supranuclear palsy and idiopathic Parkinson's disease. *NeuroImage Clin.* 3, 381–387. doi: 10.1016/j.nicl.2013.09.006

Lu, Y.-B., Franze, K., Seifert, G., Steinhäuser, C., Kirchhoff, F., Wolburg, H., et al. (2006). Viscoelastic properties of individual glial cells and neurons in the CNS. *Proc. Natl. Acad. Sci.* 103, 17759–17764. doi: 10.1073/pnas.0606150103

Manduca, A., Bayly, P. J., Ehman, R. L., Kolipaka, A., Royston, T. J., Sack, I., et al. (2021). MR elastography: Principles, guidelines, and terminology. *Magn. Reson. Med.* 85, 2377–2390. doi: 10.1002/mrm.28627

Masthoff, M., Gran, S., Zhang, X., Wachsmuth, L., Bietenbeck, M., Helfen, A., et al. (2018). Temporal window for detection of inflammatory disease using dynamic cell tracking with time-lapse MRI. *Sci. Rep.* 8:9563.

Miller, S. D., and Karpus, W. J. (2007). Experimental autoimmune encephalomyelitis in the mouse. *Curr. Protoc. Immunol.* 15:15.1.

Millward, J. M., de Schellenberger, A. A., Berndt, D., Hanke-Vela, L., Schellenberger, E., Waiczies, S., et al. (2019). Application of europium-doped very small iron oxide nanoparticles to visualize neuroinflammation with MRI and fluorescence microscopy. *Neuroscience* 403, 136–144. doi: 10.1016/j.neuroscience.2017.12.014

Millward, J. M., Guo, J., Berndt, D., Braun, J., Sack, I., and Infante-Duarte, C. (2015). Tissue structure and inflammatory processes shape viscoelastic properties of the mouse brain. *NMR Biomed.* 28, 831–839. doi: 10.1002/nbm.3319

Millward, J. M., Schnorr, J., Taupitz, M., Wagner, S., Wuerfel, J. T., and Infante-Duarte, C. (2013). Iron oxide magnetic nanoparticles highlight early involvement of the choroid plexus in central nervous system inflammation. *ASN Neuro* 5:e00110.

Moeendarbary, E., Weber, I. P., Sheridan, G. K., Koser, D. E., Soleman, S., Haenzi, B., et al. (2017). The soft mechanical signature of glial scars in the central nervous system. *Nat. Commun.* 8, 1–11.

Morrissey, S. P., Stodal, H., Zettl, U., Simonis, C., Jung, S., Kiefer, R., et al. (1996). *In vivo* MRI and its histological correlates in acute adoptive transfer experimental allergic encephalomyelitis: quantification of inflammation and oedema. *Brain* 119, 239–248. doi: 10.1093/brain/119.1.239

Munder, T., Pfeffer, A., Schreyer, S., Guo, J., Braun, J., Sack, I., et al. (2018). MR elastography detection of early viscoelastic response of the murine hippocampus to amyloid β accumulation and neuronal cell loss due to Alzheimer's disease. *J. Magn. Reson. Imaging* 47, 105–114. doi: 10.1002/jmri.25741

Murphy, M. C., Huston, J. III, Jack, C. R. Jr., Glaser, K. J., Manduca, A., Felmlee, J. P., et al. (2011). Decreased brain stiffness in Alzheimer's disease determined by magnetic resonance elastography. *J. Magn. Reson. Imag.* 34, 494–498. doi: 10.1002/jmri.22707

Muthupillai, R., Lomas, D., Rossman, P., Greenleaf, J. F., Manduca, A., and Ehman, R. L. (1995). Magnetic resonance elastography by direct visualization of propagating acoustic strain waves. *Science* 269, 1854–1857. doi: 10.1126/science.7569924

Nathoo, N., Yong, V. W., and Dunn, J. F. (2014). Understanding disease processes in multiple sclerosis through magnetic resonance imaging studies in animal models. *NeuroImage Clin.* 4, 743–756. doi: 10.1016/j.nicl.2014.04.011

Nessler, S., Boretius, S., Stadelmann, C., Bittner, A., Merkler, D., Hartung, H.-P., et al. (2007). Early MRI changes in a mouse model of multiple sclerosis are predictive of severe inflammatory tissue damage. *Brain* 130, 2186–2198. doi: 10.1093/brain/awm105

Plewes, D., Betty, I., Urchuk, S., and Soutar, I. (1995). Visualizing tissue compliance with MR imaging. *J. Magn. Reson. Imaging* 5, 733–738. doi: 10.1002/jmri.1880050620

Riek, K., Millward, J. M., Hamann, I., Mueller, S., Pfueller, C. F., Paul, F., et al. (2012). Magnetic resonance elastography reveals altered brain viscoelasticity in experimental autoimmune encephalomyelitis. *Neuroimage Clin.* 1, 81–90. doi: 10.1016/j.nicl.2012.09.003

Rosenberg, G. A. (2002). Matrix metalloproteinases in neuroinflammation. *Glia* 39, 279–291. doi: 10.1002/glia.10108

Schellenberg, A. E., Buist, R., Yong, V. W., Del Bigio, M. R., and Peeling, J. (2007). Magnetic resonance imaging of blood–spinal cord barrier disruption

in mice with experimental autoimmune encephalomyelitis. *Magn. Reson. Med.* 58, 298–305. doi: 10.1002/mrm.21289

Schregel, K., Wuerfel, E., Garteiser, P., Gemeinhardt, I., Prozorovski, T., Aktas, O., et al. (2012). Demyelination reduces brain parenchymal stiffness quantified *in vivo* by magnetic resonance elastography. *Proc. Natl. Acad. Sci. U S A.* 109, 6650–6655. doi: 10.1073/pnas.1200151109

Smorodchenko, A., Wuerfel, J., Pohl, E. E., Vogt, J., Tysiak, E., Glumm, R., et al. (2007). CNS-irrelevant T-cells enter the brain, cause blood–brain barrier disruption but no glial pathology. *Eur. J. Neurosci.* 26, 1387–1398. doi: 10.1111/j.1460-9568.2007.05792.x

Streitberger, K.-J., Sack, I., Krefting, D., Pfüller, C., Braun, J., Paul, F., et al. (2012). Brain viscoelasticity alteration in chronic-progressive multiple sclerosis. *PloS One* 7:e29888. doi: 10.1371/journal.pone.0029888

Taupitz, M., Schnorr, J., Abramjuk, C., Wagner, S., Pilgrimm, H., Hünigen, H., et al. (2000). New generation of monomer-stabilized very small superparamagnetic iron oxide particles (VSOP) as contrast medium for MR angiography: Preclinical results in rats and rabbits. *J. Magn. Reson. Imaging* 12, 905–911. doi: 10.1002/1522-2586(200012)12:6<905::aid-jmri14>3.0.co;2-5

Thompson, A., Baranzini, S., Geurts, J., Hemmer, B., and Ciccarelli, O. (2018). Multiple sclerosis. *Lancet* 391, 1622–1636.

Tonra, J. R. (2002). Cerebellar susceptibility to experimental autoimmune encephalomyelitis in SJL/J mice: potential interaction of immunology with vascular anatomy. *Cerebellum* 1, 57–68. doi: 10.1080/147342202753203096

Tysiak, E., Asbach, P., Aktas, O., Waiczies, H., Smyth, M., Schnorr, J., et al. (2009). Beyond blood brain barrier breakdown–*in vivo* detection of occult neuroinflammatory foci by magnetic nanoparticles in high field MRI. *J. Neuroinflam.* 6, 1–8.

Tzschätzsch, H., Guo, J., Dittmann, F., Hirsch, S., Barnhill, E., Jöhrens, K., et al. (2016). Tomoelastography by multifrequency wave number recovery from time-harmonic propagating shear waves. *Med. Image Anal.* 30, 1–10. doi: 10.1016/j.media.2016.01.001

Wagner, S., Schnorr, J., Pilgrimm, H., Hamm, B., and Taupitz, M. (2002). Monomer-coated very small superparamagnetic iron oxide particles as contrast medium for magnetic resonance imaging: preclinical *in vivo* characterization. *Investig. Radiol.* 37, 167–177. doi: 10.1097/00004424-200204000-00002

Waiczies, H., Millward, J. M., Lepore, S., Infante-Duarte, C., Pohlmann, A., Niendorf, T., et al. (2012). Identification of cellular infiltrates during early stages of brain inflammation with magnetic resonance microscopy. *PLoS One* 7:e32796. doi: 10.1371/journal.pone.0032796

Wang, S., Hesse, B., Roman, M., Stier, D., Castillo-Michel, H., Cotte, M., et al. (2019). Increased retention of gadolinium in the inflamed brain after repeated administration of gadopentetate dimeglumine: a proof-of-concept study in mice combining ICP-MS and micro–and Nano–SR-XRF. *Investig. Radiol.* 54, 617–626. doi: 10.1097/rli.0000000000000571

Wang, S., Millward, J. M., Hanke-Vela, L., Malla, B., Pilch, K., Gil-Infante, A., et al. (2020). MR elastography-based assessment of matrix remodeling at lesion sites associated with clinical severity in a model of multiple sclerosis. *Front. Neurol.* 10:1382. doi: 10.3389/fneur.2019.01382

Wuerfel, J., Paul, F., Beierbach, B., Hamhaber, U., Klatt, D., Papazoglou, S., et al. (2010). MR-elastography reveals. *Neuroimage* 49, 2520–2525. doi: 10.1016/j.neuroimage.2009.06.018

Wuerfel, J., Tysiak, E., Prozorovski, T., Smyth, M., Mueller, S., Schnorr, J., et al. (2007). Mouse model mimics multiple sclerosis in the clinico-radiological paradox. *Eur. J. Neurosci.* 26, 190–198. doi: 10.1111/j.1460-9568.2007.05644.x

Xiong, B., Li, A., Lou, Y., Chen, S., Long, B., Peng, J., et al. (2017). Precise cerebral vascular atlas in stereotaxic coordinates of whole mouse brain. *Front. Neuroanat.* 11:128. doi: 10.3389/fnana.2017.00128

Xu, Z. S., Lee, R. J., Chu, S. S., Yao, A., Paun, M. K., Murphy, S. P., et al. (2013). Evidence of changes in brain tissue stiffness after ischemic stroke derived from ultrasound-based elastography. *J. Ultrasound Med.* 32, 485–494. doi: 10.7863/jum.2013.32.3.485

Xu, Z. S., Yao, A., Chu, S. S., Paun, M. K., McClintic, A. M., Murphy, S. P., et al. (2014). Detection of mild traumatic brain injury in rodent models using shear wave elastography: preliminary studies. *J. Ultrasound Med.* 33, 1763–1771. doi: 10.7863/ultra.33.10.1763

Zéphir, H. (2018). Progress in understanding the pathophysiology of multiple sclerosis. *Revue Neurol.* 174, 358–363. doi: 10.1016/j.neurol.2018.03.006

Conflict of Interest: The authors declare that the research was conducted in the absence of any commercial or financial relationships that could be construed as a potential conflict of interest.

Publisher's Note: All claims expressed in this article are solely those of the authors and do not necessarily represent those of their affiliated organizations, or those of the publisher, the editors and the reviewers. Any product that may be evaluated in this article, or claim that may be made by its manufacturer, is not guaranteed or endorsed by the publisher.

Publication 3

Clara Sophie Batzdorf, **Anna Sophie Morr**, Gergely Bertalan, Ingolf Sack, Rafaela Vieira Silva and Carmen Infante-Duarte, Sexual Dimorphism in Extracellular Matrix Composition and Viscoelasticity of the Healthy and Inflamed Mouse Brain, Biology, 2022

Journal Data Filtered By: **Selected JCR Year: 2020** Selected Editions: SCIE,SSCI
Selected Categories: **"BIOLOGY"** Selected Category Scheme: WoS
Gesamtanzahl: 93 Journale

Rank	Full Journal Title	Total Cites	Journal Impact Factor	Eigenfactor Score
1	BIOLOGICAL REVIEWS	17,047	12.820	0.019750
2	Physics of Life Reviews	1,942	11.025	0.003280
3	CURRENT BIOLOGY	78,289	10.834	0.116100
4	BIOSCIENCE	22,560	8.589	0.012470
5	eLife	68,113	8.140	0.287820
6	PLOS BIOLOGY	39,598	8.029	0.059920
7	BMC BIOLOGY	8,577	7.431	0.015750
8	Communications Biology	4,996	6.268	0.016030
9	PHILOSOPHICAL TRANSACTIONS OF THE ROYAL SOCIETY B-BIOLOGICAL SCIENCES	56,921	6.237	0.055730
10	Science China-Life Sciences	6,307	6.038	0.006960
11	BIOLOGICAL RESEARCH	2,563	5.612	0.002270
12	BIOELECTROCHEMISTRY	6,107	5.373	0.004870
13	PROCEEDINGS OF THE ROYAL SOCIETY B-BIOLOGICAL SCIENCES	64,652	5.349	0.061070
14	FASEB JOURNAL	54,279	5.191	0.044390
15	Current Opinion in Insect Science	3,455	5.186	0.008610
16	Biology-Basel	2,726	5.079	0.003990
17	QUARTERLY REVIEW OF BIOLOGY	4,781	4.875	0.000920
18	Life Science Alliance	1,208	4.591	0.004260
19	COMPUTERS IN BIOLOGY AND MEDICINE	9,751	4.589	0.011860
20	Biology Direct	2,265	4.540	0.002430
21	Geobiology	2,793	4.407	0.003600
22	BIOESSAYS	11,559	4.345	0.011680
23	ASTROBIOLOGY	4,963	4.335	0.005570
24	SAUDI JOURNAL OF BIOLOGICAL SCIENCES	6,487	4.219	0.007240
25	EXCLI Journal	2,642	4.068	0.002870
26	Interface Focus	2,863	3.906	0.004480
27	Life-Basel	1,851	3.817	0.003870
28	Biology Letters	12,880	3.703	0.016230
29	JOURNAL OF EXPERIMENTAL BIOLOGY	40,334	3.312	0.026860
30	JOURNAL OF BIOLOGICAL RHYTHMS	4,128	3.182	0.003270
31	YALE JOURNAL OF BIOLOGY AND MEDICINE	2,938	3.026	0.003300

biology

MDPI

Article

Sexual Dimorphism in Extracellular Matrix Composition and Viscoelasticity of the Healthy and Inflamed Mouse Brain

Clara Sophie Batzdorf [1], Anna Sophie Morr [2], Gergely Bertalan [2], Ingolf Sack [2], Rafaela Vieira Silva [1,3,†] and Carmen Infante-Duarte [1,*,†]

[1] Experimental and Clinical Research Center, Max Delbrück Center for Molecular Medicine and Charité—Universitätsmedizin Berlin, Corporate Member of Freie Universität Berlin and Humboldt-Universität zu Berlin, Lindenberger Weg 80, 13125 Berlin, Germany; clara.batzdorf@charite.de (C.S.B.); rafaela.vieira-da-silva@charite.de (R.V.S.)
[2] Department of Radiology, Charité—Universitätsmedizin Berlin, Corporate Member of Freie Universität Berlin and Humboldt-Universität zu Berlin, Charitéplatz 1, 10117 Berlin, Germany; anna-sophie.morr@charite.de (A.S.M.); gergely.bertalan@charite.de (G.B.); ingolf.sack@charite.de (I.S.)
[3] Einstein Center for Neurosciences Berlin, Charité—Universitätsmedizin Berlin, Corporate Member of Freie Universität Berlin and Humboldt-Universität zu Berlin, Charitéplatz 1, 10117 Berlin, Germany
* Correspondence: carmen.infante@charite.de
† Equally contributing senior authors.

Simple Summary: In multiple sclerosis (MS), an autoimmune disease of the central nervous system that primarily affects women, gender differences in disease course and in brain softening have been reported. It has been shown that the molecular network found between the cells of the tissue, the extracellular matrix (ECM), influences tissue stiffness. However, it is still unclear if sex influences ECM composition. Therefore, here we investigated how brain ECM and stiffness differ between sexes in the healthy mouse, and in an MS mouse model. We applied multifrequency magnetic resonance elastography and gene expression analysis for associating in vivo brain stiffness with ECM protein content in the brain, such as collagen and laminin. We found that the cortex was softer in males than in females in both healthy and sick mice. Softening was associated with sex differences in expression levels of collagen and laminin. Our findings underscore the importance of considering sex when studying the constitution of brain tissue in health and disease, particularly when investigating the processes underlying gender differences in MS.

Abstract: Magnetic resonance elastography (MRE) has revealed sexual dimorphism in brain stiffness in healthy individuals and multiple sclerosis (MS) patients. In an animal model of MS, named experimental autoimmune encephalomyelitis (EAE), we have previously shown that inflammation-induced brain softening was associated with alterations of the extracellular matrix (ECM). However, it remained unclear whether the brain ECM presents sex-specific properties that can be visualized by MRE. Therefore, here we aimed at quantifying sexual dimorphism in brain viscoelasticity in association with ECM changes in healthy and inflamed brains. Multifrequency MRE was applied to the midbrain of healthy and EAE mice of both sexes to quantitatively map regional stiffness. To define differences in brain ECM composition, the gene expression of the key basement membrane components laminin (*Lama4*, *Lama5*), collagen (*Col4a1*, *Col1a1*), and fibronectin (*Fn1*) were investigated by RT-qPCR. We showed that the healthy male cortex expressed less *Lama4*, *Lama5*, and *Col4a1*, but more *Fn1* (all $p < 0.05$) than the healthy female cortex, which was associated with 9% softer properties ($p = 0.044$) in that region. At peak EAE cortical softening was similar in both sexes compared to healthy tissue, with an 8% difference remaining between males and females ($p = 0.006$). Cortical *Lama4*, *Lama5* and *Col4a1* expression increased 2 to 3-fold in EAE in both sexes while *Fn1* decreased only in males (all $p < 0.05$). No significant sex differences in stiffness were detected in other brain regions. In conclusion, sexual dimorphism in the ECM composition of cortical tissue in the mouse brain is reflected by in vivo stiffness measured with MRE and should be considered in future studies by sex-specific reference values.

Citation: Batzdorf, C.S.; Morr, A.S.; Bertalan, G.; Sack, I.; Silva, R.V.; Infante-Duarte, C. Sexual Dimorphism in Extracellular Matrix Composition and Viscoelasticity of the Healthy and Inflamed Mouse Brain. *Biology* **2022**, *11*, 230. https://doi.org/10.3390/biology11020230

Academic Editor: Xinhua Shu

Received: 17 December 2021
Accepted: 28 January 2022
Published: 31 January 2022

Keywords: multiple sclerosis; experimental autoimmune encephalomyelitis; sexual dimorphism; brain viscoelasticity; magnetic resonance elastography; extracellular matrix; cerebral cortex; neuroinflammation; basement membrane

1. Introduction

Multiple Sclerosis (MS) is a chronic inflammatory demyelinating disease of the central nervous system (CNS) affecting approximately 2.8 million people worldwide [1]. It displays a prominent sexual dimorphism in relation to susceptibility, incidence, pathology, and progression [2]. In women, the risk of MS is three times higher than in men, with disease onset occurring at earlier ages, but, generally, with slower progression [3–8]. While the higher susceptibility in women is associated with sex hormones and a differential immune response to inflammation, worsened progression in men is linked to enhanced neurodegeneration [2,7,9]. Moreover, MS incidence in women has been increasing over the last decades probably due to a sex-dependent response to environmental and lifestyle factors [5,6], with a current estimated female to male ratio of 2–4:1 [1,10].

The mechanical properties of the brain investigated by magnetic resonance elastography (MRE) also display sex differences. MRE is a non-invasive method that, based on the induction of shear waves through harmonic vibrations, allows the assessment of viscoelastic properties of the brain tissue *in vivo* [11]. MRE of healthy individuals showed that male brains were softer than female brains [12–14]. In response to inflammation, however, the brains of female MS patients exhibited stronger reduction in viscoelasticity compared to age-matched healthy males [12,15,16]. Similarly, in the MS mouse model, experimental autoimmune encephalomyelitis (EAE), we previously demonstrated a reduction in brain stiffness in sick mice [17–19]. This softening behavior seemed to be associated with inflammatory processes such as immune cell infiltration, demyelination, and loss of the blood–brain barrier (BBB) integrity, as well as remodeling of the extracellular matrix (ECM) [18–21]. We also recently showed that brain viscoelastic properties seem to be particularly dependent on ECM organization and axonal structure [22].

Furthermore, in MS, the ECM composition at lesion sites appears to be altered. Active lesions are marked, among others, by the deposition of fibronectin, correlating with BBB disruption and the accumulation of laminin and collagen type IV in the basement membrane and perivascular cuffs [18,23,24]. Moreover, it has been reported that estrogen can influence the production of matrix metalloproteinases [25,26], indicating that the degradation of ECM components may be influenced by sex.

Laminins, collagens, and fibronectin are mainly found in the ECM of the basement membrane in the brain and play an important role in the regulation of the BBB integrity [27]. Furthermore, collagen type I provides tensile strength and stiffness, while collagen type IV is responsible for flexible networks [28]. However, how sex-specific differences influence neuroinflammatory remodeling of the ECM and, consequently, viscoelastic brain properties, remains unclear.

Therefore, the aim of this study was to investigate sex effects on brain viscoelasticity in healthy and EAE mice via multifrequency MRE, which allows the accurate analysis of small cerebral regions [29], and to analyze sexual dimorphism in the remodeling of brain ECM.

2. Materials and Methods

2.1. Animals and EAE Model

All animal experiments were approved by the Berlin State Office for Health and Social Affairs (LAGeSo, G106/19) and conducted in strict adherence to the European

guidelines for the care and use of laboratory animals under directive 2010/63/EU of the European Parliament and of the Council of 22 September 2010.

SJL mice that were 10–15 weeks old (Janvier, SAS, Le Genest Saint Isle, France), and are known for exhibiting sex-dependent susceptibility to EAE induction [30,31], were investigated. The mice were housed under standard conditions with a 12:12h light–dark-cycle and ad libitum access to food and water. The four experimental groups consisted of female healthy (n = 14), male healthy (n = 14), female EAE (n = 23) and male EAE (n = 19) mice. To induce EAE, the animals were immunized with 250 µg of proteolipid peptide $PLP_{139–151}$, emulsified in 100 µL complete Freund's adjuvant (Thermo Fisher Scientific, Waltham, MA, USA) and 800 µg Mycobacterium tuberculosis H37Ra (Difco, Detroit, MI, USA). Furthermore, 250 ng of pertussis toxin (List Biological Laboratories, Campbell, CA, USA) resuspended in phosphate-buffered saline (PBS) (Gibco, Grand Island, NY, USA) was injected intraperitoneally on day 0 and day 2 after immunization. Mice were monitored daily for clinical signs and scored as follows: 0.5—tail paresis or weak righting reflex; 1—tail plegia or tail paresis and weak righting reflex; 1.5—tail plegia and weak righting reflex; 2.0—additional hind limb paresis; 3.0—paraplegia; 4.0—additional forelimb paresis; 5.0—moribund or dead animal. To comply with animal welfare guidelines, all mice with a score higher than 3 were euthanized and removed from the study (n_{female} = 2, n_{male} = 1). The EAE model using SJL mice has been shown to be more suitable for cerebral MRE studies than EAE in C57BL/6, since PLP-induced EAE in SJL consistently leads to the development of brain lesions and to elasticity alterations in brain structures [17–19,32,33].

2.2. MRE Acquisition

MRE acquisition was performed on a preclinical 7 Tesla MRI scanner (BioSpec, Bruker, Ettlingen, Germany) operated with ParaVision 6.1 software (Bruker, Billerica, MA, USA) using a 20-mm diameter 1H-RF quadrature volume coil (RAPID Biomedical, Rimpar, Germany). The set up was similar to that previously described [19,29]. EAE mice were scanned based on their individual score at the peak of disease around day 10–12 after immunization. Age-matched healthy control mice were scanned on the same experimental days. To this end, mice were placed on a custom-built animal holder and anesthetized with 1.5–2.0% isoflurane in 30% O_2 and 70% N_2O by mask under continuous respiratory monitoring, using a pressure-sensitive pad placed on the dorsal thorax (Small Animal Instruments Inc., Stony Brook, NY, USA). Body temperature was monitored using a rectal probe and kept constant by circulating warm water through pads integrated in the animal holder. External vibrations were created by a custom-made driver system, using a non-magnetic piezoceramic actuator, and translated to the skull via a transducer rod to the head cradle of the mouse to induce shear waves in the brain [19]. Multifrequency single-shot MRE was conducted by consecutively exciting five external vibrational frequencies (1000, 1100, 1200, 1300, and 1400 Hz) which were encoded by a single-shot EPI sequence. Seven coronal slices with a slice thickness of 0.8 mm and a 0.18 mm × 0.18 mm spatial resolution were acquired. The covered brain region was consistent with previous MRE studies [19,29], which facilitated the comparison of values. Further imaging parameters were TA = 9 min, TE = 53 ms, TR = 4000 ms, FOV = 16.2 mm × 10.8 mm, and matrix size = 90 × 60.

2.3. Data Reconstruction

Multifrequency MRE data were reconstructed using the tomoelastography post-processing pipeline, as described previously [29]. Viscoelasticity parameter maps were obtained based on shear wave speed c (in m/s), as a marker for tissue stiffness, and phase angle φ (in rad, also denoted as loss angle of the complex shear modulus), as a marker of tissue fluidity. Regions of interest (cerebral cortex, hippocampus, thalamic area, whole coronal midbrain slice) were defined manually, according to anatomical structures in a blinded fashion using MATLAB (Version 9.4 (R2018a). The MathWorks Inc.; 2018, Natick, MA, USA). Due to technical errors, $n_{male\ naïve}$ = 1 had to be excluded from the MRE analysis.

2.4. Tissue Processing

Animals were sacrificed directly after the MRE measurements with an overdose of ketamine (Inresa Arzneimittel GmbH, Freiburg im Breisgau, Germany) and xylazine (CP-Pharma, Burgdorf, Germany) followed by cardiac perfusion with PBS (Gibco, Grand Island, NY, USA). The brains were extracted and one hemisphere was preserved in 4% paraformaldehyde (PFA) (Carl Roth, Karlsruhe, Germany) overnight at 4 °C, following dehydration in 30% sucrose at 4 °C. Afterwards, the tissue was embedded in O.C.T. (Sakura Finetek, Tokyo, Japan) and stored at −80 °C until preparation for histological staining. From the other half of the brain, the cerebral cortex and hippocampus were carefully extracted under a microscope, then freeze-dried in liquid nitrogen and stored at −80 °C for gene expression analysis. Post-MRE tissue processing was performed on a subgroup of animals ($n_{\text{female naïve}} = 6$, $n_{\text{male naïve}} = 6$, $n_{\text{female EAE}} = 6$, $n_{\text{male EAE}} = 7$).

2.5. Gene Expression Analysis

RNA was extracted from the hippocampus and the cerebral cortex using the Quick-RNA-MiniPrep Kit (Zymo Research, Irvine, CA, USA), and cDNA synthesis was carried out with the High-Capacity cDNA Reverse Transcription Kit (Thermo Fisher Scientific, USA), according to the manufacturer's instructions. Quantitative RT-PCR was performed with the QuantStudio 6 Flex Real-Time PCR system (Thermo Fisher Scientific, USA) using TaqMan® probes for the following genes: *Lama4, Lama5, Col4a1, Col1a1,* and *Fn1* (Thermo Fisher Scientific, USA; Supplementary Table S1). *Hprt1* served as the endogenous reference [34,35]. Collagens (*Col4a1*, *Col1a1*) provide fibrillar and net-like structures [28], while laminins (*Lama4*, *Lama5*) and fibronectin (*Fn1*), which are glycoproteins, are important for cellular attachment to the matrix [36,37] and influence collagen organization [38]. Therefore, we considered these proteins to be important regulators of the mechanical properties of the brain ECM.

2.6. Histology

For immunofluorescence staining the tissue was cut into 6 µm slices, thawed, fixed with 4% PFA for 15 min and then blocked with PBS containing 8% horse serum (Gibco, USA), 3% bovine serum albumin (Sigma-Aldrich, Darmstadt, Germany) and 1% Triton TM X-100 (Thermo Fisher Scientific, USA) for one hour at room temperature. Sections were then incubated overnight with the primary antibodies at 4 °C, diluted in PBS containing 20% blocking solution. As primary antibodies, we used mouse anti-fibronectin, 1:400 (Novus Biologicals, 2755-8, Littleton, CO, USA), rabbit monoclonal anti-collagen IV (EPR22911-127), 1:400 (Abcam, ab236640, Cambridge, UK) and rat monoclonal anti-CD3 (17A2), 1:100 (Invitrogen, 14-0032-82, Carlsbad, CA, USA). On the following day, sections were incubated with secondary antibodies: anti-rat, anti-mouse, and anti-rabbit, conjugated with Alexa-Fluor 488 or 568, 1:500 (Invitrogen, Carlsbad, CA, USA) for one hour at room temperature and counterstained with 4',6-diamidino-2-phenylindole (DAPI) at 1:10,000. Images were acquired at 20 times magnification with the Keyence Fluorescence Microscope BZ-X800 (Keyence Corporation, Osaka, Japan).

2.7. Statistical Analysis

Analyses were performed using GraphPad Prism 9.3 (GraphPad Software, La Jolla, CA, USA) with significance levels defined as $*p < 0.05$, $**p < 0.01$, $***p < 0.001$. All p-values below 0.1 are reported. Statistical group comparison was performed with an unpaired two-tailed t test, or with two-way analysis of variance (ANOVA) with post-hoc pairwise comparisons where appropriate. Values are reported with means, standard deviation (SD) and a 95% confidence interval (CI). Graphs are reported with means and a 95% CI.

3. Results

3.1. Sex-Specific Viscoelastic Properties of Healthy Mouse Brain

To determine sex differences in the brain's mechanical properties, the viscoelasticity of healthy female (♀) and male (♂) midbrains were compared. The predefined regions of interest were averaged for mean values of shear wave speed c (in m/s) and fluidity φ (in rad). Representative MRE parameter maps for the whole midbrain slice covering the cortex, hippocampus, and thalamus are depicted in Figure 1.

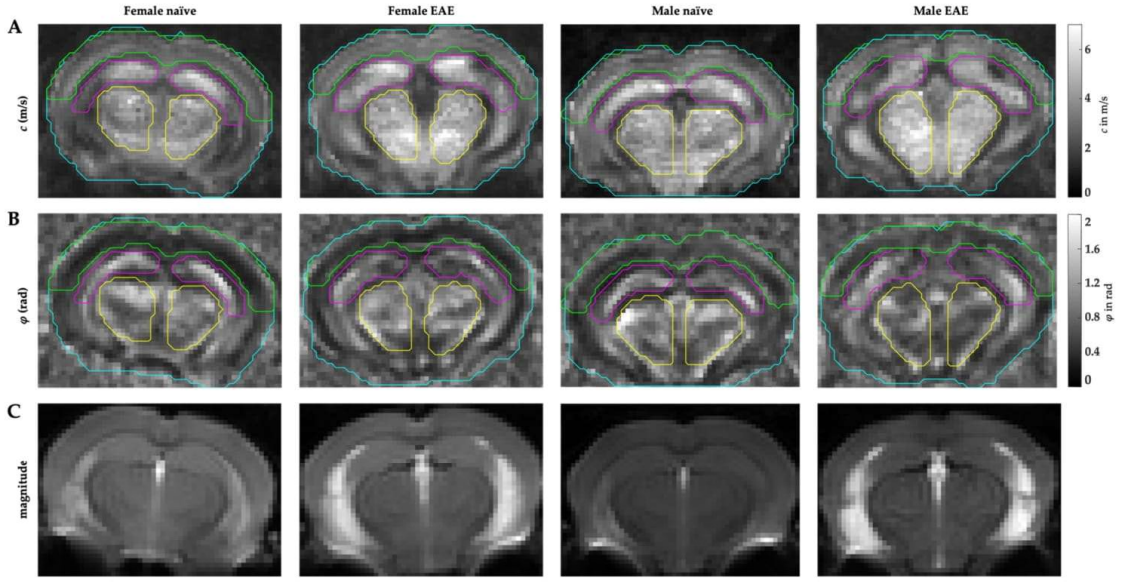

Figure 1. Representative parameter maps of the coronal murine midbrain with defined regions of interest in female/male naive and female/male EAE. (**A**) stiffness maps in c (m/s), (**B**) fluidity-maps in φ (rad), (**C**) anatomical magnitude images (arbitrary units). Cyan = whole midbrain, green = cerebral cortex, magenta = hippocampus, yellow = thalamic area.

No differences in c or φ were observed when comparing the whole midbrain area of males and females (Figure 2A,B). However, sex became an important variable when considering the cortical viscoelasticity, which was on average 9% softer in males than in healthy age-matched females (mean c_{female} = 2.90 ± 0.33 m/s, 95%CI 2.71–3.09 m/s; mean c_{male} = 2.65 ± 0.29 m/s, 95%CI 2.63–2.78 m/s; p = 0.044). No sex-related differences in c or φ for the hippocampus or the thalamic area were detected.

3.2. Differences in Extracellular Matrix Composition in the Healthy Brain of Males and Females

Gene expressions of laminins (*Lama5* and *Lama4*), collagens (*Col4a1* and *Col1a1*), and fibronectin (*Fn1*) were quantified in the cerebral cortex and hippocampus as a control region in healthy male (n = 6) and age-matched female (n = 6) mice. Figure 3 represents relative gene expression levels in healthy males compared to females. Laminin and collagen type IV expression was significantly lower in the male cortex than in the female one (*Lama5* −4.0-fold, p = 0.019; *Lama4* −3.4-fold, p = 0.006; *Col4a1* −1.6-fold, p = 0.029), while collagen type I expression did not present sexual dimorphism (Figure 3A). In contrast, a higher expression of fibronectin was found in the cortex of healthy males (*Fn1* 1.9-fold, p = 0.002). No differences related to sex were observed in the hippocampus (Figure 3B).

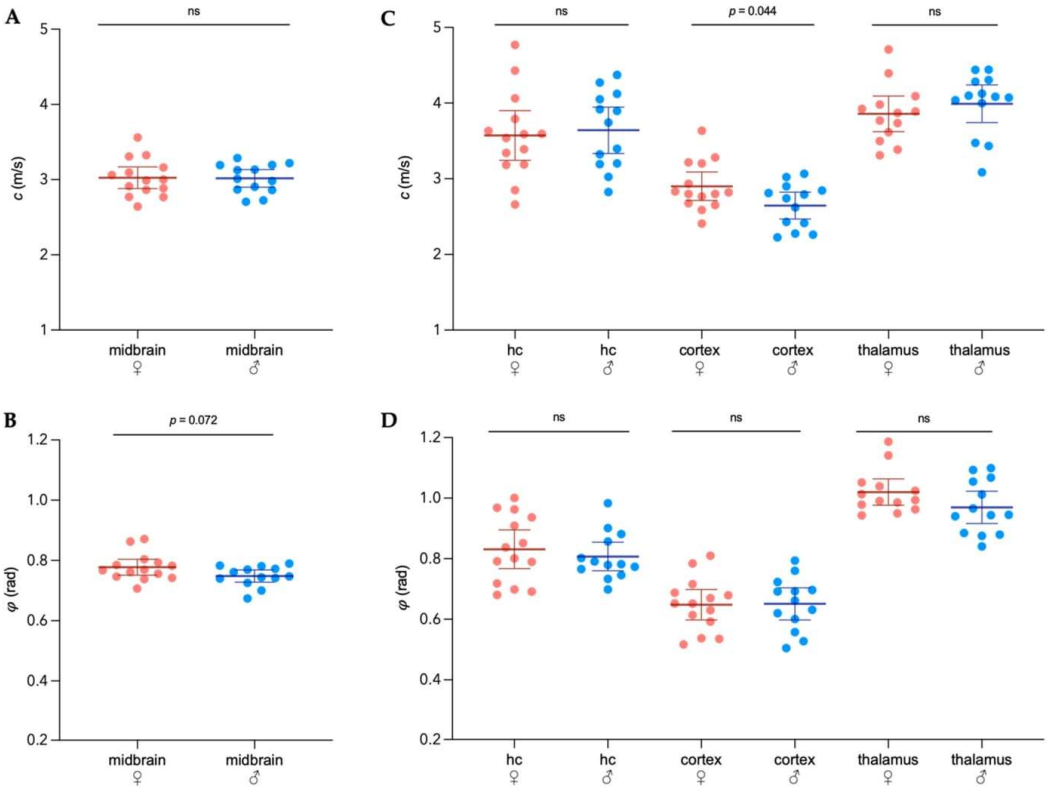

Figure 2. Sexual dimorphism in viscoelastic properties of healthy adult mouse brains. Mean shear wave speed c in m/s (**A**) and fluidity φ in rad (**B**) in the whole coronal section of the midbrain of female and male mice. (**C**) Regional analysis of stiffness (c) between sexes in the cortex, hippocampus, and thalamus. (**D**) Regional assessment of fluidity (φ). $n_{female} = 14$, $n_{male} = 13$, hc = hippocampus; representation of individual data points with mean and 95% CI. Group comparison performed by t test. ns = not significant.

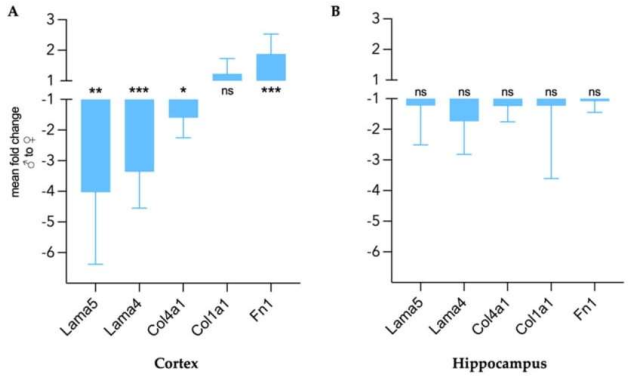

Figure 3. Sex differences in gene expression of ECM components in healthy cerebral cortex (**A**) and hippocampus (**B**) expressed as mean fold change of male gene expression compared to female with 95% CI. $n_{female} = 6$, $n_{male} = 6$. Group comparison performed with unpaired t test with Welch correction.

Lama5 = laminin α5, *Lama4* = laminin α4, *Col4a1* = collagen type IV α1, *Col1a1* = collagen type I α1, *Fn1* = fibronectin 1. *$p < 0.05$, **$p < 0.01$, ***$p < 0.001$, ns = not significant.

3.3. Sex-specific Changes of Brain Viscoelastic Properties during EAE

Next, we investigated whether viscoelasticity changes of the brain following inflammation revealed a sexual dimorphism. For that, data from healthy mice were compared with a cohort of female and male mice at the peak EAE ($n_{female} = 21$, mean score = 2.3; $n_{male} = 18$, mean score = 2.3).

Only the male EAE group showed a 5% global reduction of stiffness in the midbrain ($c_{male\ naïve} = 3.02 \pm 0.19$ m/s, 95%CI 2.90–3.13 m/s; $c_{male\ EAE} = 2.86 \pm 0.15$ m/s, 95%CI 2.78–2.93 m/s; $p = 0.024$) when averaging the whole coronal section, while fluidity remained unaltered (Figure 4A). In the hippocampus, no significant stiffness changes were observed at peak EAE in both sexes, although a trend could be seen for male EAE.

When considering different brain regions, the elasticity of the cortex was the most affected during EAE. We detected a 7% reduction for female and 6% for male mice when compared with age-matched control mice ($c_{female\ naïve} = 2.90 \pm 0.33$ m/s, 95%CI 2.71–3.09 m/s; $c_{female\ EAE} = 2.70 \pm 0.16$ m/s, 95%CI 2.63–2.78 m/s; $p = 0.013$; $c_{male\ naïve} = 2.65 \pm 0.29$ m/s, 95%CI 2.63–2.78 m/s; $c_{male\ EAE} = 2.49 \pm 0.12$ m/s, 95%CI 2.43–2.55 m/s; $p = 0.067$). The comparison between sexes revealed, however, no sex-related differences in the overall cortical softening during inflammation. The male EAE cortex was approximately 8% softer than the female EAE cortex ($p = 0.006$), maintaining the sex-dependent difference in stiffness observed in healthy mice (Figure 4B, center). In the thalamus, no inflammation-related changes of the mechanical properties were observed (Figure 4B, right). In both sexes, regional fluidity was not affected by EAE (Supplementary Figure S1).

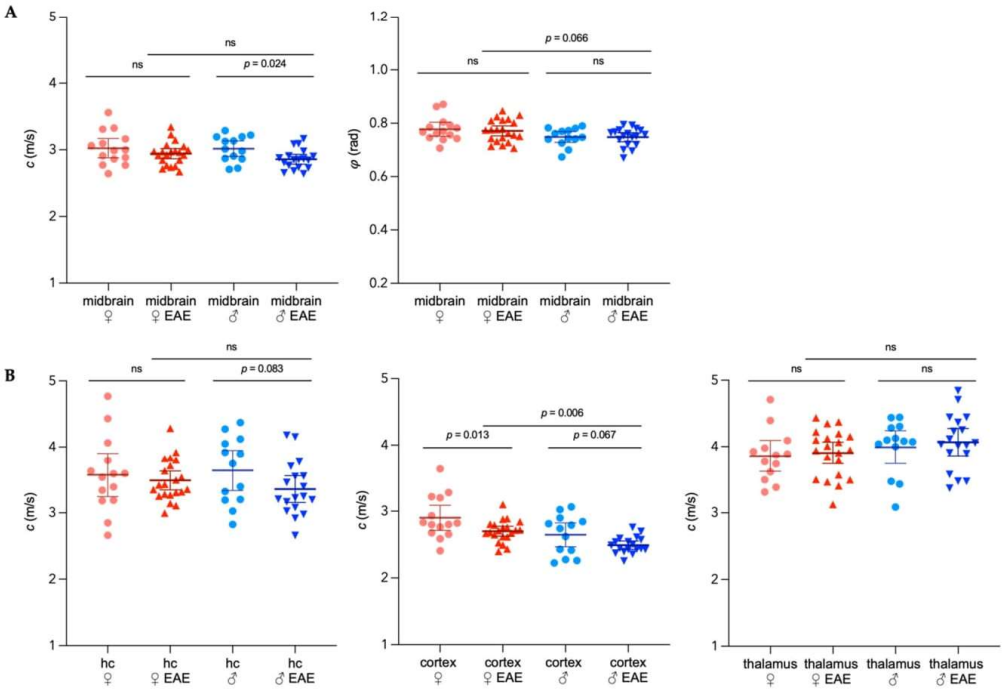

Figure 4. Sex-specific viscoelastic properties of the mouse brain in healthy conditions and EAE. (**A**) Shear wave speed *c* in m/s and fluidity φ in rad in the whole coronal midbrain. (**B**) Regional distribution of *c* in the hippocampus (hc), cortex and thalamic area; light red = healthy female; dark red =

EAE female; light blue = healthy male; dark blue = EAE male. Representation of individual data points with mean and 95%CI. $n_{female\ naive}$ = 14, $n_{male\ naive}$ = 13, $n_{female\ EAE}$ = 21, $n_{male\ EAE}$ = 18. Two-way ANOVA with Fisher's LSD post-hoc comparisons. ns = not significant.

3.4. Extracellular Matrix Remodeling in Female and Male EAE Brains

To assess inflammation-induced changes of the ECM components that appeared to be differentially expressed in male and female tissues, we investigated the gene expression levels of laminins, collagen type I and IV and fibronectin in the cerebral cortex and hippocampus of healthy and EAE mice. As shown in Figure 5A and Table 1, at peak EAE, the cortical expression of *Lama4* and *Lama5* increased similarly in both sexes (all $p < 0.05$). Given the baseline differences between healthy animals, their expression remained significantly higher in the female EAE group compared to the male (*Lama5* 3.85-fold, *Lama4* 3.86-fold, all $p < 0.001$) (Table 1). However, for *Col4a1* we observed a 3.0-fold increase in the cortex in female EAE and 2.0-fold in male EAE (all $p < 0.01$) in comparison to the respective healthy group, augmenting the initial sex difference from 1.6-fold in healthy mice to 2.38-fold ($p < 0.001$) in EAE. In addition, a decreased expression of *Col1a1* (−2.1-fold, $p < 0.001$) and *Fn1* (−1.4-fold, $p = 0.018$) was observed in the male cortex.

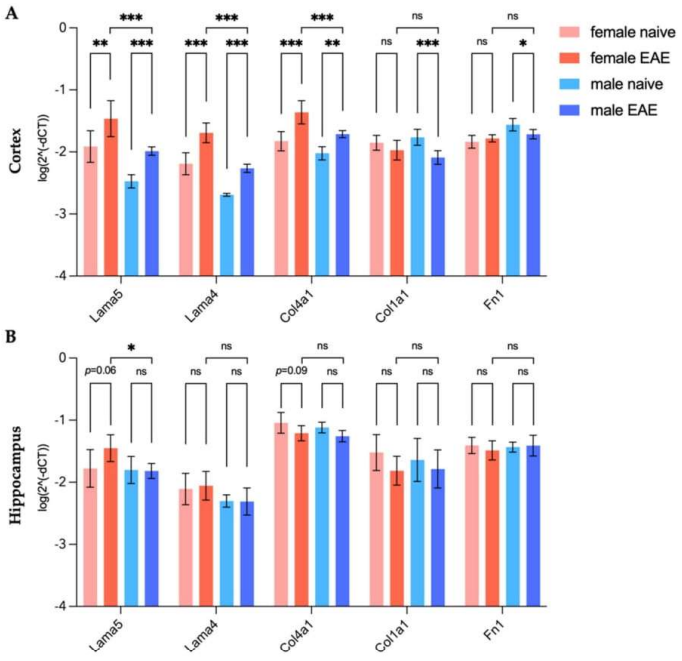

Figure 5. Sex-specific gene expression of ECM targets in healthy and EAE mice in the cortex (**A**) and hippocampus (**B**) relative to endogenous reference *Hprt1*. Representation of mean $\log[2^{(-\Delta CT)}]$ with 95% CI. n female naive = 6, n male naive = 6, n female EAE = 6, n male EAE = 7. Two-way ANOVA with Tukey's post-hoc comparisons. $^{*}p < 0.05$, $^{**}p < 0.01$, $^{***}p < 0.001$, ns = not significant.

Table 1. Sex-specific fold changes in gene expression of ECM components in EAE compared to healthy and between EAE in cortex and hippocampus.

Gene	Cortex			Hippocampus		
	♀ EAE/naive	♂ EAE/naive	EAE ♂/♀	♀ EAE/naive	♂ EAE/naive	EAE ♂/♀
Lama5	2.91	3.04	−3.85	1.83	−1.08	−2.42

Lama4	3.10	2.70	−3.86	1.08	1.11	−1.69
Col4a1	2.99	2.01	−2.38	−1.51	−1.37	−1.12
Col1a1	−1.29	−2.12	−1.34	−2.07	−1.33	1.26
Fn1	1.12	−1.43	1.18	−1.19	1.14	1.24

In the hippocampus (Figure 5B), we observed mild effects of inflammation on the expression of the selected ECM-components. *Lama5* expression remained unaltered for males at peak EAE, but increased 1.83-fold in females ($p = 0.064$), leading to a significant 2.41-fold difference ($p = 0.025$) between the sexes in the disease state (Figure 5B). Other investigated genes did not show any significant changes in the hippocampus regarding disease status or sex.

To visualize the ECM remodeling in both sexes and confirm the gene expression data, we performed representative immunohistological stainings in the cerebral cortex of two of our targets, fibronectin and collagen type IV. A representative cortical image of each group is shown in Figure 6. Collagen type IV was present around vessel-like structures, resembling the formation of the endothelial basement membranes (Figure 6A). Corroborating gene expression data, an upregulation of collagen type IV was observed in EAE mice for both sexes, compared to their corresponding healthy controls, with especially pronounced expression in female EAE. Similarly, fibronectin was also present in vessel-like structures, as demonstrated in Figure 6B. Interestingly, in healthy males, fibronectin appeared widely distributed around cell bodies.

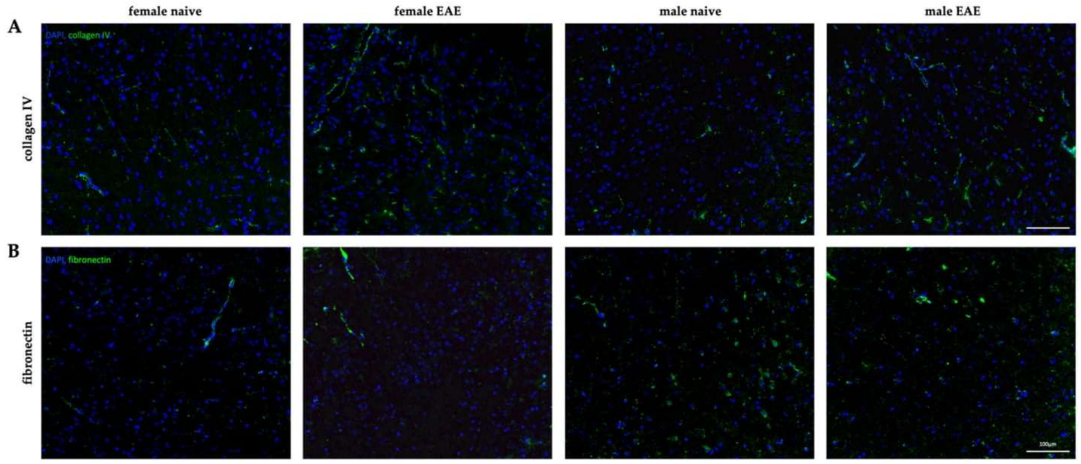

Figure 6. Sexual dimorphism in cortical ECM remodeling in EAE. (**A**) Immunofluorescence of collagen type IV (green) in healthy condition (naive) and at peak EAE for female (left) and male (right) cortices. (**B**) Cortical fibronectin (green) staining of female (left) and male (right) healthy and EAE mice. DAPI (blue). 20× magnification. Scale: 100 µm.

Additionally, to investigate whether ECM remodeling was associated with the presence of leukocyte infiltration, the cortical tissue was stained for CD3 to identify perivascular infiltrates in the cerebral cortex. Only one out of five male EAE mice presented a cortical perivascular lesion, and no leukocyte infiltrate was detected in females (Supplementary Figure S2). This indicates that the observed changes affecting elasticity and ECM composition in EAE were not related to acute lesion formation but diffuse inflammatory events.

4. Discussion

In this study, we built on our previous work on ECM alterations during neuroinflammation investigated by MRE, and further focused on sexual dimorphism, which potentially affects ECM composition and brain viscoelasticity. Our data provided evidence of sexual dimorphism in the ECM of cortical tissue, namely with respect to basement membrane proteins that may directly impact tissue structure or, as a result of the local inflammatory process, indirectly contribute to the observed divergence in tissue stiffness and the response to neuroinflammation.

Using MRE, we demonstrated here, for the first time, that the murine healthy brain exhibits sex-dependent differences in mechanical properties. Stiffness differences seem to primarily affect the cerebral cortex, as the male healthy cortex was, on average, 9% softer than the female one. This data is in line with previous MRE studies in humans that indicated significant sex differences in healthy brain viscoelasticity, with male brains being 9 to 11% softer, on average [12,13].

Furthermore, we demonstrated a significantly higher expression of laminin and collagen type IV in the healthy female cortex, while fibronectin was about two times more expressed in the male cerebral cortex than in the female cortex. Laminin, collagen type IV, and fibronectin are predominantly located within the basement membrane of CNS tissue [23,27]. Since these components have been shown to have relevant mechanical features [28,39–46] (extensively reviewed by [47–49]), our results indicate that differences in the constitution of the basement membrane may have an impact on cortical stiffness in a sex-specific manner.

In this line, sexual dimorphism has been reported in non-neuronal ECM, such as in tendons or vocal folds [50,51]. Moreover, estradiol and testosterone have been reported to have a differential effect on fibronectin synthesis depending on the investigated cells, which is in agreement with our results on the high fibronectin to collagen ratio in the male cortex [52]. Likewise, collagen turnover seems to exhibit a strong sex-dependence across the lifespan, with pronounced changes in women around menopause [53], and the connection between collagen content in the skin and circulating estrogen levels is well established [54]. Nonetheless, we cannot exclude that cellular differences between the female and male cortex may have contributed to the observed sex-specific disparity in stiffness. Studies in stroke models suggest a correlation between stiffness and neuronal cell count [55], which has been shown to differ between sexes [56]. While men seem to have more cortical neurons, female cerebral cortices show considerably larger neuropil [56,57]. On the other hand, cellular composition directly influences ECM configuration regarding its components, as well as post-translational processing such as cross-linking [28] which, then again, influences mechanical properties [41] and thereby cannot be considered as an independent variable.

No sex-specific differences in viscoelastic properties of the hippocampus were observed in our study, although more microglia and astrocytes are present in the dentate gyrus of female mice [58], while the neuronal density in the same area seems to be higher in males [59]. In addition, we did not observe differences in viscoelastic properties of the thalamus, which is in line with previous data in humans that showed no sexual dimorphism in the deep gray area [14]. Nonetheless, future studies should address possible viscoelastic changes in thalamic subregions. This will be of particular interest since the lateral posterior nucleus, the mouse homologue for the human pulvinar nucleus, has been shown to be functionally connected to cortical areas including auditory, visual, and somatosensory cortices [60,61] and to present sex-dependent differences in connectivity [62].

Under neuroinflammatory conditions, we observed a mild effect in females and a significant softening of the midbrain of 5% in male EAE, although previous studies reported a global softening in female EAE brains [17–19] as well as for MS patients of both sexes [12]. This discrepancy could be explained by the limitation of the analyzed region, which was restricted to a single coronal slice, and did not cover the usually affected cerebellum or optic nerve [63,64]. Another factor to consider when comparing these results with our previous

MRE studies [17–19,32] is our current focus on regional viscoelasticity values based on multifrequency inversion, which allows a higher resolution, and is therefore more sensitive to regional alterations, as studies in human subjects have shown [65–67].

When assessing regional mechanical properties, both female and male mice showed a similar degree of cortical softening during EAE. In both sexes, inflammation led to reduced stiffness, resulting in an 8% softer cortex in males than females in EAE, which is similar to the intersexual difference of 9% observed in healthy mice. No significant effects of inflammation on tissue elasticity were observed for the other investigated regions. Thus, multifrequency MRE revealed the murine cortex as the brain region with the largest sex-specific variation in stiffness under normal and neuroinflammatory conditions.

Interestingly, this effect was reflected by the gene expression of main proteins forming the ECM basement membrane, which presented pronounced sex differences in the cortex, and almost none in the hippocampus. In the cerebral cortex, both female and male EAE showed significantly higher expression of laminins and collagen type IV compared to healthy mice. This is in coherence with previous work on glial scars, attributing tissue softening to the enhanced expression of laminin and collagen type IV [68]. However, our results also revealed higher laminin and collagen expression in the healthy female cortex compared to the softer healthy male cortex. Nonetheless, previous work has indicated that tissue stiffness is intricately regulated by the interaction of cellular adhesion and matrix composition, providing seemingly paradoxical results when comparing healthy and pathological tissue properties [69]. Additionally, stiffness of collagen type IV has been shown to be dependent on the degree of crosslinking [41] which was not investigated here, and might explain the discrepancies between data in healthy and diseased tissue, since neuroinflammation triggers an increase in ECM degradation [70].

In both MS and EAE, deposition of basement membrane molecules associated with activated microglia in the vicinity of white matter lesions contribute to the disruption of the BBB integrity [23,24,71]. Our histological data support the elevated presence of collagen type IV around vessel-like structures in the cortex in EAE, while we did not observe perivascular leukocyte infiltration in that region. This is expected from peptide-induced EAE pathology, where inflammation mainly affects the spinal cord, cerebellum, and the optic nerve [63], and does not habitually lead to cortical lesions [64]. Pathological changes in the cortex are proposed to be directly related to spinal lesion formation via Wallerian degeneration [72], but are also highly dependent on meningeal inflammation with soluble factors leading to demyelination and neurodegeneration [73]. Therefore, we propose that the cortical changes observed here, which differ greatly from ECM remodeling described in white matter lesions [18,23], result from underlying meningeal and spinal inflammation rather than from the infiltration of leukocytes into the cortical parenchyma.

Obviously, alterations of the basement membrane cannot solely explain the elasticity changes observed in the cortical tissue, but could rather reflect the inflammatory, activated state of matrix-producing cells, such as astrocytes, oligodendrocyte precursor or endothelial cells [74]. It is reasonable to posit that stiffness changes result, at least partially, from the inflammatory state of these cells. Nonetheless, another relevant aspect that cannot be discarded, is the influence of basement membrane components on the interstitial matrix, the largest component of the brain ECM [75]. Since the interstitial matrix is in part constituted by laminins and collagens [27], it is possible that enhanced expression of such components at vascular sites leads to a partial diffusion into the parenchymal space [74]. These molecules could then interact with and alter the ECM of other compartments, such as the perineuronal matrix, resulting in a major structural effect contributing to the elastic changes here discussed.

The inflammation-induced upregulation of *Lama4* and *Lama5* was about 3-fold in both sexes. However, considering baseline differences, their expression was still about 4-fold higher in female EAE than in male EAE, demonstrating that the effect size of the inherent sex differences was larger than the observed inflammatory effect. In addition, we

observed a downregulation of *Col1a1* and *Fn1* in EAE male cortices. The histological correlates showed a reduction of fibronectin in the inflamed male cortex compared to the healthy group, affecting not only the vasculature but also fibronectin in association with cortical nuclei. This is in contrast with previous research, which described the deposition of fibronectin in MS lesions [23,24] in association with perivascular infiltrates and tissue softening [18]. Given the absence of leukocyte infiltrates in the cortex, it is conceivable that cortical fibronectin and collagen type I levels were not increased, and may not have contributed to cortical softening. As most of our knowledge about neuroinflammatory ECM remodeling stems from white matter lesions [23], ECM changes in normal-appearing gray matter are still not well understood.

In addition, none of the investigated regions exhibited changes in tissue fluidity φ between naive and EAE mice of the same sex, which has been equally described in our previous studies in acute EAE [17–19,32]. Tissue fluidity is influenced by the motility of structure elements in the viscoelastic network [76] and, thus, seems to reflect cellular confinement [77]. This confinement is affected by the interaction and organization of macromolecular networks in the ECM [77,78]. Since we did not observe any changes in fluidity properties between healthy and EAE brains across all regions, we expect the complexity of the tissue architecture to be similar between sexes and not affected by inflammation.

Taken together, our data on the cortical remodeling of the ECM in the context of EAE suggests sex-specific processes. Sex-dependent changes in the expression levels of basement membrane proteins seem to have the same net effect on macroscopic viscoelastic properties of the cortex because we observed a similar amount of softening in both sexes. Since tissue stiffness depends on both the cellular and ECM composition, as well as their structural arrangement [19,22,41,55,68,79], the combination of up- and downregulation of different matrix components may counterbalance their effect on mechanical properties and may even serve as a protective measure. Future studies with larger group sizes will allow for in-depth analyses of the individual contribution of matrix components to the viscoelastic behavior of the brain. Furthermore, as viscoelastic matrix properties have been shown to strongly influence neuronal and astrocytic growth as well as the differentiation of oligodendrocytes [80–82], it remains to be determined how the absolute sex differences in cortical stiffness affect cellular behavior and remyelination in EAE.

5. Conclusions

In conclusion, by applying multifrequency MRE we were able to demonstrate, for the first time, significant sex differences in viscoelastic properties of the cortex of healthy and EAE mice. Softening was not associated with lesion formation but with ECM remodeling, as reflected by the gene expression changes observed for collagen type IV, laminin, and fibronectin. Understanding sexual dimorphism in the composition of the ECM is important in neurobiology, and might help understand sex-dependent responses to environmental factors, as well as provide guidance for the development of individualized treatments of MS. Moreover, possible implications of sex-specific mechanical properties on the cellular behavior in neuroinflammatory conditions need to be investigated. Regarding future imaging studies, sex-specific reference values for MRE in MS should be established.

Supplementary Materials: The following are available online at www.mdpi.com/article/10.3390/biology11020230/s1, Figure S1: Regional distribution of sex-specific fluidity φ in the midbrain of the mouse in healthy and EAE. Figure S2: Singular cortical lesion in the midbrain in male EAE., Table S1: Gene symbols and corresponding primers for TaqMan® assays.

Author Contributions: Conceptualization, C.I.-D., C.S.B. and R.V.S.; methodology, C.S.B., R.V.S. and A.S.M.; software, C.S.B. and A.S.M.; validation, C.S.B., R.V.S. and A.S.M.; formal analysis, C.S.B..; investigation, C.S.B., R.V.S. and A.S.M.; resources, C.I.-D. and I.S.; data curation, C.S.B.; writing—original draft preparation, C.S.B.; writing—review and editing, R.V.S., C.I.-D., A.S.M., I.S.,

G.B.; visualization, C.S.B.; supervision, R.V.S. and C.I-D.; project administration, C.S.B.; funding acquisition, C.I.-D., I.S. and C.S.B. All authors have read and agreed to the published version of the manuscript.

Funding: The work was funded by the German Research Foundation, SFB1340-1 "Matrix in Vision" project B05, the nonprofit Hertie foundation (P1190047 to C.S.B and C.I.D) and the Research Training Group GRK2260 BIOQIC.

Institutional Review Board Statement: This study was approved by the Berlin State Office for Health and Social Affairs (LAGeSo, G106/19) and conducted in strict adherence to the European guidelines for the care and use of laboratory animals under directive 2010/63/EU of the European Parliament and of the Council of 22 September 2010.

Informed Consent Statement: Not applicable.

Data Availability Statement: The raw data supporting the conclusions of this article are available upon request from the corresponding author.

Acknowledgments: The authors thank Philipp Boehm-Sturm and Susanne Mueller from the Department of Experimental Neurology, Center for Stroke Research and the NeuroCure Cluster of Excellence, Charité Core Facility 7T Experimental MRIs at the Charité - Universitätsmedizin Berlin, Germany, for the support with the MRE experiments.

Conflicts of Interest: The authors declare no conflict of interest. The funders had no role in the design of the study; in the collection, analyses, or interpretation of data; in the writing of the manuscript, or in the decision to publish the results.

References

1. *The Multiple Sclerosis International Federation, Atlas of MS*, 3rd ed.; Multiple Sclerosis International Federation: London, UK; 2020.
2. Gilli, F.; DiSano, K.D.; Pachner, A.R. SeXX Matters in Multiple Sclerosis. *Front. Neurol.* **2020**, *11*, 616. https://doi.org/10.3389/fneur.2020.00616.
3. Bergamaschi, R. Prognostic Factors in Multiple Sclerosis. *Int. Rev. Neurobiol.* **2007**, *79*, 423–447. https://doi.org/10.1016/S0074-7742(07)79019-0.
4. Voskuhl, R.R.; Patel, K.; Paul, F.; Gold, S.M.; Scheel, M.; Kuchling, J.; Cooper, G.; Asseyer, S.; Chien, C.; Brandt, A.U.; et al. Sex Differences in Brain Atrophy in Multiple Sclerosis. *Biol. Sex Differ.* **2020**, *11*, 49. https://doi.org/10.1186/s13293-020-00326-3.
5. Bove, R.; Chitnis, T. The Role of Gender and Sex Hormones in Determining the Onset and Outcome of Multiple Sclerosis. *Mult. Scler. J.* **2014**, *20*, 520–526. https://doi.org/10.1177/1352458513519181.
6. Dunn, S.E.; Gunde, E.; Lee, H. Sex-Based Differences in Multiple Sclerosis (MS): Part II: Rising Incidence of Multiple Sclerosis in Women and the Vulnerability of Men to Progression of This Disease. *Curr. Top. Behav. Neurosci.* **2015**, *26*, 57–86. https://doi.org/10.1007/7854_2015_370.
7. Dunn, S.E.; Lee, H.; Pavri, F.R.; Zhang, M.A. Sex-Based Differences in Multiple Sclerosis (Part I): Biology of Disease Incidence. *Curr. Top. Behav. Neurosci.* **2015**, *26*, 29–56. https://doi.org/10.1007/7854_2015_371.
8. Magyari, M. Gender Differences in Multiple Sclerosis Epidemiology and Treatment Response. *Dan. Med. J.* **2016**, *63*, B5212.
9. Golden, L.C.; Voskuhl, R. The Importance of Studying Sex Differences in Disease: The Example of Multiple Sclerosis. *J. Neurosci. Res.* **2017**, *95*, 633–643. https://doi.org/10.1002/jnr.23955.
10. Koch-Henriksen, N.; Sørensen, P.S. The Changing Demographic Pattern of Multiple Sclerosis Epidemiology. *Lancet Neurol.* **2010**, *9*, 520–532. https://doi.org/10.1016/S1474-4422(10)70064-8.
11. Hiscox, L.V.; Johnson, C.L.; Barnhill, E.; McGarry, M.D.J.; Huston, J.; van Beek, E.J.R.; Starr, J.M.; Roberts, N. Magnetic Resonance Elastography (MRE) of the Human Brain: Technique, Findings and Clinical Applications. *Phys. Med. Biol.* **2016**, *61*, R401–R437. https://doi.org/10.1088/0031-9155/61/24/R401.
12. Wuerfel, J.; Paul, F.; Beierbach, B.; Hamhaber, U.; Klatt, D.; Papazoglou, S.; Zipp, F.; Martus, P.; Braun, J.; Sack, I. MR-Elastography Reveals Degradation of Tissue Integrity in Multiple Sclerosis. *NeuroImage* **2010**, *49*, 2520–2525. https://doi.org/10.1016/j.neuroimage.2009.06.018.
13. Sack, I.; Beierbach, B.; Wuerfel, J.; Klatt, D.; Hamhaber, U.; Papazoglou, S.; Martus, P.; Braun, J. The Impact of Aging and Gender on Brain Viscoelasticity. *NeuroImage* **2009**, *46*, 652–657. https://doi.org/10.1016/j.neuroimage.2009.02.040.
14. Arani, A.; Murphy, M.C.; Glaser, K.J.; Manduca, A.; Lake, D.S.; Kruse, S.A.; Jack, C.R.; Ehman, R.L.; Huston, J. Measuring the Effects of Aging and Sex on Regional Brain Stiffness with MR Elastography in Healthy Older Adults. *NeuroImage* **2015**, *111*, 59–64. https://doi.org/10.1016/j.neuroimage.2015.02.016.
15. Streitberger, K.-J.; Sack, I.; Krefting, D.; Pfüller, C.; Braun, J.; Paul, F.; Wuerfel, J. Brain Viscoelasticity Alteration in Chronic-Progressive Multiple Sclerosis. *PLoS ONE* **2012**, *7*, e29888. https://doi.org/10.1371/journal.pone.0029888.

16. Fehlner, A.; Behrens, J.R.; Streitberger, K.-J.; Papazoglou, S.; Braun, J.; Bellmann-Strobl, J.; Ruprecht, K.; Paul, F.; Würfel, J.; Sack, I. Higher-Resolution MR Elastography Reveals Early Mechanical Signatures of Neuroinflammation in Patients with Clinically Isolated Syndrome. *J. Magn. Reson. Imaging JMRI* **2016**, *44*, 51–58. https://doi.org/10.1002/jmri.25129.
17. Riek, K.; Millward, J.M.; Hamann, I.; Mueller, S.; Pfueller, C.F.; Paul, F.; Braun, J.; Infante-Duarte, C.; Sack, I. Magnetic Resonance Elastography Reveals Altered Brain Viscoelasticity in Experimental Autoimmune Encephalomyelitis. *NeuroImage Clin.* **2012**, *1*, 81–90. https://doi.org/10.1016/j.nicl.2012.09.003.
18. Wang, S.; Millward, J.M.; Hanke-Vela, L.; Malla, B.; Pilch, K.; Gil-Infante, A.; Waiczies, S.; Mueller, S.; Boehm-Sturm, P.; Guo, J.; et al. MR Elastography-Based Assessment of Matrix Remodeling at Lesion Sites Associated With Clinical Severity in a Model of Multiple Sclerosis. *Front. Neurol.* **2019**, *10*, 1382. https://doi.org/10.3389/fneur.2019.01382.
19. Silva, R.V.; Morr, A.S.; Mueller, S.; Koch, S.P.; Boehm-Sturm, P.; Rodriguez-Sillke, Y.; Kunkel, D.; Tzschätzsch, H.; Kühl, A.A.; Schnorr, J.; et al. Contribution of Tissue Inflammation and Blood-Brain Barrier Disruption to Brain Softening in a Mouse Model of Multiple Sclerosis. *Front. Neurosci.* **2021**, *15*, 701308. https://doi.org/10.3389/fnins.2021.701308.
20. Schregel, K.; Wuerfel nee Tysiak, E.; Garteiser, P.; Gemeinhardt, I.; Prozorovski, T.; Aktas, O.; Merz, H.; Petersen, D.; Wuerfel, J.; Sinkus, R. Demyelination Reduces Brain Parenchymal Stiffness Quantified in Vivo by Magnetic Resonance Elastography. *Proc. Natl. Acad. Sci. USA* **2012**, *109*, 6650–6655. https://doi.org/10.1073/pnas.1200151109.
21. Weickenmeier, J.; de Rooij, R.; Budday, S.; Steinmann, P.; Ovaert, T.C.; Kuhl, E. Brain Stiffness Increases with Myelin Content. *Acta Biomater.* **2016**, *42*, 265–272. https://doi.org/10.1016/j.actbio.2016.07.040.
22. Guo, J.; Bertalan, G.; Meierhofer, D.; Klein, C.; Schreyer, S.; Steiner, B.; Wang, S.; Vieira da Silva, R.; Infante-Duarte, C.; Koch, S.; et al. Brain Maturation Is Associated with Increasing Tissue Stiffness and Decreasing Tissue Fluidity. *Acta Biomater.* **2019**, *99*, 433–442. https://doi.org/10.1016/j.actbio.2019.08.036.
23. Ghorbani, S.; Yong, V.W. The Extracellular Matrix as Modifier of Neuroinflammation and Remyelination in Multiple Sclerosis. *Brain* **2021**, *144*, 1958–1973. https://doi.org/10.1093/brain/awab059.
24. Van Horssen, J.; Dijkstra, C.D.; De Vries, H.E. The Extracellular Matrix in Multiple Sclerosis Pathology. *J. Neurochem.* **2007**, *103*, 1293–1301. https://doi.org/10.1111/j.1471-4159.2007.04897.x.
25. Voskuhl, R.R.; Gold, S.M. Sex-Related Factors in Multiple Sclerosis Susceptibility and Progression. *Nat. Rev. Neurol.* **2012**, *8*, 255–263. https://doi.org/10.1038/nrneurol.2012.43.
26. Gold, S.M.; Sasidhar, M.V.; Morales, L.B.; Du, S.; Sicotte, N.L.; Tiwari-Woodruff, S.K.; Voskuhl, R.R. Estrogen Treatment Decreases Matrix Metalloproteinase (MMP)-9 in Autoimmune Demyelinating Disease through Estrogen Receptor Alpha (ERalpha). *Lab. Investig. J. Tech. Methods Pathol.* **2009**, *89*, 1076–1083. https://doi.org/10.1038/labinvest.2009.79.
27. Lau, L.W.; Cua, R.; Keough, M.B.; Haylock-Jacobs, S.; Yong, V.W. Pathophysiology of the Brain Extracellular Matrix: A New Target for Remyelination. *Nat. Rev. Neurosci.* **2013**, *14*, 722–729. https://doi.org/10.1038/nrn3550.
28. Miller, R.T. Mechanical Properties of Basement Membrane in Health and Disease. *Matrix Biol. J. Int. Soc. Matrix Biol.* **2017**, *57–58*, 366–373. https://doi.org/10.1016/j.matbio.2016.07.001.
29. Bertalan, G.; Guo, J.; Tzschätzsch, H.; Klein, C.; Barnhill, E.; Sack, I.; Braun, J. Fast Tomoelastography of the Mouse Brain by Multifrequency Single-Shot MR Elastography. *Magn. Reson. Med.* **2019**, *81*, 2676–2687. https://doi.org/10.1002/mrm.27586.
30. Teuscher, C.; Bunn, J.Y.; Fillmore, P.D.; Butterfield, R.J.; Zachary, J.F.; Blankenhorn, E.P. Gender, Age, and Season at Immunization Uniquely Influence the Genetic Control of Susceptibility to Histopathological Lesions and Clinical Signs of Experimental Allergic Encephalomyelitis. *Am. J. Pathol.* **2004**, *165*, 1593–1602. https://doi.org/10.1016/S0002-9440(10)63416-5.
31. Papenfuss, T.L.; Rogers, C.J.; Gienapp, I.; Yurrita, M.; McClain, M.; Damico, N.; Valo, J.; Song, F.; Whitacre, C.C. Sex Differences in Experimental Autoimmune Encephalomyelitis in Multiple Murine Strains. *J. Neuroimmunol.* **2004**, *150*, 59–69. https://doi.org/10.1016/j.jneuroim.2004.01.018.
32. Millward, J.M.; Guo, J.; Berndt, D.; Braun, J.; Sack, I.; Infante-Duarte, C. Tissue Structure and Inflammatory Processes Shape Viscoelastic Properties of the Mouse Brain. *NMR Biomed.* **2015**, *28*, 831–839. https://doi.org/10.1002/nbm.3319.
33. Millward, J.M.; Ariza de Schellenberger, A.; Berndt, D.; Hanke-Vela, L.; Schellenberger, E.; Waiczies, S.; Taupitz, M.; Kobayashi, Y.; Wagner, S.; Infante-Duarte, C. Application of Europium-Doped Very Small Iron Oxide Nanoparticles to Visualize Neuroinflammation with MRI and Fluorescence Microscopy. *Neuroscience* **2019**, *403*, 136–144. https://doi.org/10.1016/j.neuroscience.2017.12.014.
34. Zamani, A.; Powell, K.L.; May, A.; Semple, B.D. Validation of Reference Genes for Gene Expression Analysis Following Experimental Traumatic Brain Injury in a Pediatric Mouse Model. *Brain Res. Bull.* **2020**, *156*, 43–49. https://doi.org/10.1016/j.brainresbull.2019.12.015.
35. Kang, Y.; Wu, Z.; Cai, D.; Lu, B. Evaluation of Reference Genes for Gene Expression Studies in Mouse and N2a Cell Ischemic Stroke Models Using Quantitative Real-Time PCR. *BMC Neurosci.* **2018**, *19*, 3. https://doi.org/10.1186/s12868-018-0403-6.
36. Bennasroune, A.; Romier-Crouzet, B.; Blaise, S.; Laffargue, M.; Efremov, R.G.; Martiny, L.; Maurice, P.; Duca, L. Elastic Fibers and Elastin Receptor Complex: Neuraminidase-1 Takes the Center Stage. *Matrix Biol. J. Int. Soc. Matrix Biol.* **2019**, *84*, 57–67. https://doi.org/10.1016/j.matbio.2019.06.007.
37. Culav, E.M.; Clark, C.H.; Merrilees, M.J. Connective Tissues: Matrix Composition and Its Relevance to Physical Therapy. *Phys. Ther.* **1999**, *79*, 308–319.
38. Guarnieri, D.; Battista, S.; Borzacchiello, A.; Mayol, L.; De Rosa, E.; Keene, D.R.; Muscariello, L.; Barbarisi, A.; Netti, P.A. Effects of Fibronectin and Laminin on Structural, Mechanical and Transport Properties of 3D Collageneous Network. *J. Mater. Sci. Mater. Med.* **2007**, *18*, 245–253. https://doi.org/10.1007/s10856-006-0686-5.

39. Storm, C.; Pastore, J.J.; MacKintosh, F.C.; Lubensky, T.C.; Janmey, P.A. Nonlinear Elasticity in Biological Gels. *Nature* **2005**, *435*, 191–194. https://doi.org/10.1038/nature03521.
40. Li, H.; Zheng, Y.; Han, Y.L.; Cai, S.; Guo, M. Nonlinear Elasticity of Biological Basement Membrane Revealed by Rapid Inflation and Deflation. *Proc. Natl. Acad. Sci. USA* **2021**, *118*, e2022422118. https://doi.org/10.1073/pnas.2022422118.
41. Bhave, G.; Colon, S.; Ferrell, N. The Sulfilimine Cross-Link of Collagen IV Contributes to Kidney Tubular Basement Membrane Stiffness. *Am. J. Physiol. Ren. Physiol.* **2017**, *313*, F596–F602. https://doi.org/10.1152/ajprenal.00096.2017.
42. Pastor-Pareja, J.C.; Xu, T. Shaping Cells and Organs in Drosophila by Opposing Roles of Fat Body-Secreted Collagen IV and Perlecan. *Dev. Cell* **2011**, *21*, 245–256. https://doi.org/10.1016/j.devcel.2011.06.026.
43. Candiello, J.; Balasubramani, M.; Schreiber, E.M.; Cole, G.J.; Mayer, U.; Halfter, W.; Lin, H. Biomechanical Properties of Native Basement Membranes. *FEBS J.* **2007**, *274*, 2897–2908. https://doi.org/10.1111/j.1742-4658.2007.05823.x.
44. Gould, D.B.; Phalan, F.C.; Breedveld, G.J.; van Mil, S.E.; Smith, R.S.; Schimenti, J.C.; Aguglia, U.; van der Knaap, M.S.; Heutink, P.; John, S.W.M. Mutations in Col4a1 Cause Perinatal Cerebral Hemorrhage and Porencephaly. *Science* **2005**, *308*, 1167–1171. https://doi.org/10.1126/science.1109418.
45. Gould, D.B.; Phalan, F.C.; van Mil, S.E.; Sundberg, J.P.; Vahedi, K.; Massin, P.; Bousser, M.G.; Heutink, P.; Miner, J.H.; Tournier-Lasserve, E.; et al. Role of COL4A1 in Small-Vessel Disease and Hemorrhagic Stroke. *N. Engl. J. Med.* **2006**, *354*, 1489–1496. https://doi.org/10.1056/NEJMoa053727.
46. Pöschl, E.; Schlötzer-Schrehardt, U.; Brachvogel, B.; Saito, K.; Ninomiya, Y.; Mayer, U. Collagen IV Is Essential for Basement Membrane Stability but Dispensable for Initiation of Its Assembly during Early Development. *Dev. Camb. Engl.* **2004**, *131*, 1619–1628. https://doi.org/10.1242/dev.01037.
47. Leclech, C.; Natale, C.F.; Barakat, A.I. The Basement Membrane as a Structured Surface—Role in Vascular Health and Disease. *J. Cell Sci.* **2020**, *133*, jcs239889. https://doi.org/10.1242/jcs.239889.
48. Yurchenco, P.D. Basement Membranes: Cell Scaffoldings and Signaling Platforms. *Cold Spring Harb. Perspect. Biol.* **2011**, *3*, a004911. https://doi.org/10.1101/cshperspect.a004911.
49. Morrissey, M.A.; Sherwood, D.R. An Active Role for Basement Membrane Assembly and Modification in Tissue Sculpting. *J. Cell Sci.* **2015**, *128*, 1661–1668. https://doi.org/10.1242/jcs.168021.
50. Sarver, D.C.; Kharaz, Y.A.; Sugg, K.B.; Gumucio, J.P.; Comerford, E.; Mendias, C.L. Sex Differences in Tendon Structure and Function. *J. Orthop. Res. Off. Publ. Orthop. Res. Soc.* **2017**, *35*, 2117–2126. https://doi.org/10.1002/jor.23516.
51. Kim, J.M.; Shin, S.-C.; Park, G.-C.; Lee, J.-C.; Jeon, Y.K.; Ahn, S.J.; Thibeault, S.; Lee, B.-J. Effect of Sex Hormones on Extracellular Matrix of Lamina Propria in Rat Vocal Fold. *Laryngoscope* **2020**, *130*, 732–740. https://doi.org/10.1002/lary.28086.
52. Soldano, S.; Montagna, P.; Villaggio, B.; Parodi, A.; Gianotti, G.; Sulli, A.; Seriolo, B.; Secchi, M.E.; Cutolo, M. Endothelin and Sex Hormones Modulate the Fibronectin Synthesis by Cultured Human Skin Scleroderma Fibroblasts. *Ann. Rheum. Dis.* **2009**, *68*, 599–602. https://doi.org/10.1136/ard.2008.097378.
53. Kehlet, S.N.; Willumsen, N.; Armbrecht, G.; Dietzel, R.; Brix, S.; Henriksen, K.; Karsdal, M.A. Age-Related Collagen Turnover of the Interstitial Matrix and Basement Membrane: Implications of Age- and Sex-Dependent Remodeling of the Extracellular Matrix. *PLoS ONE* **2018**, *13*, e0194458. https://doi.org/10.1371/journal.pone.0194458.
54. Hall, G.; Phillips, T.J. Estrogen and Skin: The Effects of Estrogen, Menopause, and Hormone Replacement Therapy on the Skin. *J. Am. Acad. Dermatol.* **2005**, *53*, 555–568. https://doi.org/10.1016/j.jaad.2004.08.039.
55. Freimann, F.B.; Müller, S.; Streitberger, K.-J.; Guo, J.; Rot, S.; Ghori, A.; Vajkoczy, P.; Reiter, R.; Sack, I.; Braun, J. MR Elastography in a Murine Stroke Model Reveals Correlation of Macroscopic Viscoelastic Properties of the Brain with Neuronal Density. *NMR Biomed.* **2013**, *26*, 1534–1539. https://doi.org/10.1002/nbm.2987.
56. Pakkenberg, B.; Gundersen, H.J. Neocortical Neuron Number in Humans: Effect of Sex and Age. *J. Comp. Neurol.* **1997**, *384*, 312–320.
57. Rabinowicz, T.; Petetot, J.M.-C.; Gartside, P.S.; Sheyn, D.; Sheyn, T.; de Courten-Myers, G.M. Structure of the Cerebral Cortex in Men and Women. *J. Neuropathol. Exp. Neurol.* **2002**, *61*, 46–57. https://doi.org/10.1093/jnen/61.1.46.
58. Mouton, P.R.; Long, J.M.; Lei, D.-L.; Howard, V.; Jucker, M.; Calhoun, M.E.; Ingram, D.K. Age and Gender Effects on Microglia and Astrocyte Numbers in Brains of Mice. *Brain Res.* **2002**, *956*, 30–35. https://doi.org/10.1016/S0006-8993(02)03475-3.
59. Cahill, L. Why Sex Matters for Neuroscience. *Nat. Rev. Neurosci.* **2006**, *7*, 477–484. https://doi.org/10.1038/nrn1909.
60. Chou, X.-L.; Fang, Q.; Yan, L.; Zhong, W.; Peng, B.; Li, H.; Wei, J.; Tao, H.W.; Zhang, L.I. Contextual and Cross-Modality Modulation of Auditory Cortical Processing through Pulvinar Mediated Suppression. *eLife* **2020**, *9*, e54157. https://doi.org/10.7554/eLife.54157.
61. Fang, Q.; Chou, X.-L.; Peng, B.; Zhong, W.; Zhang, L.I.; Tao, H.W. A Differential Circuit via Retino-Colliculo-Pulvinar Pathway Enhances Feature Selectivity in Visual Cortex through Surround Suppression. *Neuron* **2020**, *105*, 355–369.e6. https://doi.org/10.1016/j.neuron.2019.10.027.
62. Huang, A.S.; Rogers, B.P.; Sheffield, J.M.; Vandekar, S.; Anticevic, A.; Woodward, N.D. Characterizing Effects of Age, Sex and Psychosis Symptoms on Thalamocortical Functional Connectivity in Youth. *NeuroImage* **2021**, *243*, 118562. https://doi.org/10.1016/j.neuroimage.2021.118562.
63. Kipp, M.; Nyamoya, S.; Hochstrasser, T.; Amor, S. Multiple Sclerosis Animal Models: A Clinical and Histopathological Perspective. *Brain Pathol.* **2017**, *27*, 123–137. https://doi.org/10.1111/bpa.12454.
64. Scheld, M.; Rüther, B.J.; Große-Veldmann, R.; Ohl, K.; Tenbrock, K.; Dreymüller, D.; Fallier-Becker, P.; Zendedel, A.; Beyer, C.; Clarner, T.; et al. Neurodegeneration Triggers Peripheral Immune Cell Recruitment into the Forebrain. *J. Neurosci.* **2016**, *36*, 1410. https://doi.org/10.1523/JNEUROSCI.2456-15.2016.

65. Guo, J.; Hirsch, S.; Fehlner, A.; Papazoglou, S.; Scheel, M.; Braun, J.; Sack, I. Towards an Elastographic Atlas of Brain Anatomy. *PLoS ONE* **2013**, *8*, e71807. https://doi.org/10.1371/journal.pone.0071807.
66. Braun, J.; Guo, J.; Lützkendorf, R.; Stadler, J.; Papazoglou, S.; Hirsch, S.; Sack, I.; Bernarding, J. High-Resolution Mechanical Imaging of the Human Brain by Three-Dimensional Multifrequency Magnetic Resonance Elastography at 7T. *NeuroImage* **2014**, *90*, 308–314. https://doi.org/10.1016/j.neuroimage.2013.12.032.
67. Streitberger, K.-J.; Fehlner, A.; Pache, F.; Lacheta, A.; Papazoglou, S.; Bellmann-Strobl, J.; Ruprecht, K.; Brandt, A.; Braun, J.; Sack, I.; et al. Multifrequency Magnetic Resonance Elastography of the Brain Reveals Tissue Degeneration in Neuromyelitis Optica Spectrum Disorder. *Eur. Radiol.* **2017**, *27*, 2206–2215. https://doi.org/10.1007/s00330-016-4561-6.
68. Moeendarbary, E.; Weber, I.P.; Sheridan, G.K.; Koser, D.E.; Soleman, S.; Haenzi, B.; Bradbury, E.J.; Fawcett, J.; Franze, K. The Soft Mechanical Signature of Glial Scars in the Central Nervous System. *Nat. Commun.* **2017**, *8*, 14787. https://doi.org/10.1038/ncomms14787.
69. Embry, A.E.; Liu, Z.; Henderson, J.M.; Byfield, F.J.; Liu, L.; Yoon, J.; Wu, Z.; Cruz, K.; Moradi, S.; Gillombardo, C.B.; et al. Similar Biophysical Abnormalities in Glomeruli and Podocytes from Two Distinct Models. *J. Am. Soc. Nephrol. JASN* **2018**, *29*, 1501–1512. https://doi.org/10.1681/ASN.2017050475.
70. Rempe, R.G.; Hartz, A.M.; Bauer, B. Matrix Metalloproteinases in the Brain and Blood-Brain Barrier: Versatile Breakers and Makers. *J. Cereb. Blood Flow Metab.* **2016**, *36*, 1481–1507. https://doi.org/10.1177/0271678X16655551.
71. Sobel, R.A. The Extracellular Matrix in Multiple Sclerosis: An Update. *Braz. J. Med. Biol. Res.* **2001**, *34*, 603–609. https://doi.org/10.1590/S0100-879X2001000500007.
72. Zeis, T.; Kinter, J.; Herrero-Herranz, E.; Weissert, R.; Schaeren-Wiemers, N. Gene Expression Analysis of Normal Appearing Brain Tissue in an Animal Model for Multiple Sclerosis Revealed Grey Matter Alterations, but Only Minor White Matter Changes. *J. Neuroimmunol.* **2008**, *205*, 10–19. https://doi.org/10.1016/j.jneuroim.2008.09.009.
73. Lassmann, H. Pathogenic Mechanisms Associated With Different Clinical Courses of Multiple Sclerosis. *Front. Immunol.* **2019**, *9*, 3116. https://doi.org/10.3389/fimmu.2018.03116.
74. Ulbrich, P.; Khoshneviszadeh, M.; Jandke, S.; Schreiber, S.; Dityatev, A. Interplay between Perivascular and Perineuronal Extracellular Matrix Remodelling in Neurological and Psychiatric Diseases. *Eur. J. Neurosci.* **2021**, *53*, 3811–3830. https://doi.org/10.1111/ejn.14887.
75. Jang, D.G.; Sim, H.J.; Song, E.K.; Kwon, T.; Park, T.J. Extracellular Matrixes and Neuroinflammation. *BMB Rep.* **2020**, *53*, 491–499. https://doi.org/10.5483/BMBRep.2020.53.10.156.
76. Streitberger, K.-J.; Lilaj, L.; Schrank, F.; Braun, J.; Hoffmann, K.-T.; Reiss-Zimmermann, M.; Käs, J.A.; Sack, I. How Tissue Fluidity Influences Brain Tumor Progression. *Proc. Natl. Acad. Sci. USA* **2020**, *117*, 128–134. https://doi.org/10.1073/pnas.1913511116.
77. Chaudhuri, O.; Cooper-White, J.; Janmey, P.A.; Mooney, D.J.; Shenoy, V.B. The Impact of Extracellular Matrix Viscoelasticity on Cellular Behavior. *Nature* **2020**, *584*, 535–546. https://doi.org/10.1038/s41586-020-2612-2.
78. Elosegui-Artola, A. The Extracellular Matrix Viscoelasticity as a Regulator of Cell and Tissue Dynamics. *Curr. Opin. Cell Biol.* **2021**, *72*, 10–18. https://doi.org/10.1016/j.ceb.2021.04.002.
79. van Wageningen, T.A.; Antonovaite, N.; Paardekam, E.; Brevé, J.J.P.; Iannuzzi, D.; van Dam, A.-M. Viscoelastic Properties of White and Gray Matter-Derived Microglia Differentiate upon Treatment with Lipopolysaccharide but Not upon Treatment with Myelin. *J. Neuroinflammation* **2021**, *18*, 83. https://doi.org/10.1186/s12974-021-02134-x.
80. Previtera, M.L.; Langhammer, C.G.; Firestein, B.L. Effects of Substrate Stiffness and Cell Density on Primary Hippocampal Cultures. *J. Biosci. Bioeng.* **2010**, *110*, 459–470. https://doi.org/10.1016/j.jbiosc.2010.04.004.
81. Georges, P.C.; Miller, W.J.; Meaney, D.F.; Sawyer, E.S.; Janmey, P.A. Matrices with Compliance Comparable to That of Brain Tissue Select Neuronal over Glial Growth in Mixed Cortical Cultures. *Biophys. J.* **2006**, *90*, 3012–3018. https://doi.org/10.1529/biophysj.105.073114.
82. Urbanski, M.M.; Kingsbury, L.; Moussouros, D.; Kassim, I.; Mehjabeen, S.; Paknejad, N.; Melendez-Vasquez, C.V. Myelinating Glia Differentiation Is Regulated by Extracellular Matrix Elasticity. *Sci. Rep.* **2016**, *6*, 33751. https://doi.org/10.1038/srep33751.

Curriculum Vitae

My curriculum vitae does not appear in the electronic version of my thesis for reasons of data protection.

My curriculum vitae does not appear in the electronic version of my thesis for reasons of data protection.

My curriculum vitae does not appear in the electronic version of my thesis for reasons of data protection.

Publication list

Original research articles

Bertalan, G., Becker, J., Tzschätzsch, H., **Morr, A.**, Herthum, H., Shahryari, M., Greenhalgh, R.D., Guo, J., Schröder, L., Alzheimer, C., Budday, S., Franze, K., Braun, J., Sack, I. Mechanical behavior of the hippocampus and corpus callosum: An attempt to reconcile ex vivo with in vivo and micro with macro properties. Journal of the Mechanical Behavior of Biomedical Materials. 2022, 105613.
Impact factor: 3.902 (Journal Citation Report 2020)

Morr, A.S., Nowicki, M., Bertalan, G., Vieira Silva, R., Infante Duarte, C., Koch, S.P., Boehm-Sturm, P., Krügel, U., Braun, J., Steiner, B., Käs, J.A., Fuhs, T., Sack, I. Mechanical properties of murine hippocampal subregions investigated by atomic force microscopy and in vivo magnetic resonance elastography. Scientific Reports 2022, 12(1), 1-11. https://doi.org/10.1038/s41598-022-21105-7
Impact factor: 4.379 (Journal Citation Report 2020)

Anderhalten L, Silva RV, **Morr A**, Wang S, Smorodchenko A, Saatz J, Traub H, Mueller S, Boehm-Sturm P, Rodriguez-Sillke Y, Kunkel D, Hahndorf J, Paul F, Taupitz M, Sack I, Infante-Duarte C. Different Impact of Gadopentetate and Gadobutrol on Inflammation-Promoted Retention and Toxicity of Gadolinium Within the Mouse Brain. Invest Radiol. 2022 Investigative Radiology: October 2022 - Volume 57 - Issue 10 - p 677-688 doi: 10.1097/RLI.0000000000000884
Impact factor: 6.016 (Journal Citation Report 2020)

Morr AS, Herthum H, Schrank F, Görner S, Anders MS, Lerchbaumer M, Müller HP, Fischer T, Jenderka KV, Hansen HHG, Janmey PA, Braun J, Sack I, Tzschätzsch H. Liquid-Liver Phantom: Mimicking the Viscoelastic Dispersion of Human Liver for Ultrasound- and MRI-Based Elastography. Invest Radiol. 2022 Aug 1;57(8):502-509. doi: 10.1097/RLI.0000000000000862. Epub 2022 Feb 23. PMID: 35195086.
Impact factor: 6.016 (Journal Citation Report 2020)

Batzdorf CS, **Morr AS**, Bertalan G, Sack I, Silva RV, Infante-Duarte C. Sexual Dimorphism in Extracellular Matrix Composition and Viscoelasticity of the Healthy and Inflamed Mouse Brain. Biology (Basel). 2022 Jan 31;11(2):230. doi: 10.3390/biology11020230. PMID: 35205095; PMCID: PMC8869215.
Impact factor: 5.079 (Journal Citation Report 2020)

Silva RV*, **Morr AS***, Mueller S, Koch SP, Boehm-Sturm P, Rodriguez-Sillke Y, Kunkel D, Tzschätzsch H, Kühl AA, Schnorr J, Taupitz M, Sack I, Infante-Duarte C. Contribution of Tissue Inflammation and Blood-Brain Barrier Disruption to Brain Softening in a Mouse Model of Multiple Sclerosis. Front Neurosci. 2021 Aug 23;15:701308. doi: 10.3389/fnins.2021.701308. PMID: 34497486; PMCID: PMC8419310.
*Rafaela Vieira da Silva and Anna Sophie Morr contributed equally to this work and share the first authorship.
Impact factor: 3.707 (Journal Citation Report 2019)

Garczyńska K, Tzschätzsch H, Kühl AA, **Morr AS**, Lilaj L, Häckel A, Schellenberger E, Berndt N, Holzhütter HG, Braun J, Sack I, Guo J. Changes in Liver Mechanical Properties and Water Diffusivity During Normal Pregnancy Are Driven by Cellular Hypertrophy. Front Physiol. 2020 Nov 23;11:605205. doi: 10.3389/fphys.2020.605205. PMID: 33329058; PMCID: PMC7719759.
Impact factor: 3.201 (Journal Citation Report 2018)

Johansson EM, Bouchet D, Tamouza R, Ellul P, **Morr AS**, Avignone E, Germi R, Leboyer M, Perron H, Groc L. Human endogenous retroviral protein triggers deficit in glutamate synapse maturation and behaviors associated with psychosis. Sci Adv. 2020 Jul 17;6(29):eabc0708. doi: 10.1126/sciadv.abc0708. PMID: 32832650; PMCID: PMC7439645.
Impact factor: 12.804 (Journal Citation Report 2018)

Bertalan G, Boehm-Sturm P, Schreyer S, **Morr AS**, Steiner B, Tzschätzsch H, Braun J, Guo J, Sack I. The influence of body temperature on tissue stiffness, blood perfusion, and water diffusion in the mouse brain. Acta Biomater. 2019 Sep 15;96:412-420. doi: 10.1016/j.actbio.2019.06.034. Epub 2019 Jun 25. PMID: 31247381.
Impact factor: 6.383 (Journal Citation Report 2017)

Conference Contributions

Presentations

Anna Morr, Rafaela Vieira da Silva, Gergely Bertalan, Stefan Paul Koch, Susanne Mueller, Philipp Boehm-Sturm, Jürgen Braun, Carmen Infante Duarte, and Ingolf Sack Brain stiffness changes before disease onset and reflects remission and relapse in a mouse model of multiple sclerosis, presentation in a Combined Educational-Scientific oral session, ISMRM & SMRT Annual Meeting & Exhibition, virtually from 15-20 May 2021

Anna Morr, Inflammation induced changes of the mechanical properties of the ECM, 1st International Symposium In vivo Visualization of Extracellular Matrix Pathology CRC 1340 Matrix in Vision Charité Berlin, virtually from 27-28 May 2021

Posters

Anna Morr, Helge Herthum, Felix Schrank, Steffen Görner, Jürgen Braun, Ingolf Sack, and Heiko Tzschätzsch
A viscoelastic phantom of the healthy human liver for elastography in MRI and ultrasound, digital poster, ISMRM & SMRT Annual Meeting & Exhibition, virtually from 15-20 May 2021

Anna Morr, Marcin Nowicki, Gergely Bertalan, Rafaela Vieira da Silva, Carmen Infante Duarte, Stefan Paul Koch, Philipp Boehm-Sturm, Ute Krügel, Jürgen Braun, Barbara Steiner, Josef Käs, ThomasFuhs, and Ingolf Sack
In vivo MR elastography of the murine hippocampus is sensitive to the microscopic mechanical properties of dentate gyrus subzones, digital poster, ISMRM & SMRT Annual Meeting & Exhibition, virtually from 15-20 May 2021

Acknowledgments

First of all, I would like to thank Prof. Ingolf Sack, head of the MRE research group at Charité, for the supervision of my doctoral studies in the last four years. Without his feedback, motivation and trust into my professional competences, this thesis but also my personal development would not have been possible. Also, I would like to thank Prof. Carmen Infante-Duarte, head of the experimental neuroimmunology research group of the Experimental and Clinical Research Center, who critically evaluated my work from a biological perspective.

Second, I would like to thank Rafaela Vieira da Silva for working together with me on the SFB projects. Without her the PhD journey, would have been harder, less fun and not as fruitful in terms of results. I also want to thank Karolina Krehl for always listening to my problems and encouraging me to not give up. I am genuinely thankful for the support of the entire MRE research group, especially Heiko Tzschätzsch, without their expertise this thesis would not have been possible: Bernhard Kreft, Carsten Warmuth, Gergely Bertalan, Helge Herthum, Jacob Jordan, Jing Guo, Joachim Snellings, Judith Bergs, Jürgen Braun, Ledia Lilaj, Mahsa Salimi Majd, Matthias Anders, Mehrgan Shahryari, Steffen Görner, Tom Meyer and Yasmine Safraou.

Last but not least, I would like to thank Nico, my whole family and friends. Without their support and comfort, I would have not successfully finished my PhD journey.